Universität
Zürich UZH

Development of Ultrafast Time-Resolved Chiral Infrared Spectroscopy

---

Dissertation
zur
Erlangung der naturwissenschaftlichen Doktorwürde
(Dr. sc. nat.)

von
Mathias Bonmarin
von
Val-de-Travers (NE)

CMSZH
CHEMICAL MOLECULAR SCIENCES ZURICH
GRADUATE SCHOOL

Development of Ultrafast Time-Resolved Chiral Infrared Spectroscopy

---

Dissertation
zur
Erlangung der naturwissenschaftlichen Doktorwürde
(Dr. sc. nat.)

vorgelegt der
Mathematisch-naturwissenschaftlichen Fakultät
der
Universität Zürich

von
Mathias Bonmarin
von
Val-de-Travers (NE)

Promotionskomitee
Prof. Dr. Peter Hamm (Vorsitz)
Dr. Jan Helbing
Prof. Dr. Jürg Hutter

Zürich, 2010

"Beati pauperes spiritu quoniam ipsorum est regnum caelorum." - Matthew 5,3.

To my parents.

List of publications

Parts of the results in this thesis have been published in the following articles:

- **M. Bonmarin** and J. Helbing, *A picosecond time-resolved vibrational circular dichroism spectrometer* Optics Letters **33**, 2086-2088 (2008).
- J. Helbing and **M. Bonmarin**, *Time-resolved chiral vibrational spectroscopy* Chimia **63**, 128-133 (2009).
- **M. Bonmarin** and J. Helbing, *Polarisation control of ultrashort mid-IR laser pulses for transient vibrational circular dichroism measurements* Chirality **21**, 298-306 (2009).
- J. Helbing and **M. Bonmarin** *Vibrational circular dichroism signal enhancement by self-heterodyning using elliptically polarised laser pulses* Journal of Chemical Physics **131**, 174507 (2009).

Contents

Abstract

Among the different techniques available to study the molecular structure, chiral spectroscopy is a fast, reliable method, where molecules can be investigated in the liquid phase. Chiral spectroscopy is based on optical activity. A molecule is said to be optically active if it interacts differently with left- and right-circular polarised light. The difference of absorption between the two circular states is referred to as circular dichroism (CD), whereas the difference of refraction is known as optical rotatory dispersion (ORD). Because the optical activity finds its origin in asymmetry, it is directly dependent of the molecular geometry. Probing optically active vibrational transitions allows to retrieve even more structural information as infrared spectra are usually more resolved than electronics ones. Extension of this technique to the recording of time-resolved chiral vibrational signals may enable the dynamics of conformation changes in biomolecules such as peptides and proteins to be followed with unprecedented details. Toward this goal, we report the first pulsed laser set-up capable of recording both static infrared CD and ORD spectra and photo-induced changes in vibrational circular dichroism (VCD) with picosecond time resolution. A femtosecond laser system is synchronized to a photo elastic modulator to produce alternating left- and right-circular polarised mid-IR pulses. Transient changes in vibrational circular dichroism of the CH-stretch vibrations of the cobalt-sparteine complex $Co(sp)Cl_2$ are presented in a first proof-of-principle experiment. Both static and transient vibrational chiral spectroscopy suffer two important drawbacks: Chiral signals are usually small and sensitive to polarisation-based artefacts, which mainly originate from the interaction between an imperfect probe beam polarisation and a non isotropic sample. We report on a new scheme for synchronizing the laser system and the photo elastic modulator which generates almost perfect probe polarisation states. The technique reduces possible polarisation-based artefacts and allows multichannel detection of the chiral signals normally obscured by polarisation sensitive optics of the monochromator. To increase signal size, a self-heterodyning configuration is implemented where a part of the probe pulse acts as a phase-locked local oscillator heterodyning the chiral signal. The technical improvements presented in this thesis should open the door to measurements of transient vibrational chiral spectra of biomolecules.

Zusammenfassung

Unter den verschiedenen Techniken zur Untersuchung molekularer Strukturen ist chirale Spektroskopie eine schnelle und verlässliche Methode, bei der Moleküle in flüssiger Phase studiert werden können. Chirale Spektroskopie basiert auf optischer Aktivität. Ein Molekül wird als optisch aktiv bezeichnet, wenn es mit rechts- und linkszirkular polarisiertem Licht unterschiedlich wechselwirkt. Der Absorptionsunterschied zwischen den beiden zirkularen Zuständen wird Circulardichroismus (CD) genannt, wohingegen der Brechungsunterschied als optische Rotationsdispersion (ORD) bekannt ist. Da die optische Aktivität von Asymmetrie herrührt, hängt sie direkt von der Molekülgeometrie ab. Das Abtasten optisch aktiver Vibrationsübergänge erlaubt es noch mehr strukturelle Information zu erhalten, da Infrarotspektren in der Regel besser aufgelöst sind als elektronische Spektren. Die Erweiterung dieser Technik auf das Messen zeitaufgelöster chiraler Vibrationssignale ermöglicht es, Konformationsdynamik in Biomolekülen wie Peptiden und Proteinen in beispiellosem Detail zu verfolgen. Mit Blick auf dieses Ziel berichten wir hier über den ersten gepulsten Laseraufbau, der es erlaubt sowohl statische Infrarot CD- und ORD-Spektren, als auch lichtinduzierte Änderungen im Infrarot-Circulardichroismus (VCD) mit Pikosekunden Zeitauflösung zu messen. Ein Femtosekundenlaser wird mit einem photoelastischen Modulator synchronisiert um abwechselnd links- und rechtszirkular polarisierte Pulse im mittleren Infrarot zu erzeugen. Transiente Änderungen im VCD der CH-Streckschwingung des Kobaltsparteinkomplexes Co(sp)Cl_2 werden als erste Machbarkeitsstudie präsentiert. Sowohl statische als auch transiente chirale Infrarotspektroskopie haben zwei wichtige Nachteile: Chirale Signale sind klein und empfindlich auf polarisationsbasierte Artefakte, die hauptsächlich von der Wechselwirkung eines nicht perfekt polarisierten Abtaststrahls mit doppelbrechender Optik herrühren. Wir stellen ein neues Schema zur Synchronisation des Lasersystems mit dem photoelastischen Modulator vor, das fast perfekt polarisierte Abtastzustände erzeugt. Diese Technik reduziert mögliche polarisationsbasierte Artefakte und erlaubt die Vielkanaldetektion der chiralen Signale, die sonst von der polarisationssensitiven Optik des Monochromators verdeckt werden. Um die Signalgröße zu erhöhen, wurde ein Selbstheterodynaufbau realisiert, wo ein Teil des Abtastpulses als phasenstarrer lokaler Oszillator dient, der das chirale Signal überlagert.

Die technischen Verbesserungen, die in dieser Arbeit präsentiert werden, können die Tür zur Messung von transienten chiralen Vibrationssignalen an Biomolekülen öffnen.

Résumé

Parmi les différentes techniques permettant l'étude de la structure des biomolécules en solution, la spectroscopie chirale présente l'avantage d'être rapide et fiable. Cette technique est basée sur le principe de l'activité optique: une molécule est dite optiquement active si elle interagit différemment avec la lumière polarisée circulairement droite et gauche. La différence d'absorption entre les deux états de polarisation est appelée dichroïsme circulaire (CD). La différence de réfraction est connue sous le nom de rotation optique (ORD). Trouvant son origine dans l'asymétrie, l'activité optique est donc directement liée à la géométrie des molécules.

L'étude des transitions vibrationnelles optiquement actives permet d'accéder à une information plus riche sur la structure des molécules. En effet, les spectres enregistrés dans l'infrarouge sont généralement plus structurés que ceux dans le visible et l'ultraviolet. La possibilité d'enregistrer des spectres vibrationnels chiraux transitoirs est très prometteuse. Cette technique devrait permettre le suivit des changements de conformation des biomolécules, comme par exemple les peptides et les protéines avec une précision inégalée à ce jour. Dans ce but, nous présentons dans cette thèse, le premier spectromètre utilisant un laser pulsé, capable d'enregistrer d'une part les spectres statiques infrarouges CD et ORD, d'autre part les changements photo induits dans le dichroïsme circulaire vibrationnel (VCD). Un laser femtoseconde est synchronisé avec un modulateur photo élastique afin de produire des impulsions infrarouges successivement polarisées circulairement droite et gauche. Des changements dans le dichroïsme circulaire vibrationnel du complexe cobalt spartéine (Co(sp)Cl2) sont présentés en tant que résultats préliminaires. La spectroscopie chirale vibrationnelle présente deux difficultés essentielles: d'une part les signaux sont sensibles à des artéfacts induits par la polarisation, d'autre part les signaux sont de faible intensité. Les artéfacts proviennent généralement de l'interaction entre une polarisation imparfaite et un échantillons non isotrope. Dans le but de limiter ces artéfacts, nous présentons un nouveau type de synchronisation entre le system laser et notre modulateur photo élastique permettant de générer une polarisation quasi parfaite. Cette technique réduit les artéfacts de polarisation de manière significative, et permet une détection multi canal des signaux chiraux. Détection normalement rendue impossible à cause des optiques contenues dans le monochromateur et sensible à la polarisation. D'autre part, afin d'amplifier la taille des signaux, une technique a été développée dans notre laboratoire qui consiste à utiliser une partie du faisceau de mesure comme oscillateur locale. Les améliorations techniques obtenues dans le cadre de la présente thèse devraient permettre l'utilisation de la spectroscopie vibrationnelle chirale transitoire pour l'étude de la structure des biomolécules.

Introduction

The development of femtosecond laser technology in the last twenty years [1] has enabled researchers to investigate reaction dynamics and to identify or characterize transition states and reaction intermediates in real time. Among those techniques, femtosecond transient absorption measurements have proven to be a successful tool [2]. In this technique, also sometimes referred to as pump-probe spectroscopy, a first ultrashort optical trigger pulse (pump) induces a transition to a higher lying electronic state, the evolution of the molecular system is then followed by absorbance changes of a second pulse (probe) tuned to electronic resonances of the electromagnetic spectrum (near-UV or visible).

Information that can be retrieved by probing electronic transitions states is, however, limited. Electronic absorption bands are usually strongly broadened owing to coupling to the fluctuating surrounding solvent and rather difficult to assign. Small molecular species are even more problematic as their electronic transitions often lie in the far-UV where solvent absorption is high. On the other hand, the vibrational spectrum contains bands associated with specific parts of the molecule and the probing of ultrafast reaction dynamics in the mid-infrared spectral region is a promising alternative to transient electronic absorption spectroscopy [3]. Vibrational spectra can be related to model structures with much greater accuracy than spectra involving electronic excitation and isotope labelling (^{13}C or ^{18}O for example) can be used to single out specific functional groups. Non-linear infrared spectroscopic techniques like two-dimensional spectroscopy are now capable of unravelling the mechanism responsible for the specific shape of an absorption band such as coupling to other transitions or inhomogeneous broadening [4, 5].

Nonetheless, when probing ultrafast reaction dynamics in the mid-infrared with absorption or Raman spectroscopy, aspects of molecular geometry are only obtained indirectly via perturbation of energy levels and selection rules. For that reason, novel techniques have been developed, such as 2D-IR spectroscopy, where information about the molecular structure is retrieved via the coupling of different vibrations, leading to cross peaks in the 2D spectrum [6]. A related method that is intrinsically sensitive to molecular structure and coupling is chiral spectroscopy [7]. Chiral spectroscopy is based on optical activity. Optical activity comprises many different phenomena which can all be reduced to the common origin of a different response to right- and left-circular polarised light. Optical activity is a uniquely sensitive probe of molecular stereo-chemistry, both conformation and absolute configuration (R or S), but unlike X-ray crystallography for example, it can be applied to liquids.

Among the different chiral spectroscopic techniques, circular birefringence (CB) and circular dichroism (CD) appear to be the most powerful tools to unravel molecules absolute configuration and conformation. CD measures the difference in absorption between left- and right-circular polarised light. Its variation with wavelength is known as CD spectroscopy. CB measures the difference in refraction between left- and right-circular polarised light and is often referred to as optical rotation (OR) as this difference can be related to a rotation of the plane of polarisation of linearly polarised incident light. The variation of OR with wavelength is known as optical rotatory dispersion (ORD). Both CD spectroscopy and ORD are sensitive to chirality, which exists when a molecule is non-superposable on its mirror image. Although OR was discovered in 1811 far before CD [8] and commercial polarimeters (apparatus which measure optical rotation at a single wavelength, mainly the sodium D-line) are routinely used to determine the purity of optically active substances, ORD spectroscopy did suffer a lack of interest compared to CD spectroscopy for conformation and absolute configuration determination. Despite the fact that CD and OR theoretically access the same information (CD spectra are related to ORD via the Kronig-Kramers transformation [9] page 160), the dispersive nature of ORD, which can be observed far away from an absorption band, is probably the reason why CD spectroscopy has been more exploited. Indeed, CD signal only occurs within an absorption band and is therefore, a more specific probe than ORD where contributions coming from many transitions have to be taken into account.

The sensitivity to chirality made electronic ORD and CD spectroscopy widely used tools for enantiomeric purity and absolute configuration determination [10]. CD spectroscopy is also routinely used in the determination of the secondary structure of proteins. CD signals can be seen when the electric transition dipole moment of one chromophore couples to the magnetic transition dipole moment of a second chromophore, this mechanism gives rise to the characteristic CD signals of α-helices, β-sheets and turns in proteins in the UV spectral range [11].

A great technical difficulty associated with optical activity spectroscopy is the small signal size accounting to only 10^{-2} to 10^{-5} of the underlying absorption band as well as the possible large polarisation artefacts coming from linear dichroism and birefringence [12]. Not surprisingly, there have only been a few attempts in the past to use chiral spectroscopy for probing transient species on ultrafast time scales, despite a very early implementation of transient CD technique by Xie and Simon in the visible spectral range [13]. Today, thanks to much better stability of the light sources available and increasingly sensitive detectors, those measurements appeared more feasible. Kliger and co-workers could, for example, study the dissociation of CO from haemoglobin with nanosecond resolution using transient ORD spectroscopy [14]. Using the same technique, they more recently probed the kinetics of helix folding of an azobenzene cross-linked peptide [15]. In parallel, using transient electronic spectroscopy, Hache and co-workers could detect previously unknown picosecond dynamics after photo-dissociating CO from Myoglobin [16].

Electronic spectra are less structured than vibrationals and absorption bands of chromophores often lie in the near-UV region where solvent absorption can be problematic. This is also true for chiral electronic spectra. Probing optical activity in the mid-IR (referred as vibrational optical activity (VOA)) where the spectra are more resolved and isotope labelling can be taken advantage of, is very appealing. There is unfortunately a price to pay: Not only are the chiral vibrational signals smaller by one or two orders of magnitude, but detectors are also much less sensitive than in the UV/visible. Nonetheless, realizing the potential of vibrational circular dichroism spectroscopy (VCD) and vibrational optical rotatory dispersion (VORD), lots of efforts have been put into technical developments during the last 30 years [17]. Nowadays, commercial VCD spectrometers are available and VCD spectroscopy is of growing interest for different applications such as conformational analysis of biomolecules or determining the enantiomeric purity or the absolute configuration (R or S) of organic compounds [18,19]. As VCD signal can appear due to the coupling of two achiral chromophores arranged in a chiral configuration, it allows one to gain information about the secondary structure of peptides via the arrangement and coupling of amide I (C=O stretch) transition dipole moments. VCD spectroscopy in combination with isotope labelling has, for example, successfully been used by Keiderling and co-workers to distinguish helical from unfolded domains in a polypeptide [20]. Moreover, one can now rely in the mid-infrared on particularly accurate *ab initio* modelling [21,22]. Time-resolved vibrational chiral spectroscopy could thus play a key role in unravelling the mechanisms of important biological or chemical processes, by monitoring the structural evolution of biomolecules or chiral molecules during a reaction. It remains nonetheless, a challenge.

We describe here the technical developments of a setup capable of recording transient chiral spectroscopy in the mid-infrared spectral range, where the advantages of probing vibrational transitions can be fully utilized. The method we implemented consists of taking the difference between left- and right-circular polarised pulses to compute the VCD after photo-triggering a reaction by a pump pulse. This shot-to-shot technique is the most intuitive way for measuring time-resolved (vibrational) CD and ORD. Due to the technical challenges expected, we concentrated on a model system chosen for its exceptionally high VCD signals in the electronic ground state. The VCD signals of the open shell transition metal complexes with the chiral ligand (-)-sparteine (sp), Co(sp)Cl_2 and Ni(sp)Cl_2, are approximately 10 times stronger than that of the closed shell complex Zn(sp)Cl_2 [23]. It has recently been shown theoretically that the closeness of electronically and vibrationally excited states lead to new important non Born-Oppenheimer corrections terms, which cause this unusual VCD enhancement [24, 25].

We could synthesize those metal complexes by standard procedures [26] and record VCD changes of several μ OD after visible excitation on a picosecond time-scale using the Co(sp)Cl_2 molecule. Although, those measurements were, to our knowledge, the first transient vibrational chiral signals ever recorded, technical improvements of the set-up are necessary before being able to investigate more complex systems like peptides or proteins. Artefacts are in static and transient chiral spectroscopy a major issue [27–29]. In particular, large linear dichroism signals (anisotropic absorption) might appear when imperfect probe polarisation interacts with an anisotropic sample [12]. Imperfect probe polarisation can originate from the modulation device itself or from imperfect optics placed before the sample Isotropy of the sample can be broken by the pump beam.

In our set-up, polarisation modulation is achieved by a photo elastic modulator (PEM) [30] to which our laser system is electronically synchronized. The synchronization is designed so that each pulse crosses the modulator each time it acts exactly as a waveplate, with opposite sign for consecutive mid-IR pulses. The PEM retardation (i.e. the amplitude of the crystal oscillation) can be adjusted so that the modulator acts as a quarter waveplate generating left- and right-circular polarised light to probe circular dichroism, or as a half waveplate generating linearly polarised pulses to probe optical rotation. We developed a special synchronisation scheme where polarisation imperfections originating from the modulator or optics before the sample can be drastically reduced ensuring an almost perfect probe beam polarisation state and reducing possible artefacts. The method consist of compensating the residual static birefringence of the modulator or the stress induced birefringence of the optics placed before the sample by slightly adjusting the time delay when each pulse crosses the modulator and the output polarisation produced is then carefully analysed.

Vibrational chiral signals are unfortunately very small. Although great care is accorded to the infrared light source stability and to the choice of high sensitivity low noise detectors, signal size remain an issue in VCD/VORD experiments. Nonlinear IR spectroscopy suffers similar difficulties. There, in order to record very tiny third order responses of IR chromphores, one uses heterodyne detection where weak signals interfere with a much stronger reference field also called local oscillator [31]. In chiral spectroscopy, the free induction decay (FID) that gives rise to CD and ORD is polarised perpendicular to the incident field so that the two can be separated using polarisers. The chiral FID signal can interfere with a strong reference leading to signal enhancement. Rhee *et al.* [32] for example, proposed a set-up where the local oscillator, a replica of the probe pulse itself, is guided around the sample and interfere on the detector with the chiral FID.

Based on the same principle, the set-up we propose is somehow closer to the quasi-null technique implemented by Kliger and co-workers for transient CD and ORD in the visible/UV region [33,34]. Vibrational circular dichroism spectra are recorded using elliptical polarised (instead of circular polarised) ultrashort pulses. The short polarisation axis of the elliptical light acts as the phase-locked local oscillator. This leads to VCD signals that increase linearly with the ellipticity of the probe pulses and enhanced signal to noise. An analogous scheme allows for ORD measurements.

Another way to increase the signal to noise ratio is to decrease the noise level. Most of the dispersive static chiral spectrometers (so as our spectrometer built to record transient vibrational chiral signals) disperse the light before the sample doing a one color experiment [17], scans are then taken rotating the monochromator's grating. In addition to the loss in averaging time, low frequency noise (drifts of the detector's bias current for example) are easily picked up during this process. Besides, the time resolution of a pump probe experiment is, in principle, only limited by the duration of the laser pulses (typically 100 fs in our case), spectrally narrowing the probe pulses reduces the time resolution to a few picoseconds. Dispersing the probe beam after the sample and performing multichannel detection would be a much more interesting alternative affording single shot correlated noise spectra and regaining a femtosecond time resolution. Until now, dominating artefacts coming from polarisation sensitive optics of the monochromator (grating, concave mirrors etc.) have prevented array detection. Thanks to the very good control of our polarisation, we could convert, after the sample, the probe pulses into a well-defined linear polarisation states and disperse them onto a multichannel array detector. Full ORD spectra (200 cm^{-1} bandwidth) in the C-H stretch region of the terpene molecule limonene could be recorded within few minutes. All the technical developments described above should make transient vibrational chiral spectroscopy a new interesting tool to unravel ultrafast process in biological systems.

The following thesis is into five Chapters divided: Chapter 1 introduces vibrational chiral spectroscopy from the basic phenomenon of optical activity to chiral vibrational spectrometers. Chapter 2 describes in details the set-up built to record the transient vibrational chiral signals. Chapter 3 explains the synchronisation between the modulator and the laser system and how the control of the probe polarisation is achieved. Chapter 4 presents the transient VCD signals obtained with the Co(sp)Cl$_2$ metal transition complex. Chapter 5 presents the self heterodyning chiral signal enhancement technique in combination with multichannel ORD detection. Finally, an introduction to the mathematical description of light polarisation (Jones vectors, Stokes calculus etc.) useful to understand the calculations done in this document can be found as an appendix.

Chapter 1

Chiral infrared spectroscopy

1.1 Optical activity

1.1.1 Phenomenological description

Optical activity (OA), comprises the set of phenomena originating in differences in optical properties for left- and right-circular polarised radiation. In the absence of an external additional magnetic field, optical activity arises from chirality, which exists when a material or molecule cannot be superimposed with its mirror image; the two images are called enantiomers or optical isomers. Many biologically active molecules are chiral (including the naturally occurring amino acids and sugars) making chirality one of the most important features of the biological world [35].

Optical activity regroups two closely related phenomena: **Circular birefringence** (CB), which can be attributed to unequal refraction of left- and right-circular polarised light (CB is more known as **optical rotation** (OR) due to its ability to rotate the plane of polarisation of linearly polarised light) and **circular dichroism** (CD), which is the difference in absorption of left- and right-circular polarised light. Pictorially, if we send linearly polarised light onto a circular birefringent medium, its plane of polarisation will rotate by an angle δ (see Figure 1.1 Top). This angle δ is a measure of the refraction difference between the two left- and right-circular states. On the contrary, if we send the same linear incident polarisation onto a circular dichroic medium, the output polarisation will be elliptical (see Figure 1.1 Bottom), the ellipticity angle η being a measure of the absorption difference between the two left- and right-circular states. The measurement of the wavelength dependence of circular dichroism is called CD spectroscopy; the measurement of the wavelength dependence of optical rotation is called optical rotatory dispersion (ORD). Both those techniques are usually regrouped under the label chiral spectroscopy [1].

---

[1] In the literature, nonetheless, other techniques are often also categorized under chiral spectroscopy [7, 36]: Fluorescence detected circular dichroism [37] (FDCD) which is the detection of electronic absorption

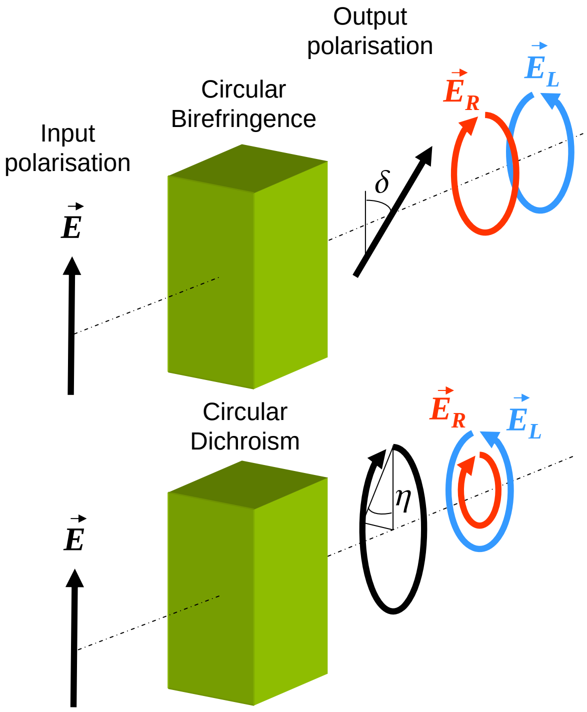

Figure 1.1: Pictorial representation of optical activity. Top: Circular birefringence is the velocity difference (refraction) in the medium between left- and right-circular polarised light (represented by coloured arrows). The result is a rotation of the plane of polarisation of linearly polarised light (black arrow). Bottom: Circular dichroism is the absorption difference in the medium between left- and right-circular polarised light. The result is an elliptical output polarisation.

Chiral spectroscopy can be divided into two sub-units: Electronic chiral spectroscopy when electronic transitions are probed by visible or UV light and infrared chiral spectroscopy when vibrational transitions are excited. In the latter, circular dichroism is then referred to as vibrational circular dichroism (VCD) as optical rotatory dispersion becomes vibrational optical rotatory dispersion (VORD) [2].

Optical activity is not a new discovery and has been fascinating many scientists since almost 200 years. Optical rotation was the first manifestation to be observed by the french physicist Arago, who discovered that crystal quartz could rotate the plane of polarisation of light [8]. This property was also found few years later in other non crystalline natural substances, liquid and vaporous, like turpentine (a liquid obtained from resin distillation

---

CD through a measurement of the total fluorescence associated with the absorbed CD intensity. Circular polarised luminescence [38] (CPL), in this technique the sample is excited at typically a single wavelength without polarisation modulation and the observed luminescence, either fluorescence or phosphorescence, is measured for its intensity difference with respect to right- and left-circular polarised states.

[2] Vibrational Raman optical activity [39] (VROA) which is the difference in intensity of Raman scattered right- and left-circular polarised light is also often categorized under chiral vibrational spectroscopy but will not be discussed here.

and mainly containing pinene) by Biot [40] who defined the **specific rotation** (the rotation angle per unit length of path) and the notions of **positive/negative rotation**: The rotation is called positive if the plane of polarisation is turned in a clockwise direction as viewed by an observer toward whom the light is propagating and negative for an anti-clockwise rotation.

Units Circular birefringence is usually measured as a specific rotation $[\delta]$ which is the angle of rotation (in degree) divided by the concentration (in g/mL) times the cell length (in cm). For circular dichroism, ellipticity is the historically unit and is defined as the tangent of the ratio of the minor to the major elliptical axis. The specific ellipticity $[\eta]$ is given by the ellipticity (in radian) divided by the sample concentration (in mol/L) times the path length (in cm). Although radian units persist, in most cases CD is now measured by taking the difference in absorption of right- and left-circular polarised light and the relevant unit used is the molecular circular dichroism or $\Delta\varepsilon$ (in L/mol/cm) which is the difference between the two molar extinction coefficients ε_l,ε_r for each polarisation state. The relation between the specific ellipticity and the delta epsilon is

$$[\eta] = 3298 \times \Delta\varepsilon. \tag{1.1}$$

1.1.2 Fresnel cinematic model

The first attempt to explain theoretically optical activity was done by Fresnel and is referred to as the cinematic theory of optical activity [41]. Noticing that linearly polarised light could be decomposed into the sum of left- and right-circular beams, Fresnel was able to explain optical rotation by a difference of the indexes of refraction for each circular polarisation states. He wrote down an expression for the rotatory power δ (in radians) of a substance [3]

$$\delta = \frac{\pi}{\lambda}(n_l - n_r)L. \tag{1.2}$$

Where λ is the vacuum wavelength, n_l, n_r are the refractive indices for left- and right-circular polarised light and L the sample length. If the angle δ is positive, the substance is said to be dextrorotatory or (+), if δ is negative the sample is said to be levorotatory or (-).

Although the cinematic theory only explains optical rotation (circular dichroism had not been observed at that time), Fresnel was the first to notice that optical activity was related to a different response to right- and left-circular polarised light.

The discovery of circular dichroism, the difference of absorption between left- and right-

---

[3] For more details about the Fresnel cinematic theory, see the reference [42]

circular polarised light, happened later with Cotton [43] in 1896 (CD is sometimes still refereed as to the Cotton effect in the literature in the case of an isolated absorption band). We know from basic electromagnetic theory that the index of refraction is, in fact, a complex value whose real part is related to refraction and whose imaginary part to absorption.

$$n = a + ib. \tag{1.3}$$

If OR is related to a refraction difference between left- and right-circular polarised light, so to the difference between the real parts of the refraction indexes

$$\delta = \frac{\pi}{\lambda}(a_l - a_r)L. \tag{1.4}$$

CD can be related to a difference of the imaginary part of the refraction indexes for left- and right-circular polarised light [44]

$$\eta = \frac{1}{4}(b_l - b_r)L. \tag{1.5}$$

1.1.3 Electromagnetic theory

After introducing Fresnel cinematic theory in the last paragraph, we turn now to the problem of generalizing the electromagnetic theory to introduce optical activity.
We start from the Maxwell equations for a medium containing no charges nor currents [45].

$$\left.\begin{aligned} &\nabla \cdot \vec{D} = 0, \\ &\nabla \cdot \vec{B} = 0, \\ &\nabla \times \vec{E} = -(1/c)\frac{\partial \vec{B}}{\partial t}, \\ &\nabla \times \vec{H} = (1/c)\frac{\partial \vec{D}}{\partial t}. \end{aligned}\right\} \qquad \text{Maxwell equations}$$

Where $\vec{E}$ and $\vec{H}$ are the electric and magnetic field, $\vec{D}$ and $\vec{B}$ are the electric and magnetic induction and c is the celerity of light in vacuum. Next to the Maxwell equations, the constitutive equations link the fields and inductions to the electric and magnetic moments per unit volume $\vec{P}$ and $\vec{I}$ [45]

$$\left.\begin{aligned} &\vec{D} = \vec{E} + 4\pi\vec{P}, \\ &\vec{B} = \vec{H} + 4\pi\vec{I}. \end{aligned}\right\} \qquad \text{Constitutive equations}$$

The connection between the electric and magnetic moments and the electric and magnetic fields takes the form for simple isotropic media

$$\vec{P} = \kappa \vec{E}, \tag{1.6}$$
$$\vec{I} = \kappa^{'} \vec{H}. \tag{1.7}$$

where κ and $\kappa^{'}$ are scalars. The constitutive equations then become

$$\vec{D} = (1 + 4\pi\kappa)\vec{E} = \epsilon\vec{E}, \tag{1.8}$$
$$\vec{B} = (1 + 4\pi\kappa^{'})\vec{H} = \mu\vec{H}. \tag{1.9}$$

Where we defined ϵ the dielectric constant and μ the magnetic permeability. Solving the Maxwell equations for the electric and magnetic field leads to the Helmholtz equation and the classical definition of the index of refraction $n = \sqrt{\epsilon\mu}$. As in general, $\kappa^{'} \approx 10^{-4}\kappa$ except for strongly magnetic substances, the index of refraction can be defined as $n = \sqrt{\epsilon}$.

How to modify the constitutive equations to introduce optical activity The constitutive equations mean that the electric induction $\vec{D}$ originates only from the applied electric field $\vec{E}$ enhanced by the dielectric constant ϵ, as the magnetic induction $\vec{B}$ originates only from the magnetic field $\vec{H}$ enhanced by the permeability μ.
Nonetheless, Maxwell differential equations show that a time varying magnetic field produces an electric field and vice versa; yet no corresponding terms appear in the constitutive equations. Drude was the first to propose to modify those to describe optically active media [46], followed by Born et Fedorov [47]. In order to describe an optically active medium, the constitutive equations have to be modified introducing new source terms [44]

$$\vec{D} = \epsilon\vec{E} - g\frac{\partial\vec{H}}{\partial t}, \tag{1.10}$$
$$\vec{B} = \mu\vec{H} + g\frac{\partial\vec{E}}{\partial t}. \tag{1.11}$$

where we introduced g, a macroscopic unitless constant not determined yet.
If we assume that the fields are plane monochromatic waves of the form $\vec{X} = \vec{X}_0 e^{i\psi} = \vec{X}_0 e^{i2\pi\nu(t - n\vec{k}\cdot\vec{r}/c)}$, then equations $\nabla \cdot \vec{E} = 0$ and $\nabla \cdot \vec{B} = 0$ become $\vec{k} \cdot \vec{D} = 0$ and $\vec{k} \cdot \vec{B} = 0$ and $\vec{D}$ and $\vec{B}$ are transverse vectors.
Similarly, the $\nabla\times$ equations become

$$n\vec{k} \times \vec{E} = \vec{B}, \tag{1.12}$$

$$n\vec{k} \times \vec{H} = -\vec{D}. \tag{1.13}$$

and the constitutive equations

$$\vec{E} = \epsilon^{-1}\vec{D} + i\gamma\vec{B}, \tag{1.14}$$

$$\vec{H} = \vec{B} - i\gamma\vec{D}. \tag{1.15}$$

with $\gamma = 2\pi\nu g\epsilon^{-1}$. Eliminating the electric and magnetic fields from 1.12 and 1.13, we get

$$n(\epsilon^{-1}\vec{k} \times \vec{D} + i\gamma\vec{k} \times \vec{B}) = \vec{B}, \tag{1.16}$$

$$n(-i\gamma\vec{k} \times \vec{D} + \vec{k} \times \vec{B}) = -\vec{D}. \tag{1.17}$$

Remembering that $\vec{D}$ and $\vec{B}$ are transverse vectors and can be expressed in a orthonormal (x, y, z) basis as $(D_1, D_2, 0)$ and $(B_1, B_2, 0)$ z being the direction of propagation, equations 1.16 and 1.17 are a system of four equations with four unknowns, which determinant needs to be zero to have solutions

$$det \begin{pmatrix} -1 & -in\gamma & 0 & -n\epsilon^{-1} \\ -in\gamma & -1 & -n\epsilon^{-1} & 0 \\ 0 & -n & 1 & ni\gamma \\ n & 0 & -ni\gamma & 1 \end{pmatrix} = 0. \tag{1.18}$$

Solving this system gives $n^{-2} = (\epsilon^{-1/2} \pm \gamma)^2$. The two negative roots correspond to propagation in the direction $-\vec{k}$ and are not of interest. The two positive roots correspond to propagation in the direction $\vec{k}$. The root with positive sign for γ can be easily seen to correspond to a solution for $\vec{D}$ and $\vec{B}$ of the form of right-circular polarised wave as the other to left-circular polarisation. γ being small compared to unity, it follows

$$n_r = \sqrt{\epsilon} - 2\pi\nu g, \tag{1.19}$$

$$n_l = \sqrt{\epsilon} + 2\pi\nu g. \tag{1.20}$$

The rotation angle δ defined phenomenologically by Fresnel (see equation 1.2) becomes

$$\delta = \frac{\pi}{\lambda}(n_l - n_r)L = \frac{4\pi^2}{\lambda^2}cg. \tag{1.21}$$

Microscopic origins of β The next step is to see what kind of response of the individual molecules to the fields of the light wave is needed to give terms in the macroscopic field equations 1.10 and 1.11. We can define the microscopic electric and magnetic moments, $\vec{p}$ and $\vec{m}$ for a medium containing N molecules per unit volume as

$$\vec{P} = N\vec{p}, \tag{1.22}$$

$$\vec{I} = N\vec{m}. \tag{1.23}$$

The microscopic electric moment is classically linked to the electric field via the polarisability α, $\vec{p} = \alpha\vec{E}$, as the microscopic induced magnetic moment is equal to zero $\vec{m} = \vec{0}$ for not too strong magnetic substances.
Suppose we modify those relations introducing new sources terms

$$\vec{p} = \alpha\vec{E} - (\beta/c)\frac{\partial\vec{H}}{\partial t}, \tag{1.24}$$

$$\vec{m} = (\beta/c)\frac{\partial\vec{E}}{\partial t}. \tag{1.25}$$

A quick comparison with Equation 1.11 and 1.10 leads to a definition of α, familiar from the ordinary theory of dispersion and to a similar definition for the parameter g

$$\epsilon = (1 + 4\pi N\alpha), \tag{1.26}$$

$$g = \frac{16\pi^3 N}{\lambda^2}\beta. \tag{1.27}$$

We can then get a direct connection between the rotatory power δ and the molecular parameter β

$$\delta = (\frac{16\pi^3 N}{\lambda^2})\beta. \tag{1.28}$$

This is the main result of the electromagnetic theory, it refers the optical activity of the medium to the microscopic parameter β [44].
In the next section, using molecular theories, we will explicitly evaluate the parameter β. Briefly, it will be shown that β is given by

$$\beta_a = \frac{c}{3\pi h} \sum_b \frac{R_{ba}}{\nu_{ba}^2 - \nu^2}. \tag{1.29}$$

where β_a is the value of β for a molecule in quantum state a, ν_{ba} is the frequency of the light absorbed in the jump $a \rightarrow b$ and R_{ba} is a constant characteristic of this transition and is called the **rotational strength**. Equation 1.29 is called the **Rosenfeld equation** [48] and is equivalent to the well known dipole strength equation which links the polarisability α_a of the molecule in the quantum state a to the dipole strength D_{ba} of a transition

$$\alpha_a = \frac{2}{3h} \sum_b \frac{\nu_{ba} D_{ba}}{\nu_{ba}^2 - \nu^2}. \tag{1.30}$$

Before going to the Rosenfeld equation derivation, a naive pictorial representation to understand the origin of the parameter β consists to think of electrons in the medium constrained to move on a helical pathway during a transition (see Figure 1.2).

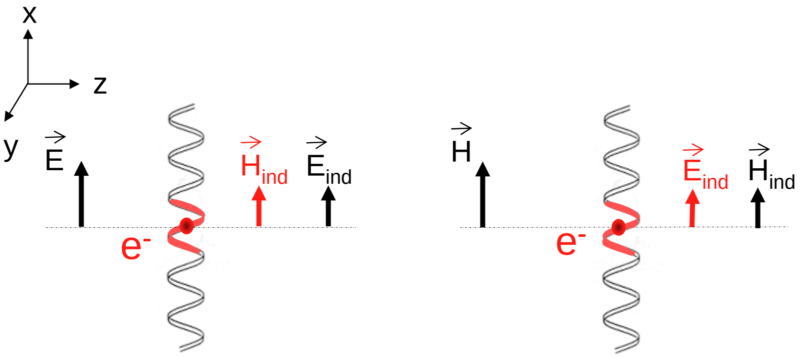

Figure 1.2: Origin of the coupling parameter β. Electrons are obliged to move on a helical path, motion of the electrons in the E field direction causes a circular current and hence a magnetic field. Adapted from Hecht [49] (page 379)

Indeed, when put into an electric field, the positive charges of the medium are displaced in the direction of $\vec{E}$ as the negative charges are displaced in the opposite way creating a dipole moment proportional to the strength of the electric field. If these flowing charges are now obliged not to move directly from their initial to their final positions but are constrained to move in somewhat helical paths, there is a circulatory component of motion around $\frac{\partial \vec{E}}{\partial t}$, accompanying the general forward motion in the direction of $\vec{E}$. The current associated with the circulatory component of the motion give rise to a magnetic moment that is proportional to the amount of $\frac{\partial \vec{E}}{\partial t}$ and in the same direction as $\vec{E}$. This is a simple pictorial view of the mechanism underlying the term involving β in the equation for the induced magnetic moment. Similarly, a varying magnetic field gives rise to induced currents in the molecule. The same helical constraints will require a displacement of positive charges in one direction and negative ones in the opposite direction giving rise to an induced electric moment. This is the mechanism underlying the term involving β in the equation for the induced electric moment [4]

1.1.4 The Rosenfeld equation

Many attempts have been done to derive the parameter β from a molecular basis at the beginning of the last century [51–53]. It was already noticed that the calculation of β depends essentially on taking into account the finite ratio of the molecular diameter to the wavelength of the wave, or rephrasing it: The phase of the light wave has to be different for different parts of the molecule for optical activity to appear. The full quantum mechanical calculation of β, which has been briefly introduced in the last section, was first formulated by Rosenfeld [48]. We briefly highlight the important points of its derivation in the next paragraph.

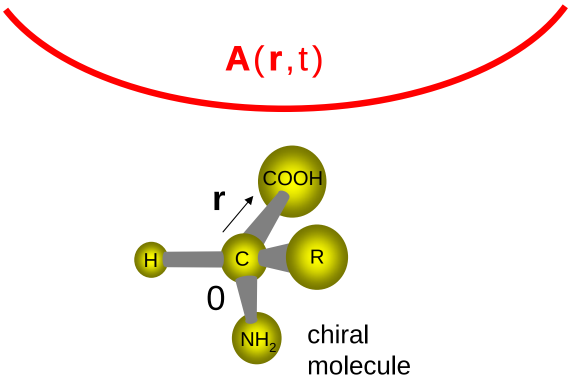

Figure 1.3: Schematic representation of a chiral molecule in an electro-magnetic field. To model optical activity, we have to take into account the spatial variation of the electromagnetic field over the molecule.

Consider a molecule perturbed by an electromagnetic radiation. We have to find how the wave-function for the molecule in a particular quantum state a is affected by the perturbation. If Ψ is the wave-function of the perturbed molecule, we have to solve the Hamilton equation

$$i\hbar\frac{\partial\Psi}{\partial t} = (\hat{\mathcal{H}}_0 + \hat{\mathcal{H}}_{int})\Psi. \tag{1.31}$$

In which $\hat{\mathcal{H}}_0$ is the field-free zero-order Hamiltonian [54](page 45)

---

[4] This representation of optically active molecules as helical conductors is well worth keeping in mind. As an example, if we direct a linearly polarised microwave beam onto a box filled with a large number of identical copper helices (e.g., 1 cm long by 0.5 cm in diameter and insulated from each other), the transmitted wave will undergo a rotation of its plane of polarisation [50].

$$\hat{\mathcal{H}}_0 = -\frac{\hbar^2\nabla^2}{2m} + \hat{V}. \tag{1.32}$$

With $\hat{V}$ the potential energy operator and $\hat{\mathcal{H}}_{int}$ the field-dependent perturbation Hamiltonian operator defined as

$$\hat{\mathcal{H}}_{int} = -\frac{q}{m}\vec{A} \cdot \frac{\hbar\nabla}{i}. \tag{1.33}$$

Where $\vec{A} = \vec{A}_0 e^{i(t-\vec{k}\cdot\vec{r}/c)E/\hbar}$ is the vector potential ($E = h\nu$ is the quantum energy associated with the wave), m is the molecule mass and q its charge.
The size of a molecule is typically much smaller than the wavelength of the light in spectroscopy so that, as an approximation, we can usually neglect the spatial dependence r of the potential vector

$$\vec{A} = \vec{A}_0 e^{-i\omega t} e^{i\vec{k}\cdot\vec{r}} \approx \vec{A}_0 e^{-i\omega t}. \tag{1.34}$$

leading to an interaction Hamiltonian

$$\hat{\mathcal{H}}_{int} = -e^{-i\omega t}\frac{q}{m}\vec{A}_0 \cdot \frac{\hbar\nabla}{i}. \tag{1.35}$$

Reformulating the Hamiltonian in terms of the electric field vector $\vec{E}$ instead of the vector potential gives [54] (pages 96-97)

$$\hat{\mathcal{H}}_{int} = -\hat{p} \cdot \vec{E}. \tag{1.36}$$

where $\hat{p}$ is the electric dipole moment operator.
Solving equation 1.31 with such an spatial independent vector potential leads to the definition of the isotropic polarisability α_a [55] (page 49)

$$\alpha_a = \frac{2}{3h}\sum_b \frac{\nu_{ba}|\langle a|\hat{p}|b\rangle|^2}{\nu_{ba}^2 - \nu^2} = \frac{2}{3h}\sum_b \frac{\nu_{ba}D_{ba}}{\nu_{ba}^2 - \nu^2}. \tag{1.37}$$

where $\langle a|\hat{p}|b\rangle$ is the transition dipole moment between the state a and an excited state b, ν_{ba} is the frequency of the radiation associated with the transition and D_{ba} is the dipole strength.
On the other hand, optical activity originates from chirality. To model it, it is then intuitive to take into account the spatial dependence of the field over the molecule so that its asymmetry can be probed (see Figure 1.3). Taking the two first terms of the vector potential expansion

$$e^{i\vec{k}\cdot\vec{r}} \approx 1 + (i\vec{k}\cdot\vec{r}) + \frac{1}{2}(i\vec{k}\cdot\vec{r})^2 + \cdots . \tag{1.38}$$

leads to an interaction Hamiltonian of the form

$$\hat{\mathcal{H}}_{int} = -\frac{q}{m}\vec{A}_0[1 + i\vec{k} \cdot \vec{r}]e^{-i\omega t} \cdot \frac{\hbar\nabla}{i}. \tag{1.39}$$

Reformulating the interaction Hamiltonian as a function of the electric and magnetic fields $\vec{E}$ and $\vec{H}$ gives [54] (pages 96-98)

$$\hat{\mathcal{H}}_{int} = -\hat{p} \cdot \vec{E} - \hat{m} \cdot \vec{H}. \tag{1.40}$$

where we introduced $\hat{m}$, the magnetic dipole moment operator and we neglected the electric quadrupolar interactions (see Appendix).
Expressing the electric and magnetic dipole moments as a function of $\vec{H}$ and $\vec{E}$ and comparing them with equations 1.24 and 1.25 gives for β [55] (pages 68-78)

$$\beta = \frac{c}{3\pi h}\sum_b \frac{Im\{\langle a|\hat{p}|b\rangle \cdot \langle b|\hat{m}|a\rangle\}}{\nu_{ba}^2 - \nu^2} \tag{1.41}$$

where Im stands for the imaginary part of the terms between the curly brackets, p and m are electric and magnetic dipole moment operator, ν_{ab} is the frequency of the radiation associated with the transition $a \rightarrow b$. Equation 1.41 is the Rosenfeld equation [48]. The term $Im\{\langle a|\hat{\mu}|b\rangle \cdot \langle b|\hat{m}|a\rangle\}$ is called the rotational strength R_{ba}.

1.1.5 General properties of the rotational strength

Chirality From equation 1.41, we see that the simplest chiral electronic displacement which can give rise to optical activity is along an helical path, which implies a simultaneous translation and rotation of charge, that is a transition with $\langle a|\hat{\mu}|b\rangle \neq 0$ and $\langle b|\hat{m}|a\rangle \neq 0$ and for which the two vectors are not orthogonal. In addition, it is apparent that the rotational strength is a signed quantity. R_{ba} has equal absolute values but opposite in sign for each mirror image arrangements [44].

The Sum rule The summation over all electromagnetic transitions of the rotational strength is equal to zero [44]

$$\sum_b R_{ba} = 0. \tag{1.42}$$

Experimentally, if we see a positive band in the CD or ORD spectrum, we can expect one or more bands of negative sign somewhere else.

Relation with experimental quantities The rotational strength, as the dipole strength, can be related to experimental quantities. The dipole strength D_{ba} is proportional to the integrated infrared spectrum

$$D_{ba}(cgs\ units) = \frac{6909hc}{8\pi^3 N_0}\int(\frac{\varepsilon}{\lambda})d\lambda = 9.18\times 10^{-39}\int(\frac{\varepsilon}{\lambda})d\lambda. \tag{1.43}$$

where ε is the wavelength dependant molar extinction coefficient (in L/mol/cm); as the rotational strength is proportional to the integrated CD spectrum

$$R_{ba}(cgs\ units) = \frac{6909hc}{32\pi^3 N_0}\int(\frac{\Delta\varepsilon}{\lambda})d\lambda = 2.29\times 10^{-39}\int(\frac{\Delta\varepsilon}{\lambda})d\lambda. \tag{1.44}$$

where $\Delta\varepsilon$ is molar circular dichroism (in L/mol/cm).
Kuhn introduced the g-factor, sometimes also called anisotropy or dissymmetry factor, defined as [53]

$$g_{ba} = \frac{R_{ba}}{D_{ba}}. \tag{1.45}$$

g_{ba} is a measure of the importance of a line in contributing to optical activity.

1.2 Vibrational optical activity

1.2.1 Advantages of probing vibrational transitions

Until the early 70's, essentially all ORD and CD spectra were measured in the visible and near UV and were attributable to electronic transitions. In the case of organic molecules and bio-polymers (which are heavily studied with chiroptical techniques) the number and type of transitions that could be studied with chiral spectroscopy was limited. Indeed, they mainly reduce to molecules containing a chromophore and in most of the cases the chromophore is achiral and the chiral signal comes from the perturbation of the chromophore by its environment. Structure sensitivity of the technique is lost as structural information becomes a higher order effect. If most of the organic compounds have only few accessible chromphores in the visible/UV region, they all posses extensive IR absorption spectra. Chiroptical variants of IR absorption techniques can be used to derive molecular structural information from all of these states. Vibrational spectra are usually much more structured than electronic spectra, providing a more local probe of conformation. Site selectivity can be further enhanced by ^{13}C (and/or ^{18}O) isotope labelling. Finally, reliable *ab initio* calculations are now available in the mid-IR [21, 22]. The obvious method of measuring vibrational optical activity (VOA) is by extending optical rotatory dispersion and circular dichroism into the infrared. However, in addition to the technical difficulties in manipulating polarised infrared radiation, there is a fundamental physical difficulty. Theoretically, the rotational strength of a vibrational transition should be three to four orders of magnitude smaller than for electronic transitions. Nonetheless, as the sensitivity is determined by the asymmetric ratio of the rotational strength over the dipole strength $g = \frac{4R}{D}$ and as vibrational transitions have a dipole strength two to three orders of magnitude lower than electronics, vibrational optical activity is still a measurable quantity. The first measurements of vibrational optical activity were, in fact, achieved very early by Biot [40] in 1835 who sent linearly polarised infrared light along the optical axis of a column of quartz. Nonetheless, the optical rotation he observed originated probably mainly from near infrared electronic transitions. Progress in vibrational optical activity were then slow. In 1972, Schrader and Korte reported the first liquid phase vibrational optical rotatory dispersion spectrum (VORD) of cholesteric liquid crystals [56], almost at the same time Dudley and Chabay published vibrational circular dichroism spectra (VCD) of similar samples [57–59] (Vibrational optical activity is accessible in cholesteric liquid crystals because the helix pitch length is of the order of the wavelength of infrared radiation). A major step was made few years later by Holzwarth and co-workers who reported a well defined circular dichroism spectrum in the C-H and C-D stretch region for the (S)-(+)- and (R)-(-)-2,2,2-trifluoro-1-phenylethanol [60]. The publication by Nafie, Keiderling and Stephens of vibrational circular dichroism spectra down to about 2000 cm^{-1} in a number of typical optically active molecules served notice that infrared vibrational circular dichroism had become a routine technique [61]. Since then, lots of efforts have been put into technical developments. Although VCD and VORD bring the same structural information (VCD and VORD spectra are related to each other via the Kronig-Kramers transformation [9] page 160), VCD happened to dominate VORD spectroscopy. With the apparition of the first commercial VCD instruments in the late 90's, VCD became a powerful and convenient analytical tool for natural products and biomolecules, it allies the spectroscopic details or IR absorption with the stereo-chemical sensitivity of CD. Applications of vibrational optical activity can be divided into different parts: Conformational analysis, where the objective is to study the conformation in solution of selected biological molecules, mainly proteins, nucleic acids and more recently, sugars; determination of the optical purity of manufactured sample and absolute configuration ((+)-(S) or (-)-(R)) of new chiral molecules.

1.2.2 Applications of vibrational optical activity

Since the first VCD measurements reported for liquids in 70's [59, 60], vibrational circular dichroism has been applied to many fields. VCD can be used, for example, to predict enantiomeric excess (% ee) in pharmaceutical samples [62,63]. On the other hand, absolute configuration determination of synthetic or natural compounds may be the most common application [19, 64]. Figure 1.4 shows an example of the determination of the absolute configuration of the mirtazapine molecule, a pharmaceutical ingredient with antidepressant therapeutic effects, using VCD spectroscopy [65].

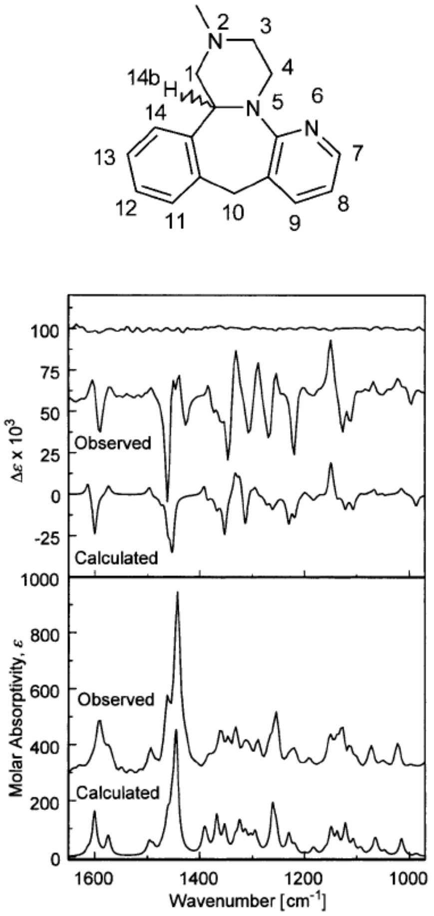

Figure 1.4: Top: Structure of the (±) mirtazapine molecule. Bottom: Observed IR and VCD spectra from the (-) mirtazapine sample in comparison to calculated spectra for the (-)-enantiomer. See original paper from Freedman *et al.* for details [65].

The absolute stereoisomery is generally established comparing the sign and frequency patterns of the observed VCD spectrum with the *ab initio* quantum chemistry calculated one [21, 22].

VCD has also been used for the conformational analysis of peptides, proteins and sugars, mainly in an empirical manner [64, 66]. The secondary structure of a peptide or protein, mainly α-helix, β-sheet or random coil is reflected in the C=O stretch (amide I) and N-H deformation (amide II) region (see Figure 1.5). The patterns of an α-helical structure, observable in a protein containing a high fraction of α-helix such as haemoglobin, consists of a positive couplet in the amide I region followed by a small negative band in the amide II region (see Figure 1.5). On the contrary, a β-sheet structure exhibits different features especially in the C=O stretch region where a β-sheet has a small negative peak around

1600 cm^{-1}. In the amide II region, β-sheet often exhibits a negative couplet. An example of a protein which secondary structure dominated by β-sheet would be concanavalin A. A random coil protein is an interesting case, it has no extensive secondary structure. It shows a negative couplet in the amide I region in which a strong negative peak appears at higher frequencies and a small broad negative peak in the amide II region.

Secondary structure determination from VCD spectra, contrary to the absolute configuration determination of smaller molecules where reliable *ab initio* calculations are available, remains a qualitative approach despite lots of progress in theoretical modelling [21,67].

Next to peptides and proteins, VCD can also be an interesting tool to determine the conformation of carbohydrates [68].

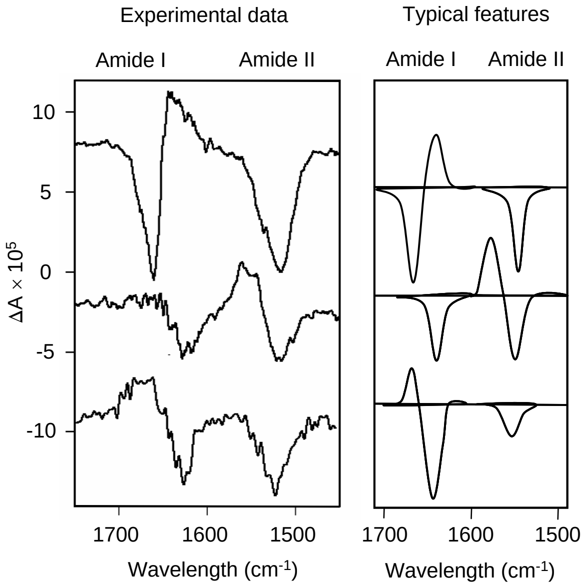

Figure 1.5: Left: Comparison of typical amide I and II VCD spectra for proteins in solution that have different dominant secondary structures. Top spectrum from haemoglobin (highly helical), middle spectrum from concanavalin A (highly β-sheet, no helix), bottom spectrum from casein (random coil protein with no extensive secondary structure). Adapted from keiderling [67]. Right: Model VCD patterns of α-helix, β-sheet and random coil structure in the amide I and II regions. The patterns can be derived from different globular proteins with dominant secondary structure fractions (adapted from Taniguchi *et al.* [64])

1.2.3 Vibrational optical activity measurements

Dispersive versus FT-IR configuration

Two main techniques are employed for VOA experiments: Dispersive and Fourier transform (FT-IR) measurement [29].

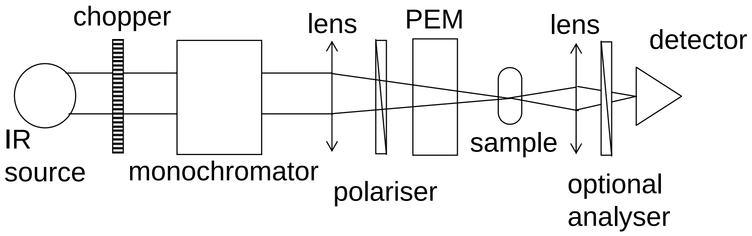

Figure 1.6: Schematic representation of a dispersive VCD/VORD set-up. Adapted from [29]. See text for details

Dispersive VCD/VORD technique Most dispersive instrumentation suitable for measurement of circular dichroism and optical rotation in the UV/Vis or in the IR, is based on the design of Grosjean and Legrand [69]. In a typical vibrational set-up [17], the broad band IR beam from a light source (Glow bar) is first directed into a monochromator (see Figure 1.6) which selects a narrow bandwidth. The monochromatic light is then focused onto a sample. Before the sample, a linear polariser followed by a photo elastic modulator (PEM) modulate the IR beam through desired states of polarisation. After passing through the sample, the beam is focused onto a detector. An optional polariser can be used for VORD measurements. The electronic signal for VCD is processed using a phase-sensitive device such as a lock-in amplifier. The first VCD dispersive set-up was built by Holzwarth and co-workers in 1972 [59].

FT-IR VCD/VORD technique In a FT-IR set-up (see Figure 1.7), the IR beam from a light source is first passed through an interferometer. A typical Michelson interferometer modulates the IR beam by creating a path difference between the two beams as they recombine at the beam splitter. The output IR beam from the interferometer then passes through a VCD optical bench which similar to dispersive set-ups. By passing through a linear polariser and a PEM, the Fourier modulated IR beam is further modulated at the PEM frequency. The doubly modulated signal is first demodulated at the PEM frequency by a lock-in amplifier, then Fourier transformed within a computer. The first FT-IR VCD set-up was developed by Nafie and co-workers [70] in 1979.

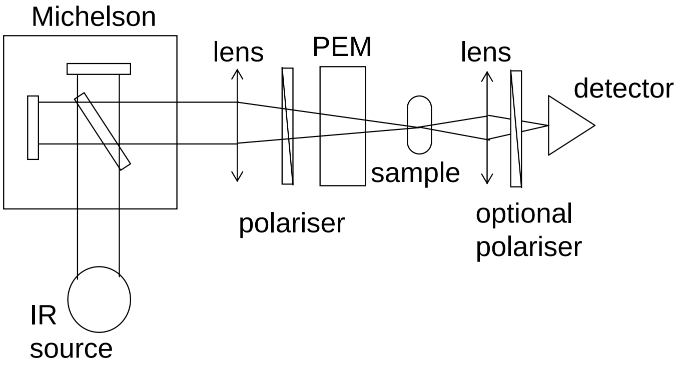

Figure 1.7: Schematic representation of a FT-IR VCD/VORD set-up. Adapted from [29]. See text for details

Comparison of the two configurations In the long run, FT-IR based VCD set-ups are likely to expand in usage due to the possibility to collect the whole mid-infrared spectrum at a reasonable resolution and in an acceptable time. Nonetheless, the most useful VCD spectra are gained on molecular species in solution where solvent absorption allows measurements only in small spectral windows. With a dispersive VCD spectrometer, single bands (e.g., C-H, N-H and O-H stretches) can be measured at a modest resolution within few minutes and averaging over several scans for sample and baseline, can be done on the time scale of one hour [17]. In those cases, dispersive VCD measurements are much more efficient than FT-IRs justifying the efforts still put into dispersive spectrometer developments [71].

Dispersive configuration in depth

Polarisation artefacts are a concern in VCD/VORD spectroscopy and great care has to be dedicated to the choice of optics. For example, ZnSe and BaF_2 lenses are now preferred over focusing mirrors as they are less sensitive to polarisation and introduce smaller artefacts [72]. For similar reasons, dispersive spectrometers are usually a one color experiment, where a monochromator select a narrow spectral bandwidth before the modulator so to limit artefacts introduced by sensitive optics (grating, concave mirrors etc..).
Typically, the most important elements of a VCD spectrometer are: The light source, the polarisers, the detection scheme and the photo elastic modulator.

The light source As typical chiral vibrational signals are 4 to 6 orders smaller than the normal absorption, intense light sources are very desirable to obtain spectra with good signal to noise ratios. Most spectrometers use the black body radiation of a glow bar source which gives satisfactory results between 1000 to 4500 cm^{-1}. Different other sources have been tried for specific wavelength ranges. A xenon arc lamp with a sapphire window has been used for VCD in the near IR up to 6 μm region with moderate results [73]. A carbon rod source has been constructed in Keiderling's laboratory for VCD experiments giving higher color temperature ($\approx$ 2400 K) and higher power (3-4 kW) than does a traditional glower IR source [17] (page 216), but its high energy consumption, short life time and the need for a cooling system prevented a commercial application. Finally, Diem has used a hot Nernst glower as a light source for dispersive VCD spectrometer [74]. The Nernst glower can reach a temperature above 3000 K but the replacement costs are relatively high and the life-time is moderate ($\approx$ 3 months). All these sources are designed to yield higher light intensity at the cost of replacement maintenance in contrast to glow bars.

The polarisers Most instruments employ wire grid polarisers, they consist of parallel metallic lines in a jail bar pattern and achieve their polarising properties through anisotropic conduction [75]. The grid are usually deposited on BaF_2, ZnSe, or other transmitting substrates. Grid polarisers provide high angular aperture as well as an adequate extinction ratio for IR radiation (A typical wire-grid made of gold with a 0.25 μm spacing, on a barium fluoride substrate will have a extinction ratio [5] of 10^{-2} at 6 μm). Free standing wire-grid polarisers without any substrate are now available increasing the usable frequency range. As a better extinction ratio is not really needed for classic VCD spectrometers, wire-grid are the most employed polarisers. Other type of polarisers have been used for special set-ups where higher extinction ratios are compulsory: Dichroic calcite polarisers can have an extinction ratio better than 10^{-8} but their working range is really narrow and absorption losses are non negligible [76]. Brewster angle polarisers are another possibility: Four germanium plates are arranged in a chevron geometry [77], input radiation is incident near Brewster angle for the first plate such that the reflected beam is preferentially s-polarised. This reflected beam is steered subsequently to the successive plates always intersecting near Brewster angle. At the output, the beam is almost completely s-polarised. Broadband extinction ratio better that 10^{-9} are achievable [77] with Brewster angle polarisers but losses and complexity to align prevent their use.

The photo elastic modulator The photo elastic modulator (PEM)is the heart of the set-up in charge of the polarisation modulation.

The first polarisation modulation based circular dichroism set-up in the UV/Visible region was developed in 1960 [69]. The modulation between the two left and right circular

---

[5] The extinction ratio of a polariser is a measure of its ability to attenuate a plane polarised beam. Assuming a perfectly plane polarised incident beam, T_1 is defined as the maximum transmission for which the polariser can be oriented. Minimum transmission T_2 is the transmission through the polariser when it is rotated 90 degrees from T_1. The extinction ratio is given as $\dfrac{T_1}{T_2}$

states, was achieved using a an electro-optic modulator made from potassium dihydrogen phosphate (KDP). Transmission range of KDP and the restricted polarisation retardation limits imposed by the high voltage requirements limited this technique to visible and UV regions.

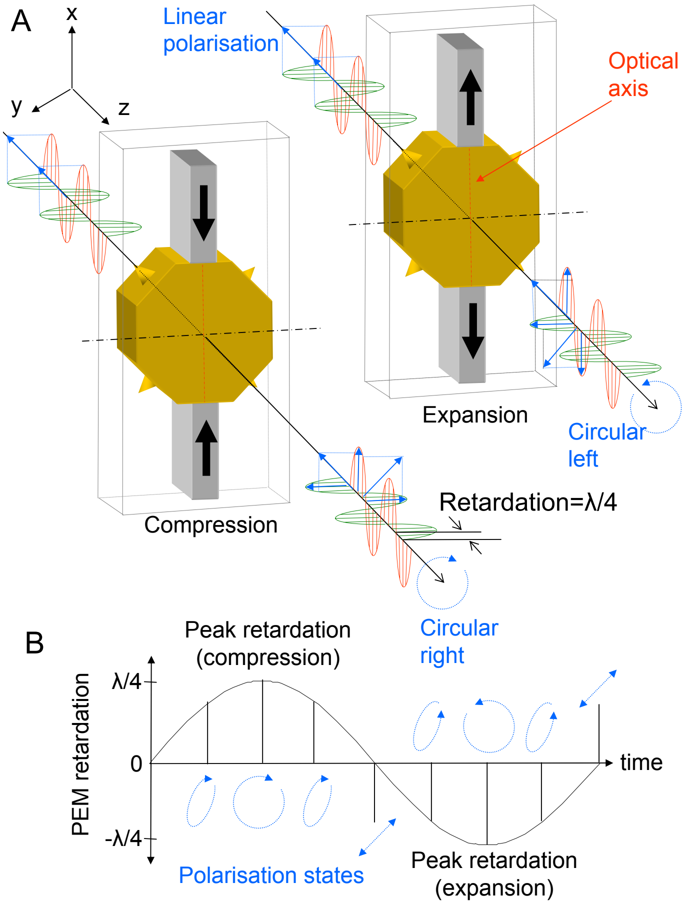

Figure 1.8: A: Functioning of a photo elastic modulator: An octagonal photo elastic crystal is sandwiched between two piezometers. When the bar is compressed, the polarisation component parallel to the modulator axis travel faster than the horizontal component and inversely if the bar is expanded. The phase difference between the two components can be adjusted to produce circular polarisation. See text for details. B: PEM retardation amplitude versus time for a full modulation cycle, polarisation states are indicated in blue arrows. At the peak's retardation (compression and expansion), the incident linear polarisation is rotated by 90 degrees. In between, when the retardation is zero, the PEM is inactive and the incident linear polarisation at 45 degrees remains unchanged.

Things changed with the invention of the photo elastic modulator in the late 1960's by Kemp [30]. The phenomenon of photo-elasticity is the basis for operation of the PEMs, it is the ability of a stressed material to exhibit a birefringence proportional to the applied strain. In its simplest form, a PEM consists of a rectangular bar of suitable transparent material (fused silica, lithium fluoride and calcium fluoride for the visible, ZnSe and silicon for the infrared) sandwiched between two piezoelectric transducers [6]. The bar vibrates along the axis set by the piezoelectric transducers at a resonant frequency determined by the length of the bar and the speed of a longitudinal sound wave in the bulk material. The frequency is usually between 20 kHz and 100 kHz depending on the crystal and its size. The oscillating birefringence effect is the maximum at the center of the bar. The advantages in comparison to a classical KDP electro-optic cell are the large acceptance angle, ±20 ° (2-3 ° for a KDP crystal) [78] and also the possibility to operate in the infared with transparent material like ZnSe. For the use in the infrared, the rectangular shaped bar has been replaced by an octagonal one using a two dimensional standing wave which approximately doubles the retardation available at the center with a given voltage. The effect of the modulator on a linear incident polarisation is shown on Figure 1.8 A and B. The incident plane of polarisation is inclined at 45 degrees to the modulator axis. If the crystal is relaxed, the light passing through the bar remains unchanged (not shown on the Figure). If the crystal is compressed, the polarisation component parallel to the modulator axis travels slightly faster than the horizontal component. If the optical element is expanded, the vertical component lags behind the vertical component (see Figure 1.8 A). The phase difference between the two components at any instant of time is called the retardation. The peak retardation is the amplitude of the sinusoidal retardation as a function of time (see Figure 1.8 B). The retardation is given by

$$A(t) = z(n_x(t) - n_y(t)) \tag{1.46}$$

Where z is the thickness of the optical element and n are the instantaneous values of refractive index along the x and y directions. When the peak retardation exactly reaches one-fourth of the wavelength, the PEM causes a 90-degrees phase shift between the two orthogonal polarisations and acts as a quarter-waveplate. For an entire modulation cycle, Figure 1.8 B shows the retardation versus time and the polarisation states at several points in time. The polarisation oscillates between right- and left-circular for the peak retardation, with linear and elliptical polarisation states in between.

Another important condition occurs when the peak retardation reaches one-half of the wavelength of the incident light. When this happens, the PEM acts as a half-waveplate at the instant of maximal retardation and rotates the plane of polarisation by 90 degrees (see Figure 1.9).

The detection scheme To detect the modulated IR intensity, high sensitivity, cooled solid state detectors with a moderately fast response (due to the modulation frequency) are used. At wavelength inferior to 5 μm, InSb detectors are preferred. For higher wave-

---

[6] Hinds instruments Inc. is the only retailer for PEMs

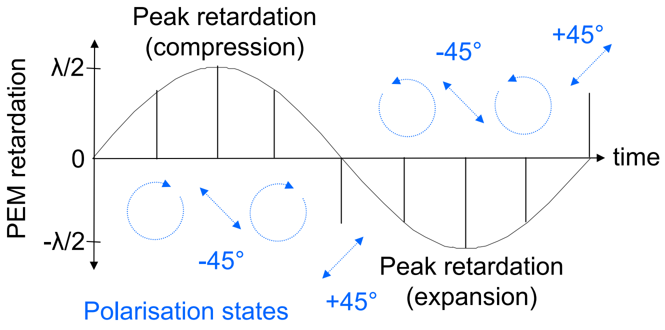

Figure 1.9: PEM retardation amplitude versus time for a full modulation cycle, polarisation states are indicated in blue arrows. At the peak's retardation (compression and expansion), the incident linear polarisation is rotated by 90 degrees. In between, when the retardation is zero, the PEM is inactive and the incident linear polarisation at 45 degrees remains unchanged.

length, photo-resistive HgCdTe detectors (MCT) are commonly used due to their high sensitivity [79]. Detector non-linearity, which is a source of artefacts (see section 5.1.1), can be decreased by switching from photo-resistive to photo-voltaic configuration [80]. In most designs, the signal generated by the detector is first passed through an automatic normalization circuit, which adjusts the amplification of both the average and the differential IR signals to keep the average signal constant. A feed back loop containing a lock-in amplifier is used for the normalization. Since the VCD signal is proportional to the ratio of the differential and average signals, the PEM modulated signal after such a normalization is directly proportional to the VCD intensity. More sophisticated detection schemes including several lock-in amplifiers have also been developed [17, 29].

Chapter 2

Technical description of the vibrational transient chiral set-up

2.1 General layout overview

We present in the next part the experimental set-up which allows us to access vibrational circular dichroism dynamics. The configuration is in many ways close to a classical time-resolved IR spectroscopy set-up. A Ti:sapphire laser system producing 800 nm femtosecond pulses is split into two parts (see Figure 2.1), one part of the beam is sent to an optical parametric amplifier (OPA) to generate the mid-infrared probe pulses while the other part is sent to a non collinear optical parametric amplifier (NOPA) to create the visible pump pulses. Both pulses are then recombined in a pump-probe set-up. In the case of our transient VCD set-up, the main difference lies in the pump-probe set-up where left- and right-circular polarised pulses are generated.

2.2 Generation of the femtosecond 800 nm pulses

The laser system is depicted in Figure 2.2. A titanium-doped aluminum oxide (Ti:Al_2O_3) crystal oscillator (Tsunami - Spectra-Physics), pumped by a frequency doubled Nd:YVO_4 continuous laser (Millenia - Spectra-Physics), generates short (80fs), low intensity (6nJ per pulse), 800 nm pulses at 80 MHz repetition rate.

A pulse coming from the oscillator is then selected by a Pockels cell and enters the regenerative amplifier. It consists of a Ti:sapphire laser cavity pumped by a doubled Nd:YLF (Evolution - Spectra-Physics). To avoid damaging the cavity crystal, pulses are stretched before and re-compressed after amplification. After several travels through the cavity a very intense (800 μJ per pulse), short (100 fs), 800 nm pulse is singled out by the output Pockels cell and sent to the optical parametric amplifier and NOPA for frequency conver-

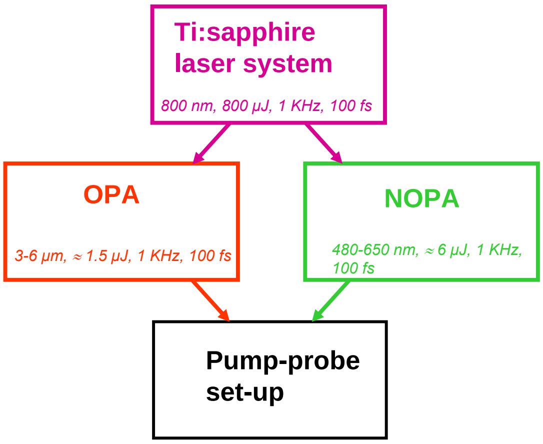

Figure 2.1: Schematic representation of the whole transient set-up. Pulses coming from the Ti:Sapphire laser system are split into two parts: One part generates the mid-IR pulses (OPA), the other one creates the visible pump pulses (OPA), the two are then recombined in the pump-probe set-up.

sion. The repetition rate of the regenerative amplifier is limited by the pulsed Nd:YLF pump laser which works best at around 1 KHz and by the maximum frequency of the Pockells cells.

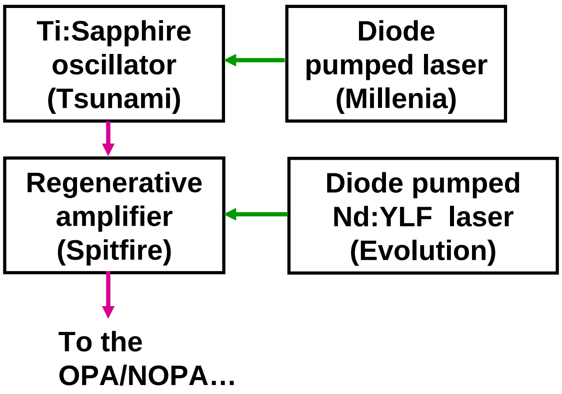

Figure 2.2: Schematic representation of the laser system (see text for details)

2.3 Generation of the mid-IR pulses

A home built two stages optical parametric amplifier (OPA), based on a β-barium borat (BBO) crystal, followed by difference frequency mixing in a AgGaS$_2$ crystal is used to generate intense and stable mid-infrared pulses tunable between 3 and 8 μm [81].

Figure 2.3 is a schematic representation of the OPA: A very small fraction of the

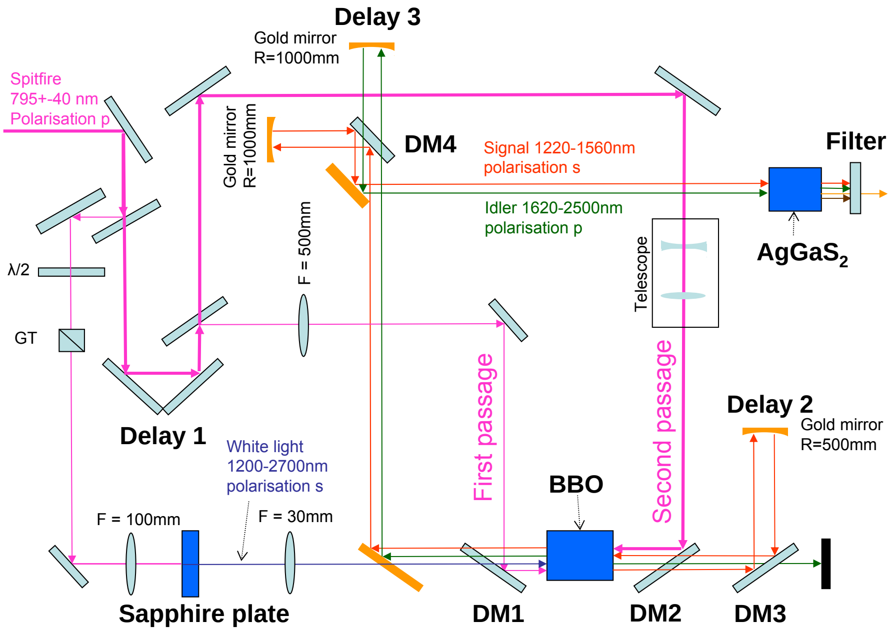

Figure 2.3: Schematic representation of the optical parametric amplifier(OPA). Important parts are highlighted in bold. See text for details.

800 nm beam (1-2 μJ) is used to create a white light continuum in a sapphire plate. This continuum acts as a seed for parametric amplification. Both the white light and another fraction of the 800 nm (15 μJ) are focused in spatial overlap on a type II BBO crystal(ϑ = 27 °, α = 30 °). Temporal overlap of the two beams is ensured by the delay stage 1. The generate idler beam is removed by a dichroic mirror (DM3) while the amplified signal is used as a seed for a second amplification stage using the same BBO crystal and a more intense part of the 800 nm original pulse (200 μJ) as a pump. Resulting signal (1220-1560 nm) and idler (1620-2500 nm) are separated on dichroic mirror, DM4, then spatially and temporally recombined onto a type I AgGaS$_2$ crystal (ϑ = 33 °, ϕ = 45 °). The mid-IR pulses generated by difference frequency generation (DFG) in the AgGaS_2 crystal are then filtered out. Their frequency is tunable between 3 to 8 μm and the energy is typically around 1.5 μJ. The temporal duration is around 100 fs and spectral width 200 cm^{-1}. A saturation mechanism allows an exceptionally low pulse-energy fluctuations of only 0.2% of the mid-IR pulses which is smaller than the Ti:sapphire amplifier noise [81]. This exceptional stability is a requirement to access really small chiral absorption differences.

2.4 Generation of the visible pulses

The generation of the visible pump light is achieved by an home made non collinear optical parametric amplifier (NOPA) [82–84].

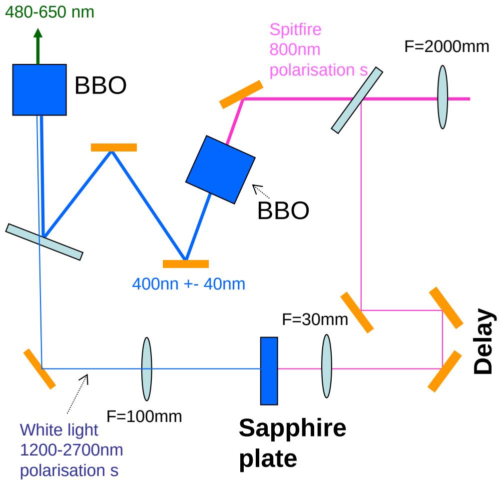

Figure 2.4: Schematic representation of the non collinear optical parametric amplifier (NOPA). Important parts are highlighted in bold (see text for details).

Schematic representation of the NOPA is presented in Figure 2.4: A part of the 800 nm laser pulse coming from the previously described Ti:sapphire laser system, is converted into a 400 nm pulse in a BBO crystal (1 mm, type I, θ=32 °, ϕ=0 °) as another small fraction of the beam is used to generate a white light continuum in a 1 mm thick sapphire plate. Both beams (the 400 nm pump and the with light seed) are then spatially and temporally recombined onto a BBO type I crystal (2 mm, type I, θ=32 °, ϕ=0 °). The pump beam is not collinear with the seed and actually comes underneath so that phase matching condition is achieved by rotating the BBO crystal around its horizontal axis. Tuning the BBO angle and the seed delay allows to generate uncompressed few μJ pulses with center wavelength between 480 and 650 nm.

2.5 The pump-probe set-up

2.5.1 Static measurements

The pump-probe set-up is the heart of our system, it is where we recombined visible pump and IR probe pulses and where we generate the alternating left- and right-circular polarisation. In classical pump-probe experiments, variation of the absorption with time provides information on the dynamics of the excited state of a sample and the formation of photo products. In such an experiment, a pump pulse first excites a sample or initiates a reaction and a probe pulse, which is delayed with respect to the pump pulse, is used to monitor differential absorbance of the sample as a function of the delay time. Following this method, we add in the probe beam pathway a photo elastic modulator which generates alternately the left- and right-circular polarisation, allowing not only to

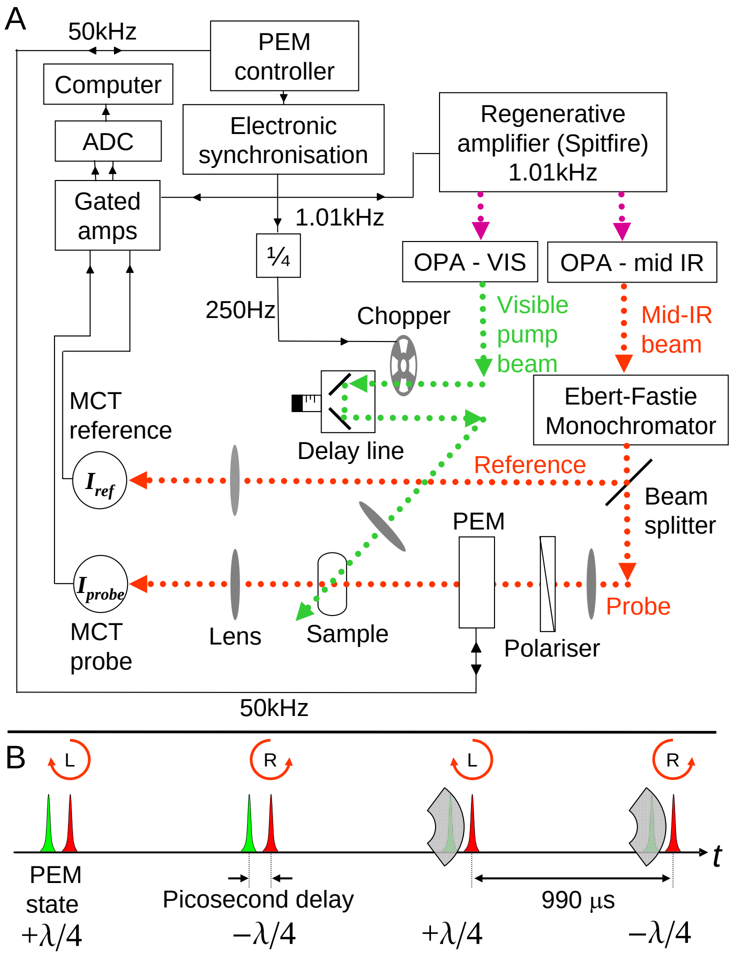

Figure 2.5: A: Schematic representation of the pump-probe set-up (see text for details). B: Timing for transient measurements, four different signals are recorded repeatedly ever four consecutive probe pulses by periodically blocking the pump beam at one quarter of the laser frequency.

measure absorption changes but also circular dichroism changes. Our set-up is inspired by the first implementation by Xie and Simon of picosedond time-resolved electronic circular dichroism spectroscopy [13] and is described in detail in Figure 2.5 part A. Figure 2.6 shows a picture of the set-up. The femtosecond infrared pulses take the place of a black body radiation from ceramic or graphite-based glower (or tungsten in the near-IR) used in conventional VCD spectrometers. Visible pulses are created through a non-collinear optical amplifier.

The mid-IR pulses from the OPA are spectrally narrowed by a home built Ebert-Fastie monochromator (300 gg/mm grating, cylindrical mirror f=127 mm) specially designed not to change the beam profile. Pulse bandwidth and time duration can be varied with slit size (typically 0.25 or 0.5 mm) and we carry out a wavelength scan by rotating the grating. A portion of the IR beam is split off just after the monochromator and focused with a ZnSe lens on a nitrogen cooled single element mercury-cadmium-telluride (MCT) detector (Infrared associates). We use this detector as a reference to correct for intensity fluctuations of the laser.

A wire grid polariser (extinction ratio $\approx 10^{-4}$) and a ZnSe photo elastic modulator (Hinds Instruments, Inc.) are placed in between focusing lens (ZnSe, 12 cm focal length) and the sample to modulate the polarisation between left- and right-circular. The focal spot (100 μm, FWHM)is then imaged onto a second MCT detector by a single ZnSe 10 cm focal lens. As described in more detail later, we synchronize our laser source to the fix PEM natural frequency (50.01 kHz) so that pulses cross the modulator each time it acts as a quarter waveplate with an opposite sign for consecutive pulses. The transmitted intensity is recorded individually for every laser shot using home built gated amplifiers followed by 16 bits analogue/digital conversion. The VCD signal is then evaluated in the computer as the log-ratio of an average (typically 300-1000) of left- and right-handed probe pulse intensities, corrected by the appropriate reference signals

$$A_{vcd} = log_{10}(\frac{\sum I_{probe}^{left}}{\sum I_{ref}}) - log_{10}(\frac{\sum I_{probe}^{right}}{\sum I_{ref}}). \tag{2.1}$$

2.5.2 Transient measurements

For transient VCD measurements, the visible pump beam coming from the NOPA is focused onto the sample in spatial overlap with the IR probe. Four different signals are recorded repeatedly every four consecutive probe pulses by periodically blocking the pump beam at one quarter of the laser frequency (250 Hz)(see Figure 2.5 part B). They correspond to the two states of the PEM ($+\lambda/4 - \lambda/4$) each with and without the pump beam. VCD signals before and after photo excitation are thus measured quasi simultaneously and can be subtracted to produce the transient VCD signal, which is evaluated in the computer as

$$\Delta A_{vcd} = A_{vcd}^{pump\ on} - A_{vcd}^{pump\ off}. \tag{2.2}$$

By increasing its optical path using a motorized translation stage, the pump beam is then delayed with respect to the IR probe beam to record transient VCD signals at different time delays. To ensure a complete exchange of the sample between two laser pulses, we use a home-built flow cell consisting of two CaF_2 windows separated by a 100 μm Teflon spacer [85]. It also allows us to record solvent background spectra under identical experimental conditions.

With this technique, we could record VCD changes of several μOD in the course of a photo-induced reaction on a picosecond time-scale using an open shell transition metal complex with the chiral ligand (-)-sparteine as a test molecule. Those results are presented in Chapter 4. Our laser based set-up also features some advantages over conventional spectrometers based using thermal light sources for recording static VCD spectra. The tightly focused IR laser beam, which we typically attenuate by more than a factor 10, allows for smaller sample volumes and higher spectral resolution. Sample with large solvent background (diluted aqueous systems) are still measurable in thicker sample cells. In addition, using this configuration, important signal enhancement can be achieved by employing crossed polarisers and elliptically polarised light, this technique will be developed in Chapter 5.

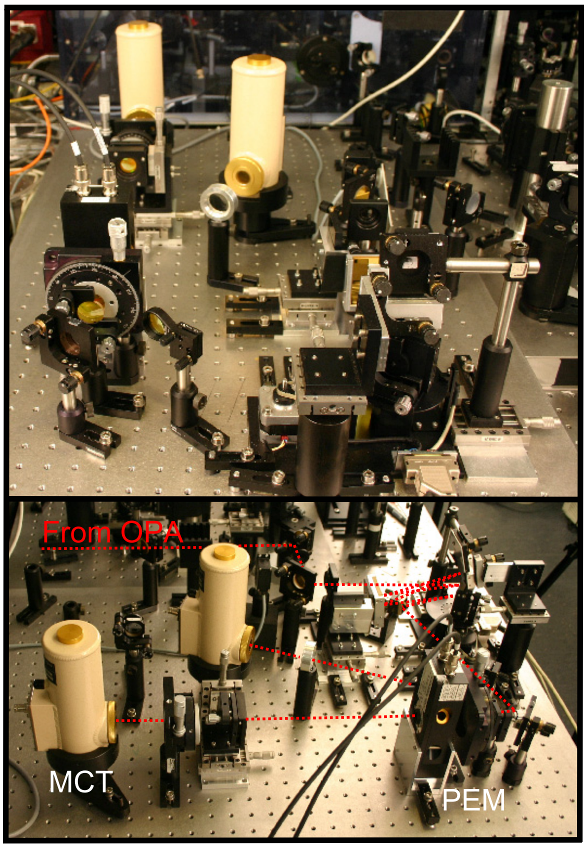

Figure 2.6: The static VCD/VORD set-up. See text for details.

Chapter 3

Polarisation control and artefacts minimisation

3.1 Artefacts in static and transient VCD/VORD spectroscopy

In VCD/VORD spectroscopy, polarisation-based artefacts can be orders of magnitude larger than signals and can easily dominate, their minimization is then crucial. Several articles have been describing in detail possible polarisation artefacts [12, 27, 28, 86], we present in the following those artefacts trying to give as much as possible a pictorial description of each effect. Artefacts coming from the non-linearity of mid-IR detectors and small background signals can also distort the VCD/VORD spectra and need to be considered as well.

3.1.1 Non-linearity of the detectors

Mercury-cadmium-telluride based detectors (MCT) are widely used in infrared spectroscopy because they offer a high sensitivity over a relatively wide frequency range [79]. Two types of configurations are available: Photoconductive (PC) HgCdTe detectors are operated with a constant DC bias to sense the photo generated conductance change which should be proportional to the radiant power incident on the detector. Photovoltaic (PV) HgCdTe detectors generate a photo current which is proportional to the incident photon flux. However, both detectors types exhibit non linear response not proportional to the incident intensity [87–89]. The result is that the chiral signal is significantly reduced in regions of weaker sample absorption and in the center of the laser spectrum and can be strongly distorted. The choice of a detector as linear as possible is then a major issue. Furthermore, not only the detector but the amplifier which is used to condition the output of the signal can introduce non linearities.

In our set-up, we tested both photo-conductive and photovoltaic detection schemes. Liquid nitrogen cooled photo-conductive HgCdTe elements with an active area of 1×10^{-2} cm^2 where bought from Infrared Associates Inc, they were coupled to home built gated amplifiers which outputs were directly linked to the AD conversion card. Liquid nitrogen cooled photovoltaic elements with an active area of 0.25×10^{-2} cm^2 were bought by Kolmar Technologies Inc, they were supplied with an integrated pre-amplifier which output was sent to a gated integrator (SR250 from Standford Research System) and then to the AD conversion card. As previous studies suggested [80], the problem of linearity is improved largely by using the photovoltaic type of detector (see Figure 3.1), the photovoltaic configuration coupled with a smaller size of the active area decreases the time constant of the detector leading to a much better linearity. We nonetheless still apply a linearisation procedure.

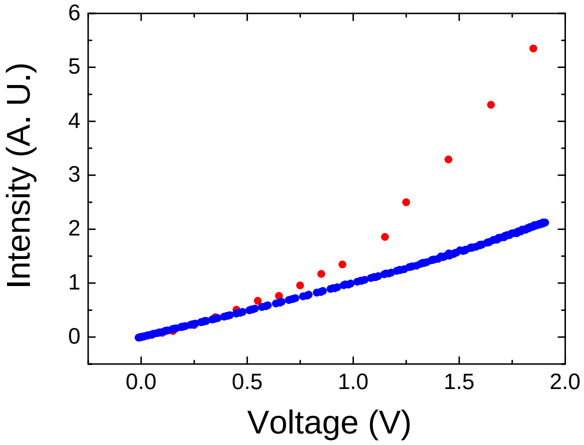

Figure 3.1: Detectors linearity. Laser intensity versus voltage recorded at the output of the MCT detector. Blue circles correspond to photovoltaic configuration PV, red circles to photo-conductive configuration PC. The PV configuration exhibits a better linear response.

Background signals from electronic and diffuse background infrared radiation also create artefact signals, typically with the spectral profile of the transmitted light intensity. Prior to any (transient) VCD/ORD scans, four background signals are recorded (IR-beam blocked) for each detectors, which correspond to and are subtracted from the four signals needed to evaluate the transient VCD or VORD. Their amplitudes are very small and we noticed significantly better offset correction after increasing the resolution of the AD-conversion from 12 to 16 bits. Nevertheless, background drifts remain an important source of noise in the narrow band transient VCD/ORD measurements.

3.1.2 Polarisation-based artefacts

By polarisation-based artefacts, we mean all the unwanted signals which originate from the polarisation of the probe beam and its interaction with the sample.

In chiral spectroscopy, the aim is to measure circular dichroism (CD) and circular birefringence (CB). Circular dichroism is the difference of absorption between left- and right-circular polarised beams (see Figure 3.2 A) as circular birefringence is the difference of refraction between left- and right-circular polarised beams (see Figure 3.2 B) (CB is also known as optical rotation (OR), OR measurements will be presented in Chapter 5). Every circular dichroic sample will exhibit circular birefringence and *vice-versa*, nonetheless, CB does not induce any difference of intensity between left- and right-circular polarised states and thus does not perturb the circular dichroism measurement [12]. Similarly, it can be shown using basic Jones calculation (see Appendix) that CD will not perturb circular birefringence measurements. polarisation-based artefacts susceptible to distort the signal are linear birefringence, (LB) and linear dichroism, (LD) and come from the sample anisotropy [1].

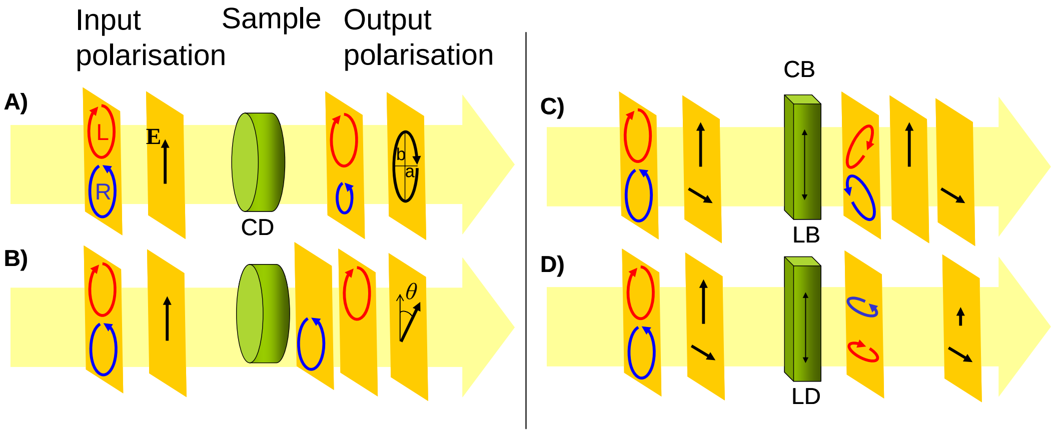

Figure 3.2: Schematic representation of the interaction of polarised light with the medium. A: Circular birefringence (CB), B: Circular dichroism (CB) or optical rotation (OR), C: Linear birefringence (LB), D: Linear dichroism (LD). The effects on the input polarisation are represented for circular polarisation states (red and blue arrows for left- and right-circular polarisation respectively) and for linear polarisation states (black arrows). See text for details.

Linear birefringence In a linear birefringent (LB) medium, linearly polarised light beams parallel and perpendicular to an optical axis travel at different speeds. As it is shown in Figure 3.2 C, the result is that LB converts left- and right-circular polarised beams into two elliptical polarised ones with different axis orientation. An elliptical polarised beam can always be decomposed into the sum of a perfectly circular polarised component plus a linear one. In the case of LB, the linear components added to the right- and left-circular polarisation have different orientation axis (see Figure 3.2 C)

---

[1] We will not consider artefacts coming from depolarising effects as very few optical elements present depolarising properties. Those are not present in our set-up.

Usually, liquid samples are not oriented and their linear birefringence can be neglected but this is not the case for optical elements such as sample cell, lenses, modulator, etc. which exhibit strain birefringence. The effect of LB alone is a reduction of the chiral signals by $\cos \tau L$ [12], where τL is the retardation induced. Fortunately, for most optical elements τL is $\ll 10°$, in this case $\cos \tau L$ is ≤ 0.985 and the reduction in signal resulting from LB is less than 1 %. Further problems arise when the strain induced LB interacts with linear dichroism, this will be discussed later.

Linear dichroism In a linear dichroic (LD) medium, linearly polarised light beams parallel and perpendicular to an optical axis are absorbed to different extend (see Figure 3.2 D). Being orders of magnitude larger than CD and CB, LD can easily dominate the signal. Fortunately, as for linear birefringence, a liquid sample should not exhibit preferential absorption axis unless if the isotropy is broken, which can be the case in transient experiments where the pump is linearly polarised and excites molecules with electronic transition dipoles oriented parallel to the pump pulse polarisation.

Interaction of strain induced LB and pump-induced LD As we saw, every effect taken separately are not a source of concern. Problems mainly arise when we have interaction between the pump-induced linear dichroism and strain induced linear birefringent [12]. The phenomenon is depicted on Figure 3.3 for CD measurement: Effect of strain induced linear birefringence is to create two left- and right-handed ellipses with different orientations of their major axis. Those two ellipses can be decomposed in a circular and linear part. The linear part will probe the linear dichroism of the sample those anisotropy has been broken by the pump beam. At the end the detector records the sum of two signals: LD and CD, LD being orders of magnitude larger than CD. Similar considerations apply to CB measurements. The linear birefringence has different sources, it can arise from strained optics (lenses) but in our case also from an imperfect photo elastic modulator. It is easy to show that if the polarisations of the left- and right-handed beams can be described by the same ellipses i.e. when they are composed of a circular component of opposite handedness plus the same linear component, the LD signal is cancelled when computing the circular dichroism signal.

In summary, LD and LB are not strong concerns when they are considered separately. Nevertheless, important artefacts can appear when non-perfectly circular or symmetrically elliptical polarised probe beams interact with a sample in which excitation by a polarised pump beam has broken the sample isotropy. Imperfect polarisation of the probe beam can arise from strain linear birefringence of the cell windows or from the modulator itself.

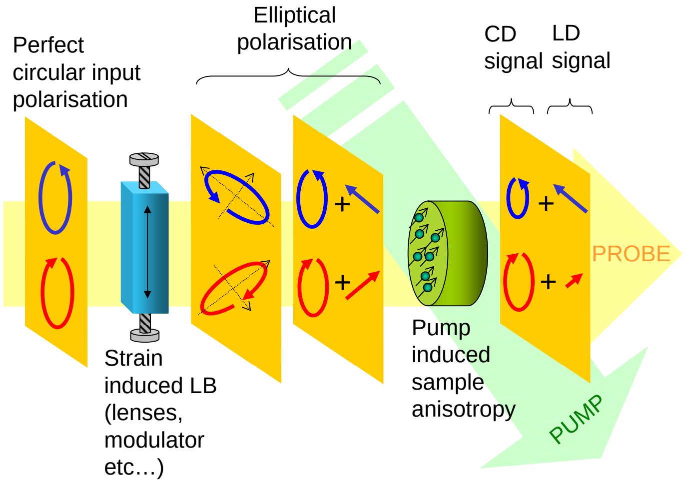

Figure 3.3: Schematic illustration of the effect of a linear birefringent medium (LB) on incident left- and right-circular polarised light. Two elliptical polarisation states are produced with different orientations of their main axes. They can be described as perfectly symmetric circular states plus linear polarisations with different orientations. These linear polarisation components can probe pump-induced anisotropy of the sample leading on the detector the sum of two signals: Circular dichroism and linear dichroism, the latter being one order of magnitude larger.

3.2 Artefacts control and polarisation optimisation

3.2.1 Review of the solutions already proposed in the literature

Different techniques have been suggested in the literature to suppress or at least to diminish such artefacts, mainly in the context of electronic static/transient CD spectroscopy. One possible solution is to try to depolarise the pump laser beam by inserting a spinning half-waveplate into the pump path [13]. Hache and co-workers, on the other hand, proposed to carefully align a Pockels cell to optimize circular polarised probe pulses in the UV/visible [28]. They were able to obtain a sufficiently high degree of circular polarisation to reduce birefringence artefacts below the noise level. In the mid-infrared regime Pockels cells cannot produce the necessary birefringence and photo elastic modulators (PEM) are preferably utilized for manipulating the polarisation state. They are usually employed for the polarisation modulation of a continuous light beam in static vibrational circular dichroism measurements, where the birefringence of optical elements in the beam path can cause similar artefacts as anisotropic excitation in pump-probe measurements. In order to reduce such artefacts, Nafie and co-workers proposed to use a second photo elastic modulator placed immediately after the sample to scramble the polarisation [90]. This second modulator has a different frequency from the first one and its retardation is adjusted so as to randomize the polarisation of the infrared beam. By averaging over a large number of modulator oscillations, polarisation-based artefact signals can be strongly reduced. Similarly, a beam reversal configuration has been proposed, where the probe beam is reflected back through the same PEM prior to detection, to return the light to its original state of linear polarisation [86]. While these methods can greatly improve the quality of static VCD measurements, artefacts arising from imperfections of the sample cell (e.g. strain-induced linear birefringence of the windows or linear birefringence of an anisotropic sample) cannot be removed in this manner. To achieve this, it was recently proposed to insert an additional rotating half-waveplate into the beam path [91]. Methods based on time-averaging over random pump or probe polarisations in order to eliminate artefacts appear at present too time-costly to be applied to transient VCD measurements. Indeed, with lasers of kilohertz repetition rate highest sensitivity is achieved by comparing, under identical conditions, the transmitted intensity of consecutive mid-IR laser pulses in the presence of and without the preceding pump pulse that induces the chemical or biochemical reaction of interest. Our approach to reducing artefacts in transient VCD spectroscopy is similar to that of Hache and co-workers [28] and we present in the following a method that allows us to create highly symmetrical probe beam polarisations using a photo elastic modulator. Intrinsic imperfections of the modulator and strain birefringence of the sample cell, can be largely compensated by an appropriate timing scheme.

3.2.2 Symmetric triggering

The photo elastic modulator consists of an octagonal ZnSe bar attached to two piezoelectric transducers. The bar vibrates at a fixed natural frequency f_m of approximately 50 kHz, determined by its length and the speed of sound in the material so that we need to electronically synchronize the laser system to the PEM.

The synchronisation electronic is explained in Figure 3.4 A: By doubling the PEM modulation frequency f_m, a $2f$ signal (100 kHz) is generated and down-counted to 1.01 kHz by an odd number of cycles (division by 99 [2]) . This 1.01 kHz signal (f_t) is then appropriately delayed (delay d) and triggers the pump laser and the Pockels cells of the femtosecond amplifier. Approximately every millisecond the Pockels cells single out one weak pulse arriving from the 80 MHz femtosecond oscillator for amplification. This is schematically shown in Figure 3.4 B. The amplified pulses are then converted to the mid-IR and the delay d is adjusted such that they arrive at the modulator when it is alternately in a state of maximum expansion or compression. As illustrated by the plot of the PEM-induced retardation φ as a function of time at the bottom of Figure 3.4 B, the modulator is then acting as a quarter waveplate with opposite sign for consecutive mid-IR pulses.

In order to analyse and optimize the polarisation state of the probe pulses we place

---

[2] Division by an even number would synchronize the laser in such a way that all pulses experience the same retardation when they cross the PEM.

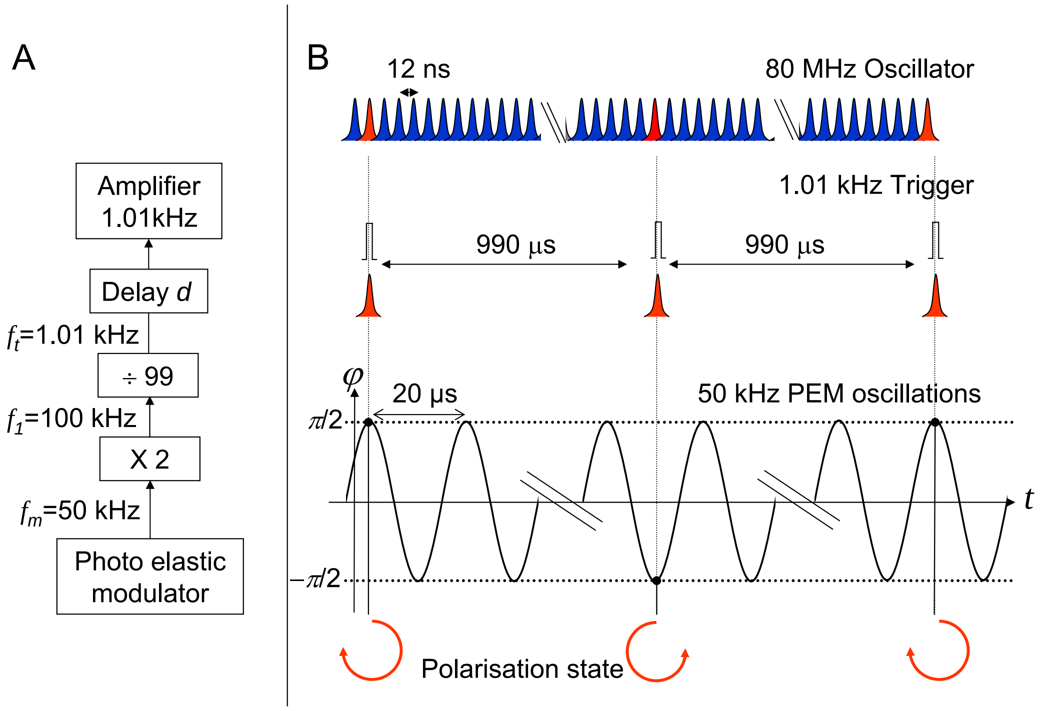

Figure 3.4: A: Synchronization of the laser system to the PEM natural frequency f_m. A 100 kHz signal ($2f_m$) is down-counted to 1.01 kHz by an odd number of cycles (division by 99); this 1.01 kHz trigger is then appropriately delayed before being sent to the regenerative amplifier. B: At the arrival of a trigger pulse at the amplifier, a femtosecond laser pulse from the 80 MHz oscillator is selected, amplified and converted to the mid-IR. We adjust the trigger delay d so that the laser pulses cross the modulator at the turning points of its oscillation, where it acts as a quarter waveplate. This produces a train of circular polarised pulses of alternating handedness, indicated by the circular red arrows.

a second polariser, which is perpendicular to the first one, after the PEM, as depicted in Figure 3.5 A. For a sinusoidal variation of the PEM birefringence φ with time the intensity of the transmitted light is then given by

$$I(t) = I_0\{\sin\varphi\}^2 = I_0\{\sin\varphi_0 \sin\{2\pi f_m t\}\}^2. \tag{3.1}$$

where I_0 is the incident intensity, φ_0 the retardation at the turning points of the PEM oscillations and f_m the natural frequency of the PEM.

To calibrate the maximum retardation φ_0 we first coarsely adjust the trigger delay d such that pulses cross the PEM at a turning point of its oscillations. Then, we vary the modulation amplitude and record the transmitted intensity on the detector, yielding the signal shown in Figure 3.5 B. The maximum signal corresponds to the retardation where the modulator acts as a half-waveplate ($\varphi_0 = \pi/2$), at half of this modulation amplitude the PEM acts as a quarter waveplate ($\varphi_0 = \pi/4$). Subsequently, with the maximum retar-

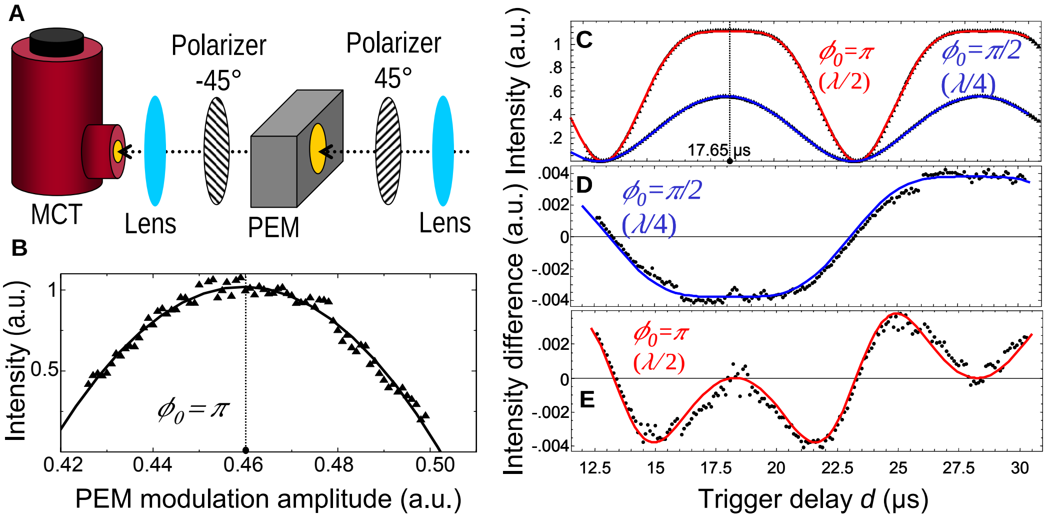

Figure 3.5: Calibration of the PEM retardation and trigger delay using the set-up shown in part A: The PEM is sandwiched between two crossed polarisers and the intensity of the transmitted mid-IR pulses is recorded. B: Intensity recorded as a function of PEM retardation, varied by changing its driving voltage. The trigger delay is set for pulses to cross the modulator at the turning points of the PEM oscillations (d=17.65 μs in part C). The maximum of the curve corresponds to the point where the PEM acts as a half-waveplate, at half of this modulation amplitude it acts as a quarter-waveplate. C: Intensity as a function of the arrival time (trigger delay d) of the mid-IR pulses at the PEM for maximum retardations fixed at $\varphi_0 = \pi/2$ (red) and $\varphi_0 = \pi/4$ (blue). The data (symbols) have been scaled by a cubic polynomial function to correct for the non-linearity of the detector in order to match the signal predicted by Equation 3.1 (solid lines). D: Difference, as a function of trigger delay d, between the intensities recorded for consecutive pulses, which correspond to polarisation states of opposite handedness; maximum PEM retardation fixed at $\varphi_0 = \pi/4$. The difference is due to static birefringence and can be reproduced using Equation 3.2 with $\delta\varphi \approx 0.002$ (blue solid line, see text). E: Same as D but with the PEM retardation fixed at $\varphi_0 = \pi/2$.

dation fixed at $\pi/2$ or $\pi/4$, the arrival time of the pulses at the modulator is varied by delaying the triggers to the laser system, yielding the dotted curves in Figure 3.5 C, which should be described by Equation 3.1. However, in order to achieve the best fit between the recorded signals and the prediction of Equation 3.1 (solid lines in Figure 3.5 C) the measured intensities have to be scaled by a cubic linearisation function to correct for the detector non-linearity. The consistency of this detector linearisation procedure was verified by repeating the measurements at different laser intensities I_0.

Due to the symmetry of the triggering scheme, the mid-IR pulses pass the modulator alternately in a state of compression or expansion of equal magnitude, which ideally produces identical circular or elliptically polarised pulses of opposite handedness. However, we recorded a small yet noticeable difference between the intensities of consecutive pulses after the second polariser. This difference as a function of trigger delay is shown in Figure 3.5 D and E for maximum modulator retardations $\varphi_0 = \pi/4$ and $\varphi_0 = \pi/2$, respectively. The maximum value of this difference does not depend on the retardation amplitude, which excludes an anharmonic oscillation of the modulator. We can model this data by adding a constant $\delta\varphi$ in Equation 3.1

$$I^{'}(t) = I_0\{\sin\varphi_0 \sin\{2\pi f_m t\} - \delta\varphi\}^2. \tag{3.2}$$

It describes a residual static linear birefringence in the direction of the PEM's optical axis (in our case 45 ° with respect to the orientation of the linear polarisers) that is homogeneously distributed along the ZnSe bar. This residual static birefringence is a known effect of photo elastic modulators [92] and leads to a small constant offset of the modulation amplitude. The solid lines in Figure 3.5 D and E are given by

$$I^{'}(t) - I^{'}(t + 1/2f_m) \tag{3.3}$$

with $\varphi_0 = \pi/4$ and $\pi/2$, respectively. The experimental data is reproduced by adjusting the parameter $\delta\varphi \approx 0.002$, from which the tiny ellipticity of the probe pulses can be estimated.

3.2.3 Asymmetric triggering and birefringence compensation

In order to correct for the on-axis linear birefringence of the modulator (or that of the sample cell), we can modify our triggering scheme and slightly adjust the delays sent to the laser system. The principle of this technique is explained in Figure 3.6: The residual static birefringence corresponds to a constant offset $\delta\varphi$ in the retardation modulation, as depicted at the bottom of Figure 3.6 B. When the modulator amplitude is adjusted to produce a maximum retardation of $+\pi/4$ the subsequent laser pulse, in the symmetric triggering scheme, is subject to a retardation slightly in excess of -$\pi/4$ resulting in elliptical polarisation (indicated by the dotted elliptical arrow). A retardation of -$\pi/4$ can nevertheless be realized by making the laser pulse pass the modulator before it has reached the negative turning point of its oscillation. For this purpose, every second trigger is anticipated by a time δt of the order of 100 nanoseconds.

Figure 3.6 A shows schematically, how this asymmetric trigger is generated. We now directly down-count the modulator frequency (f_m = 50 kHz) by an odd number of cycles to trigger a delay generator (Stanford Research) at a frequency f_2 = 505 Hz. Two 505 Hz trigger signals, one delayed regarding to the other by $1/(2f_2)$-δt, ($1/(2f_2) \approx 990$ μs) are then added to produce an asymmetric trigger with a frequency close to 1.01 kHz. Subsequently δt is varied in nanosecond steps until the intensity difference between consecutive

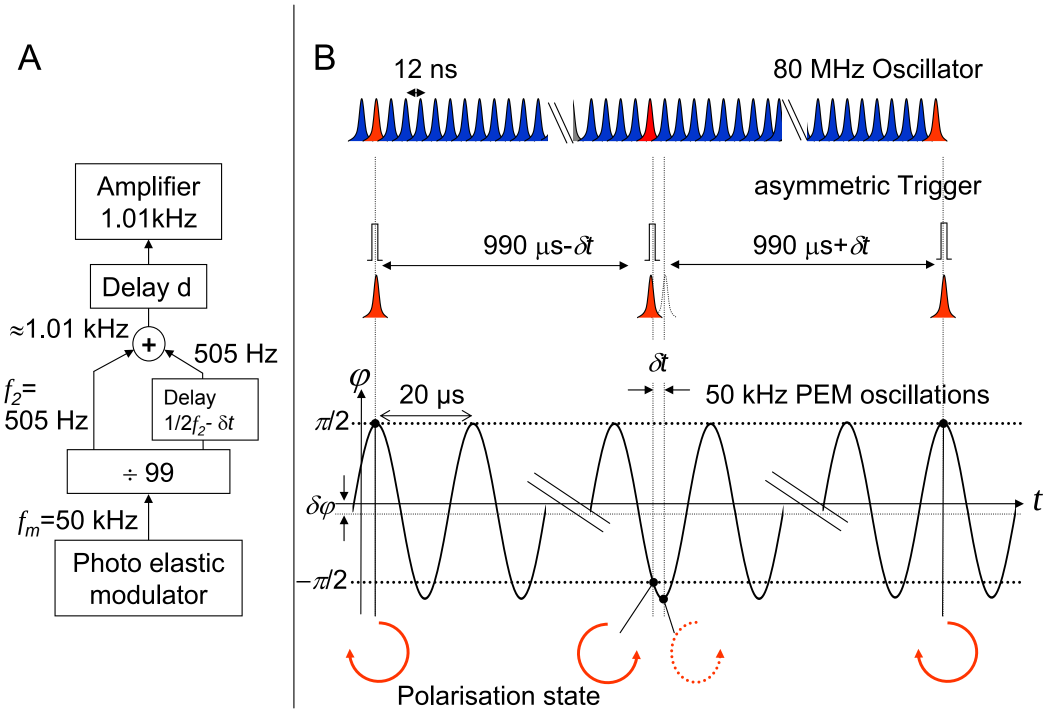

Figure 3.6: A: Asymmetric trigger generation for LB compensation. The PEM frequency f_m is down-counted by an odd number of cycles (division by 99) to produce two f_2=505 Hz signals. One is delayed by approximately half a period before the two are added to form an asymmetric trigger signal of $\approx$ 1.01 kHz for the laser amplifier with the time structure shown in B. B: Static residual birefringence causes an offset $\delta\varphi$ in the retardation modulation. At one turning point the PEM oscillations it is thus slightly in excess of -$\pi/4$, leading to elliptical polarisation (dotted red arrow). This is compensated by appropriately anticipating every second trigger by δt, which selects a pulse for amplification that arrives at the PEM when the total retardation is exactly -$\pi/4$.

pulses (left- and right-handed) detected behind the second crossed polariser vanishes. At the moment, the delay precision is limited by a 12 ns jitter due to arbitrary arrival time of pulses from the femtosecond oscillator. This could, however, be improved by locking the femtosecond oscillator cavity length to the PEM natural frequency using feedback-control [93].

For a final characterization of the polarisation states with optimized modulator amplitudes and trigger delays we measured the light intensity transmitted by the second polariser as a function of its orientation. The data shown in Figure 3.7 A were recorded both with (open circles) and without (solid squares) linear birefringence compensation by asymmetric triggering. It is evident, that the differences between left-handed (red) and right-handed (blue) pulses is significantly reduced by LB compensation. This is seen quantitatively in Figure 3.7 B where the log-ratios of left- and right-handed signals in A are

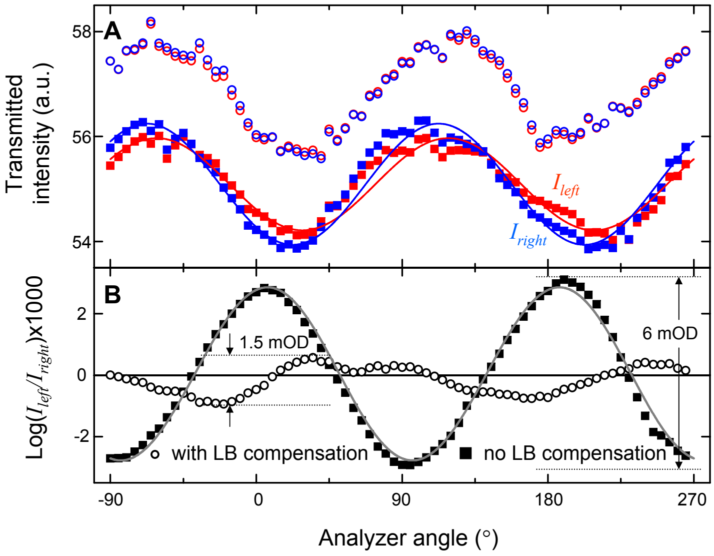

Figure 3.7: Analysis of the probe pulse polarisations after delay and retardation optimization (same set-up as Figure 3.5). A: Intensity of left- (red) and right-handed (blue) pulses as a function of analyser angle. Solid squares: Symmetric triggering scheme (Figure 3.4), Open Circles: After compensation of static birefringence by asymmetric triggering (Figure 3.6). Compensated curves have been offset for clarity. B: Logarithm of the ratio of the signals in A with corresponding symbols. A fit of the data recorded without LB compensation (solid lines in A and B) reveals a static linear birefringence of approximately $\lambda/600$ oriented at 9 degrees with respect to the PEM modulation axis. The off axis component of this birefringence cannot be compensated by asymmetric triggering, leading to a residual difference between left- and right-handed polarisation states (open symbols in B). Slight distortions and the dissymmetry of the data with respect to 180 degree rotation are due to the uneven surface of the polarisers, which consist of a free-standing wire grid without substrate.

plotted. This log-ratio can be viewed as a CD signal recorded with the second polariser in place and is greatly reduced from 6 mOD to approximately 1.5 mOD peak to peak difference thanks to the asymmetric triggering scheme.

The remaining intensity differences between left- and right-handed pulses can be accounted for by an off-axis component of the static birefringence (e.g. caused by strain in a direction different from that induced by the piezoelectric transducers), which is not described by Equation 3.2 and cannot be fully compensated by varying the effective PEM modulation amplitude. The magnitude and orientation of the modulator static birefringence can be determined from a Jones matrix analysis (see section 1), of the data recorded without LB correction in Figure 3.7 , which yields the solid lines in Figure 3.7 A and B. It shows that the modulator static birefringence is equivalent to a waveplate with an optical axis deviating by 9 degrees from the modulation axis and a retardation of approximately $\lambda/600$. The relatively large modulation of the signals in Figure 3.7 A as a function of analyser angle is, however, not primarily due to the static birefringence as it is still observed after compensation (open circles). It is rather caused by a modulation amplitude approximately 1% in excess of $\pi/4$ and a slight misalignment of the modulator orientation with respect to the first linear polariser, deviating by ≈ 0.4 degrees from 45 ° (parameters deduced from the solid line fits in Figure 3.7 A and B). Presently, the latter imperfections are difficult to avoid in our set-up. However, it is clear from the data recorded with LB correction (open circles in Figure 3.7) that they do not prevent the generation of probe pulses with highly symmetrical left- and right-handed elliptical polarisations with almost perfectly parallel major axes. This is sufficient to minimize linear dichroism artefacts in transient CD scans. Furthermore, in static CD measurements with slightly elliptical polarisation the signal is reduced by a few percent at most. We will also show below that even the less perfectly polarised probe pulse generated by our symmetric triggering scheme cause only negligible birefringence artefacts under the conditions of our first transient CD experiment. Nonetheless, in samples exhibiting larger linear dichroism and weaker CD changes much more harmful artefacts may arise unless the static linear birefringence of PEM and sample cell is compensated.

3.3 Conclusion

We have provided a detailed description of a set-up allowing us to generate perfectly symmetrical polarisation. A flexible triggering scheme allows us to precisely control the arrival time of the probe pulses at the modulator to the instant when the total birefringence of modulator and sample cell together corresponds most closely to quarter wave modulation of opposite sign for consecutive laser pulses. The optimization procedure is based on a comparison of the intensities of left- and right-handed polarised pulses that is transmitted by a linear polariser. Although not perfectly circular, the probe beam polarisations are highly symmetric, which makes the set-up insensitive to pump-induced linear dichroism. In particular we have demonstrated that the offset signals due to linear birefringence recorded after placing a second crossed polariser into the beam path, between sample and detector, can be eliminated. This will be important for the signal enhancement and multichannel detection scheme developed in Chapter 5.

Chapter 4

The test molecule

4.1 Resonance enhanced VCD of transition metal complexes

In order to test the ability of our set-up to record VCD transients, molecules which large signals are highly desirable. VCD signals are small signals which only account to 10^{-3} to 10^{-5} of the underlying absorption. Transient VCD are then expected to be very small signals.

It was observed few years after the discovery of VCD that some transition metal complexes exhibit different VCD signals depending on the transition metal, although IR intensities remaining the same [23]. The effect is approximately one order of magnitude and can also be associated with sign changes for some transitions. This enhancement effect has been recently attributed to the presence of underlying electronic CD in the infrared or near infrared (NIR) region [24, 25] and named therefore resonance-enhanced VCD. Usually, electronic transitions take place in molecules at much higher energies than vibrational transitions. However, with some transition metal *d*-orbitals, there can be low-lying electronic transitions. Such low lying $d-d$ transitions could couple with vibrational transition and enhance the anisotropy ratio [25].

For our study, different transition metals are attached to the bidentate chiral alkaloid ligand (-)sparteine (sp) to form a tetrahedral, N-bonded four coordinate chloride complexes of the type M(sp)Cl_2 where M= Co, Ni (see inset in Figure 4.1). Synthesis was done in house following published procedures [26]. Different metal substitution does not alter the tetrahedral configuration [94].

4.2 Transient VCD signals

The spectra shown on Figure 4.1 bottom compare well with published data [24] and demonstrate that signal to noise ratios comparable to commercial spectrometers can be achieved (1 hour averaging for spectra shown in Figure 4.1, baseline rms noise for pure solvent 8 μOD).

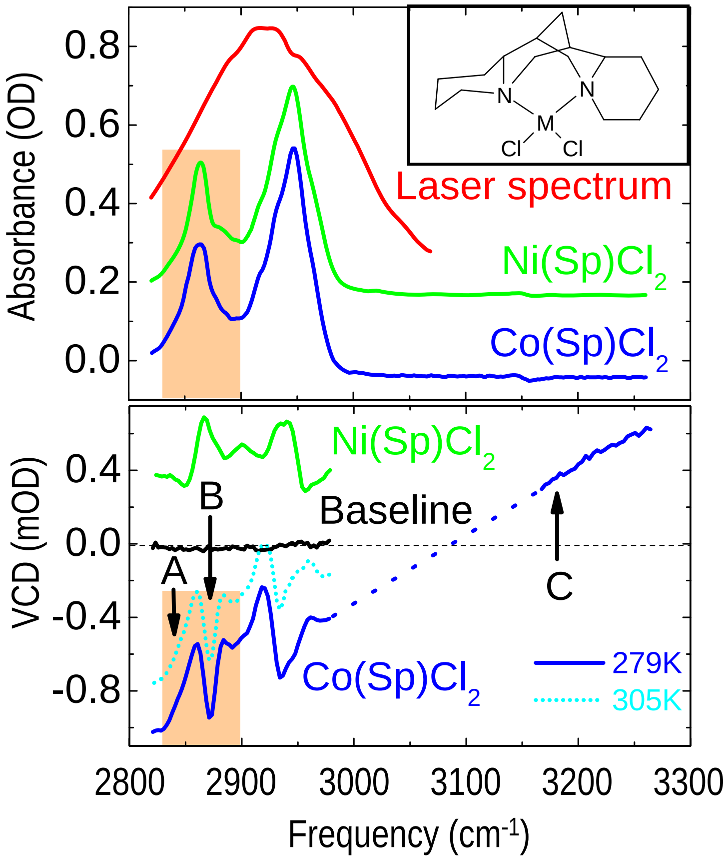

Figure 4.1: Inset: The metal (-)-sparteine chlorine complex M(sp)Cl_2, M stands for transition metal Co, Zn. Top: Structure and absorption spectra of Co(sp)Cl_2 and Ni(sp)Cl_2 in the C-H stretch region of the sparteine ligand (concentration 0.3mol/l). Bottom: Static VCD spectra recorded with the laser set-up (common baseline). The Ni(sp)Cl_2 signal is positive; VCD of Co(sp)Cl_2 is negative and decreasing at higher temperatures

As explained in the previous paragraph, the relatively large ground-state VCD signals of the Co and Ni complexes has been attributed to the closeness of vibrational transitions and low-lying magnetic dipole allowed $d-d$ excitations of the transition metal [24] which give rise to the underlying broad CD signal of Co(sp)Cl_2 in Figure 4.1. Despite almost identical absorption spectra in the C-H stretch region (see Figure 4.1 top), the VCD spectra of Co(sp)Cl_2 and Ni(sp)Cl_2 are of opposite sign and of very different shape, revealing a strong influence of the electronic resonance and thus the d-electron configuration on the VCD signal of the spartein ligand. One may thus expect a change in the chiral signal when the low-lying electronic transitions are shifted after excitation of an electronic dipole-allowed $d-d$ transition in the visible.

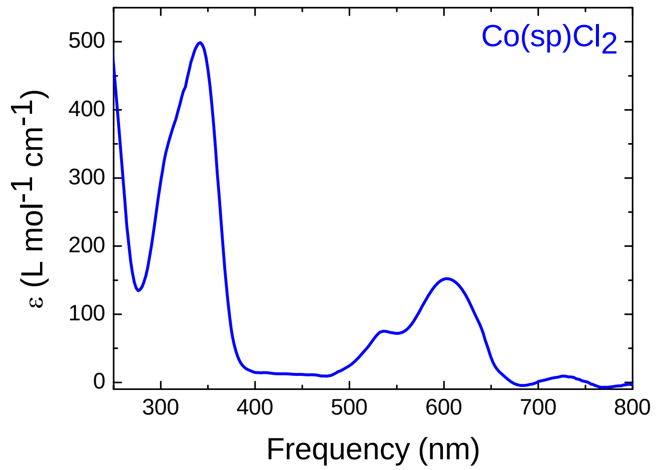

Figure 4.2: Electronic absorption spectrum of the Co(sp)Cl_2 complex. Absorption bands between 450 and 800 nm are coming from ${}^4A_2 \rightarrow {}^4T_1$ transitions. Intense absorption band at a lower frequency correspond to a charge transfer from the metal to the chlorine ligand.

Excitation of a ${}^4A_2 \rightarrow {}^4T_1$ transitions of the cobalt complex (see Figure 4.2) at around 600 nm (2 μJ uncompressed ≈ 100 fs pulses from the NOPA) causes an immediate red shift of the C-H stretch band (see 10 ps spectrum in Figure 4.3), leading to a negative transient absorption signal around 2872 cm^{-1} and a positive one near 2842 cm^{-1}.

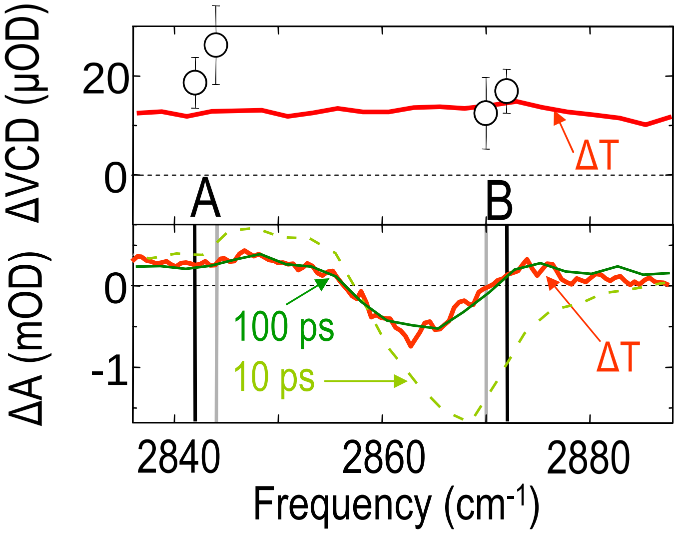

Figure 4.3: Solid red lines, temperature-induced change in absorption (bottom) and static VCD (top) both scaled to a 0.6 K temperature rise to match the pump-probe spectrum at 100 ps delay (solid green line, bottom). A pump-probe after 10ps (dashed green line, bottom) is also shown. Open symbol represent the transient VCD signal shon in fig. a) and b)

This red shift subsequently decreases owing to electronic relaxation and energy dissipation into the solvent ($CDCl_3$) on a 25 ps timescale. The transient VCD signal, on the other hand, diminishes (become less negative) at both probe frequencies as a result of excitation (see Figure 4.4 B and C).

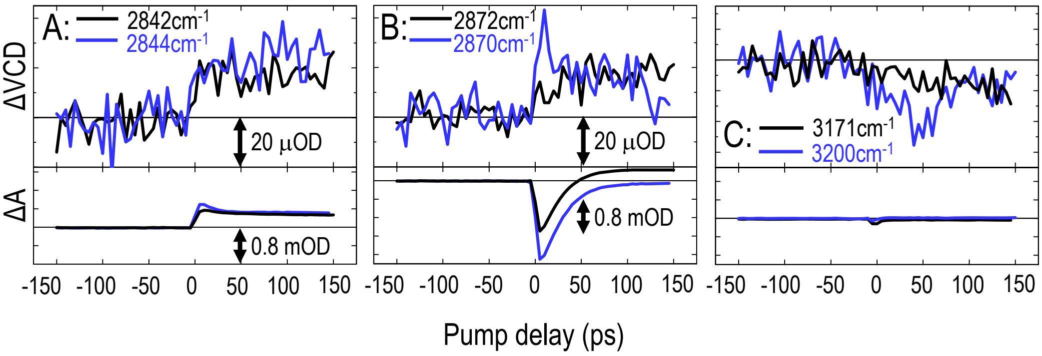

Figure 4.4: Transient absorption signals (bottom) and transient VCD signals (top) at different probe frequencies A, B and C (90 mn integration, 70000 pulses/points). Data plotted in blue and black were recorded several weeks apart. Transient measurement of Ni complex was not possible, because the compound was unstable under visible irradiation.

We noticed a strong temperature dependence of the static absorption and VCD spectrum of $Co(sp)Cl_2$ (see Figure 4.1, bottom) and found that both the transient absorption and VCD signals (at long pump-probe delays) agree with the spectral changes induced by an increase in sample temperature by 0.6 K (see fig.4.3). Such a temperature jump is consistent with the absorbed laser energy, spot size and heat capacity of $CDCL_3$ and appears to be dominating the pump-induced VCD changes, while $d-d$ excitations seem to be too short lived to contribute to the signal at our current time resolution. The different character of transient absorption and transient VCD is also apparent at probe frequencies ≥ 3150 cm^{-1}, where there are no vibrational transitions (and no pump-probe signal) but a large positive (electronic) CD band (see Figure 4.1). At 3171 cm^{-1} the CD signal becomes slightly less positive after visible excitation, indicating an overall pump-induced decrease in the chiral signal (see Figure 4.4 C). However, since the static CD increased slightly with temperature at this frequency, this transient is not yet fully understood.

4.3 Simulations

We investigate the VCD dynamic of the transition metal complex $Co(sp)Cl_2$ with the chiral ligand (-)-sparteine in the CH-stretch region (see the absorption spectrum in Figure 4.5 A). The absorption changes observed at different pump-probe delays after visible excitation of a $d-d$ electronic transition are shown in Figure 4.5 B . As mentioned in the last paragraph, they are consistent with a decay of the electronic excitation on a timescale shorter than the picosecond time resolution of our set-up, causing a strong heating of the molecule, which broadens the C-H stretch vibrations and shifts them to lower energy. This leads to the characteristic derivative-like transient absorption spectrum after 10 ps shown by the red line in Figure 4.5 B. The spectral broadening and shift then partially decays on a 20 ps timescale due to energy dissipation from the hot molecule to the solvent (black and blue line in Figure 4.5 B). These spectral changes are reasonably well-captured by a simulation (see Figure 4.5 C and D) assuming a single Lorentzian band, which is red-shifted and broadened immediately after excitation and then narrows and shifts back with a 20 ps time constant. The static VCD spectrum (Figure 4.5 E) is more difficult to simulate as multiple vibrational modes seem to contribute and vibrational circular dichroism is strongly enhanced by a broad low-lying magnetic dipole allowed *d-d* transition of Cobalt, which is not seen in the absorption spectrum but gives rise to a negative background CD signal [24]. Here we only seek a qualitative match and model the data by assigning an appropriate rotational strength to the narrow Lorentzian vibrational line on top of a broad Gaussian CD band (Figure 4.5 F). After photo-excitation the Lorentzian contribution is assumed to evolve in parallel with the absorption spectrum (spectral shifts and broadening but no change in rotational strength) while the broad background signal strongly weakens in the hot sample after photo-excitation. This is in agreement with temperature-dependent equilibrium measurements (see section 3) which reveal a significant weakening of the static VCD signal in a heated sample. Figure 4.5 G shows the transient VCD changes due to 600 nm excitation recorded at a probe wavelength of 2872 cm^{-1} (indicated by the vertical lines in the Figs. 4.5 A-F). Within signal to noise the VCD signal is a step function, in contrast to the transient absorption changes at the same wavelength. The persistence of the signal to long time delays is attributed to the large number of molecules, which are not directly excited but respond to the heating of the probed sample volume by approximately 2 K after energy dissipation to the solvent. Simulated transient VCD signals at the same probe wavelength are shown in Figure 4.5 H. For these simulations we describe the sample and all optical elements by Jones matrices (see Appendix) and we assume for simplicity that the linear birefringence of modulator and cell windows can be treated as a single birefringent element between modulator and sample, whose strength and orientation are chosen to be consistent with the polarisation analysis presented in the previous section (solid lines in Figure 3.7). Excitation with linearly polarised light, spectral dynamics and rotational diffusion, which takes place with a 50 ps time constant, are taken into account. In order to produce a maximum linear dichroism artefact, electronic and vibrational transition dipole moments are assumed to be collinear, although no significant linear anisotropy was found in polarisation-dependent pump-probe measurements.

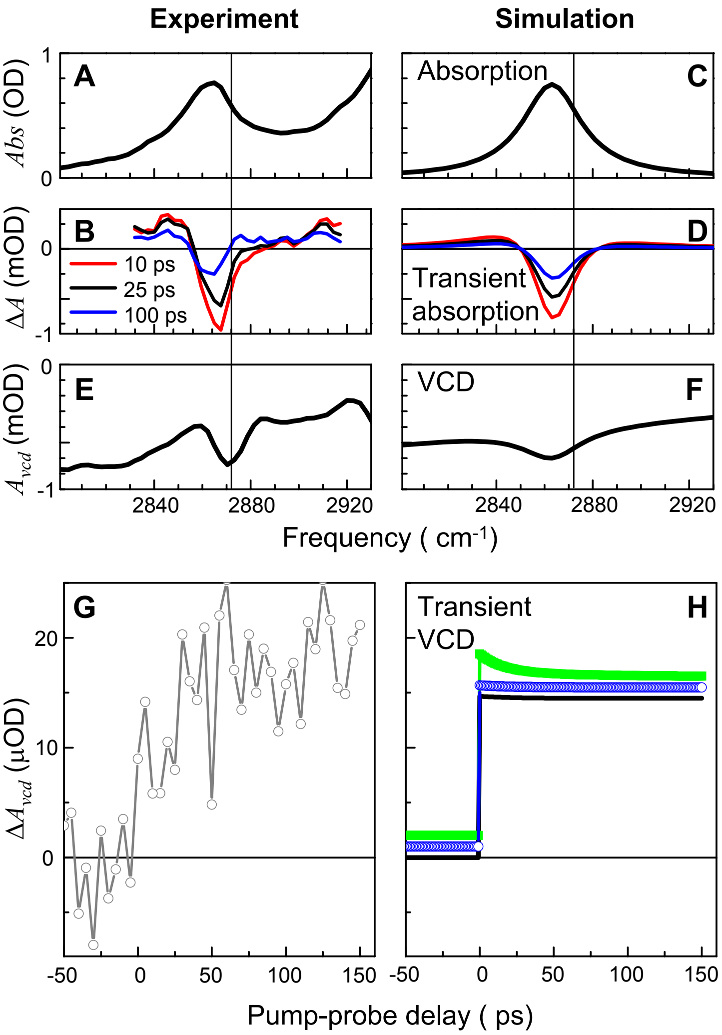

Figure 4.5: A: Absorption spectrum in the C-H stretch region of the Cobalt (-)-sparteine complex Co(sp)Cl_2. B: Transient absorption changes of Co(sp)Cl_2 after excitation of a *d*-*d* ($^4A_2 -^4 T_1$) transition at 600 nm at different pump-probe delays. C: Lorentzian absorption line used in the simulations D: Transient absorption spectra modelled by a shift and broadening of the Lorentzian band which decay with a 20 ps time constant. E: Static VCD spectrum of Co(sp)Cl_2. F: Modelled VCD spectrum assuming a negative rotational strength of the Lorentzian absorption line plus a broad Gaussian background due to a low-lying magnetic dipole allowed d-d transition. G: Transient VCD signal recorded at 2872 cm^{-1} (indicated by vertical line in A-F) H: Simulated transient VCD signal for perfectly circular polarised probe pulses (black line) for pulses obtained from the symmetric triggering scheme (green squares) and for pulses after correction for static linear birefringence (blue circles), both plotted with an offset for clarity. See text for further details.

Linear and circular birefringence of the sample are related to the LD and CD by linear response theory [95] and are equally included in the simulations. Since the Jones matrices for linear and circular dichroism do not commute, we used the so-called N-matrix formalism as outlined in section 1 to arrive at a correct description of the sample. The simulation was carried out for probe pulse polarisations produced by our set-up both with and without linear birefringence compensation by asymmetric triggering, yielding the green and blue curves in Figure 4.5 H, respectively. The same simulation for ideal circular polarisation is shown by the black line. The differences are well below the noise level of the experiment and only visible because we assumed a maximal anisotropy of the transient absorption signal (that decays with the rotational diffusion time of 50 ps). Several favourable circumstances contribute to this insensitivity: The shift of the narrow vibrational band is smaller than its bandwidth, leading to strong cancellation in the transient absorption signal and thus the pump-induced anisotropy. The CD changes, on the other hand, are relatively large and are dominated by the weakening of the *d*-*d* electronic contribution which does not contribute to the absorption signal.

4.4 Conclusion

We have demonstrated that time-resolved VCD spectroscopy is experimentally feasible. Equilibrium and time-resolved CD data can be recorded simultaneously with the same set-up (the same set-up being also capable of recording static ORD, see Chapter 5). Benefiting from a relatively large VCD in the electronic ground state, we could record VCD transients for a chiral transition metal complex with sufficient signal to noise ratio for an excitation density of less than 2%. A noise level just below 10 μOD was reached in 90 minutes and may be lowered with longer integration time. Due to a very good control of the probe polarisation (see Chapter 3) and to the predominantly thermal origin of our signal, our experiment is not subject to dominant polarisation artefacts.

Chapter 5

Chiral signals enhancement by self-heterodyning and single-shot measurements

5.1 Introduction

In Chapter 4, we reported on the transient VCD measurements in the CH-stretch region (2800-300 cm^{-1}) following visible excitation of the Cobalt(-) spartein complex Co(sp)Cl$_2$. A transient VCD change of 20 μOD could be resolved in single wavelength scans for this model compound at a noise level of ≈ 8 μOD within 90 minutes of averaging time. This signal to noise level is, in principle, sufficient for applying the new spectroscopy to the study of conformational transition of peptides and proteins where VCD is highly sensitive to secondary structure and its changes [20, 67, 96]. However, information beyond that already accessible by conventional transient IR measurements will only be obtained if full transient VCD spectra (within the bandwidth of a femtosecond mid-IR laser pulse) can be recorded, which require a sensitivity improvement.

Similar difficulties with low signal levels are encountered in non-linear infrared spectroscopy. Here spectral interferometry has been introduced, which enhances a weak signal field (like a photon echo) by interference with a much stronger reference field, also called local oscillator [31]. This heterodyne-detection has made it possible to record the non linear (3rd order) response of IR chromophores, even when their linear absorption is extremely weak [5]. In linear absorption spectroscopy too, the signal is (self-)heterodyne-detected (the incoming light interferes with the linear polarisation it has created itself). However, unlike in third order spectroscopy [97] there is usually no independent control over the co-propagating signal and local oscillator fields and signal enhancement is not possible. The situation is different for chiral samples, where the part of the linear polarisation that gives rise to circular dichroism and optical rotation is polarised perpendicular to the incident field and the two can be separated using polarisers. This has recently been exploited by Rhee et al. who proposed a scheme for the interferometric detection of vibrational CD and optical rotation making use of a separate, local oscillator beam guided around the sample [95]. The result is significant signal enhancement, which has made vibrational ORD measurements possible for the first time [32]. Based on the same principle, Kliger and co-workers have earlier proposed a slightly different detection scheme for time-resolved electronic circular dichroism and optical rotation experiments [33, 98]. We could successfully transfer this technique to the mid-infrared. It has enabled us to significantly improve signal to noise in the measurement of VCD spectra in our set-up designed for transient VCD experiments (see Chapter 4). The local oscillator is now the minor axis component of highly elliptically polarised light. Independent of the sample absorbance and refractive index changes, it maintains a fixed phase shift of $\pi/2$ with respect to the field polarised along the major axis that gives rise to an enhanced chiral linear response. This may be of an advantage in transient VCD measurements, when refractive index changes cause an unknown phase shift of the infrared probe beam.

In the transient vibrational chiral spectrometer reported in the Chapter 2, light dispersion is achieved before the sample by an Ebert-Fastie monochromator. In this configuration, the acquisition of the whole spectrum by mechanically rotating the grating is a slow process during which low frequency noise can easily be picked up. A much more efficient way would be to disperse the probe beam after the sample and detect it on an MCT array detector, this way, the whole spectrum would be acquired in one single laser shot. In addition, the time resolution of the transient set-up, limited by the small probe bandwidth, would regain femtosecond resolution. Unfortunately, this configuration is normally obscured by polarisation sensitive optics of the monochromator. Thanks to the very good control of our polarisation, we could convert, after the sample, the probe pulses into a well-defined linear polarisation states and disperse them onto a multichannel array detector. Full enhanced ORD spectra (200 cm^{-1} bandwidth) in the C-H stretch region of the terpene molecule limonene could be recorded within few minutes. Those results are presented in the second part of this chapter.

5.2 The modified set-up

The time-resolved VCD spectrometer has already been described in detail in Chapter 2; next to transient signals, the set-up can also be used to record static chiral spectra. To achieve VCD and VORD enhancement, only minor modifications of the probe line are required. To record classical non-enhanced VCD signals, the incident linearly polarised light beam is oriented at 45° with respect to the modulator axis which acts as a quarter waveplate of opposite sign for consecutive laser pulses (see Figure 5.1). A modulation amplitude corresponding to $\lambda/4$ thus generates a train of alternatingly left- and right-circular polarised pulses. As it will be explained later, to enhance the VCD signal, elliptical pulses of opposite handedness have to be produced. To do so, the modulation amplitude of the PEM is decreased to produce a phase shift between the orthogonal components of the incident beam smaller than $\lambda/4$. The PEM generates then alternatingly left and right elliptically polarised pulses. A second polariser perpendicular to the first one is inserted in the beam after the modulator (see Figure 5.1).

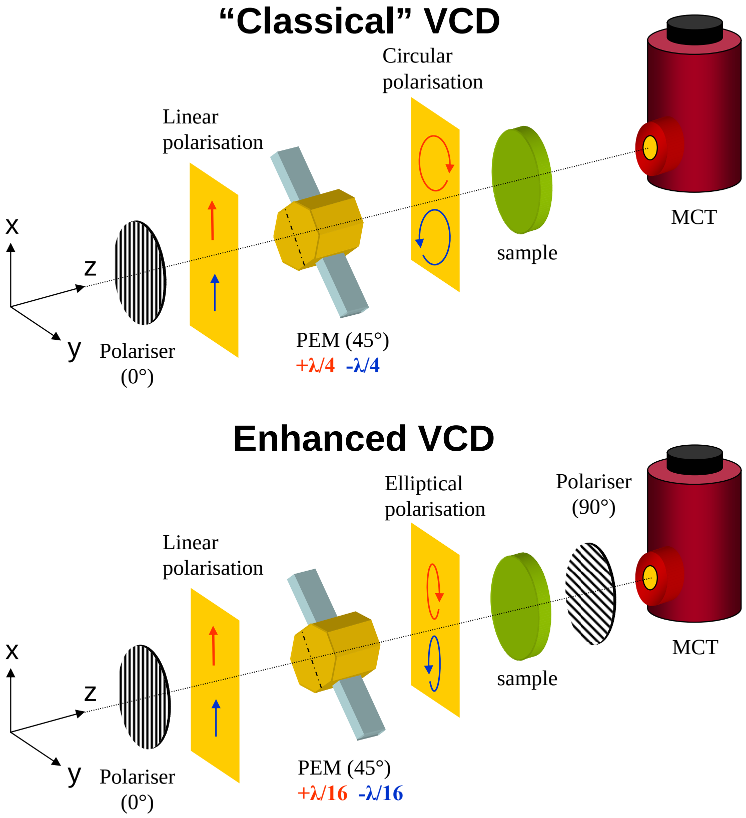
“Classical” VCD

Enhanced VCD

Figure 5.1: Schematic representation of the probe line of the experimental set-up for VCD measurements. The projection of the polarisation state onto a plane perpendicular to the propagation is also represented by the coloured arrows (blue and red corresponds to two successive pulses)

For classical VORD measurements, the linear incident beam comes at 45 degrees, as the PEM retardation alternates between zero and $\lambda/2$ for consecutive laser shots producing a train of pulses with linear polarisation alternatingly inclined by ± 45°. A second horizontal polariser is inserted into the beam before the MCT detector (see Figure 5.2).

For ORD enhancement, the incident angle of the input beam is decreased to a value α as the modulator keeps alterning between 0 and $\lambda/2$ producing a train of pulses with

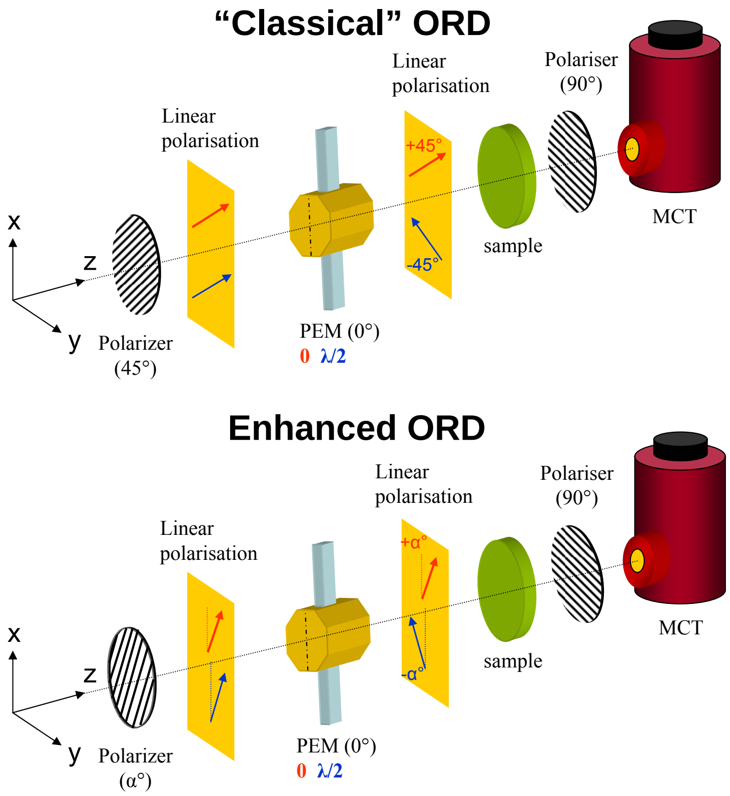

Figure 5.2: Schematic representation of the probe line of the experimental set-up for vibrational ORD measurements. The projection of the polarisation state onto a plane perpendicular to the propagation is also represented by the coloured arrows (blue and red corresponds to two successive pulses)

linear polarisation alternatingly inclined by $\pm\alpha°$.

5.3 Signal enhancement

5.3.1 Jones matrix analysis

VCD enhancement The laser pulses in our experiments propagate in the z-direction. They are linearly polarised in the x-direction before the first polariser. After passing the modulator set on a low retardation, their polarisation is alterning between left- and right-handed elliptical polarisation, their electric fields can be represented by the following Jones vector (see the appendix for more details about Jones calculus)

$$\vec{E}^0_{\pm} = \begin{pmatrix} \cos\theta \\ \pm i \sin\theta \end{pmatrix}. \tag{5.1}$$

Interaction over a length L with a sample of isotropically oriented chiral molecules with absorption coefficients

$\kappa = \ln(10)\epsilon c$, weak circular dichroism $\eta = \ln(10)(\epsilon_L - \epsilon_R)$ and circular birefringence $\delta = \ln(10)\frac{2\pi}{\lambda}(n_L - n_R)$ is taken into account by multiplication with the appropriate Jones matrix [12]

$$\begin{aligned} M_{chiral} &= e^{-\kappa L/2 - i\rho L} \begin{pmatrix} \cos(\frac{\delta L}{2} - i\frac{\eta L}{4}) & \sin(\frac{\delta L}{2} - i\frac{\eta L}{4}) \\ -\sin(\frac{\delta L}{2} - i\frac{\eta L}{4}) & \cos(\frac{\delta L}{2} - i\frac{\eta L}{4}) \end{pmatrix} \\ &\approx e^{-\kappa L/2 - i\rho L} \begin{pmatrix} 1 & -i\frac{\eta L}{4} + \frac{\delta L}{2} \\ i\frac{\eta L}{4} - \frac{\delta L}{2} & 1 \end{pmatrix} \end{aligned} \tag{5.2}$$

The transmitted light is then described by the field vectors

$$\begin{aligned} \vec{E}_\pm &= M_{chiral}\vec{E}^0_\pm \qquad (5.3) \\ &= e^{-\kappa L/2 - i\rho L} \begin{pmatrix} \cos\theta \pm i(\delta L/2 - i\eta L/4)\sin\theta \\ \pm i\sin\theta - (\delta L/2 - i\eta L/4)\cos\theta \end{pmatrix} \end{aligned}$$

and the detector records the intensities

$$I_\pm = \vec{E}^*_\pm \cdot \vec{E}_\pm = e^{-\kappa L}\left(1 \pm \eta L \sin(\theta)\cos(\theta) + O[\delta^2, \eta^2]\right) \tag{5.4}$$

Note that the terms quadratic in δ and η can be ignored, consistent with the linear approximation of the Jones matrix. In our pulsed laser set-up, we separately measure I_+ and I_- and calculate directly the difference in absorption of left- and right-handed polarised light

$$\begin{aligned} \Delta A &= \log\frac{I_+}{I^0_+} - \log\frac{I_-}{I^0_-} = \log\frac{I_+}{I_-} \\ &= \log\frac{1 + \eta L\cos\theta\sin\theta}{1 - \eta L\cos\theta\sin\theta} \approx \frac{2\eta L}{\ln(10)}\cos\theta\sin\theta \end{aligned}$$

If we now put a second polariser oriented in the y-direction behind the sample, the transmitted intensities are

$$I^y_\pm = e^{-\kappa L}\left(\sin^2\theta \pm (\eta L/2)\cos\theta\sin\theta + O(\delta^2, \eta^2)\right) \tag{5.5}$$

yielding the signal

$$\Delta A_y = \log\frac{I^y_+}{I^y_-} = \log\frac{1 + \frac{\eta L}{2}\cos\theta/\sin\theta}{1 - \frac{\eta L}{2}\cos\theta/\sin\theta} \approx \frac{\eta L}{\ln(10)}\frac{\cos\theta}{\sin\theta} \tag{5.6}$$

We may also use the full Jones matrix to arrive at the exact result

$$\Delta A_y = \log \frac{\left(1 + \cot\theta \tanh \frac{\eta L}{4}\right)^2}{\left(1 - \cot\theta \tanh \frac{\eta L}{4}\right)^2} \tag{5.7}$$

which is quasi identical to Equation 5.6 as long as the interaction with the chiral sample does not reverse the handedness of one of the probe pulses, i.e. until chiral sample and PEM have a comparable effect on the polarisation state.

For circular polarised light ($\theta = \pi/4$) the signals ΔA and ΔA_y are both equal to $\eta L/\ln(10)$. However, as illustrated by the red line in Figure 5.3, we can significantly enhance the differential absorption signal ΔA_y using elliptically polarised light ($\theta < \pi/4$). The enhancement factor $\cos\theta/\sin\theta$ is equal to the ellipticity $|E_x|/|E_y|$ of the electric field after the PEM. Note that without a second polariser ΔA is actually becoming smaller (blue line in Figure 5.3).

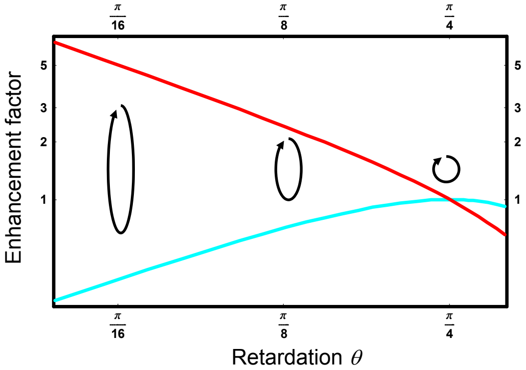

Figure 5.3: Enhancement of VCD signal $\ln(10)\Delta A_y/(\eta L)$, measured between two crossed polarisers, as a function of PEM retardation (red line). The enhancement factor is equal to the ellipticity ($|E_x|/|E_y| = \cos\theta/\sin\theta$) of the electric field, indicated in black. The blue line shows the scaling of the signal ($\ln(10)\Delta A/(\eta L)$) that would be measured without a second polariser.

VORD enhancement It is equally possible to enhance vibrational ORD signals with our set-up. For these measurements, the first polariser is inclined at a small angle α with respect to the modulator axis. The timing of the laser system is such that the modulator is alternatingly inactive or acts as a $\lambda/2$ waveplate, which rotates the inclination of the linearly polarised probe light from -α to +α with respect of the x-axis. A polariser placed after the sample singles out only the y-axis component.

As in the previous section, the laser pulses propagate in the z-direction. They are linearly polarised in the x-direction before the first polariser. After passing the first polariser and the modulator, the linear polarisation alternates between -α and +α (see Figure 5.2). Their electric fields can be represented by the following Jones vector

$$\vec{E}^0_\pm = \begin{pmatrix} \cos\theta \\ \pm\sin\theta \end{pmatrix} \tag{5.8}$$

A sample of length L of isotropically oriented chiral molecules with absorption coefficient $\kappa = \ln(10)\epsilon c$, weak circular dichroism $\eta = \ln(10)(\epsilon_L - \epsilon_R)$ and circular birefringence $\delta = \ln(10)\frac{2\pi}{\lambda}(n_L - n_R)$ can be represented by the following Jones matrix [12]

$$M_{chiral} = e^{-\kappa L/2 - i\rho L}\begin{pmatrix} 1 & -i\frac{\eta L}{4} + \frac{\delta L}{2} \\ i\frac{\eta L}{4} - \frac{\delta L}{2} & 1 \end{pmatrix} \tag{5.9}$$

After the second horizontal polariser, the transmitted light is described by the field vectors

$$\begin{aligned} \vec{E}_\pm &= P_y M_{chiral}\vec{E}^0_\pm \qquad (5.10)\\ &= e^{-\kappa L/2 - i\rho L}\begin{pmatrix} 0 \\ \pm\sin\theta - (\delta L/2 - i\eta L/4)\cos\theta \end{pmatrix} \end{aligned}$$

and the detector records the intensities

$$I^y_\pm = e^{-\kappa L}\left(\sin^2\theta \pm (\delta L)\cos\theta\sin\theta + O(\delta^2, \eta^2)\right) \tag{5.11}$$

Calculating directly the difference in absorption between two successive pulses gives

$$\Delta A_y = \log\frac{I^y_+}{I^y_-} = \log\frac{1 + \delta L\cos\theta/\sin\theta}{1 - \delta L\cos\theta/\sin\theta} \approx \frac{2\delta L}{\ln(10)}\frac{\cos\theta}{\sin\theta} \tag{5.12}$$

In classical VORD measurements, $\theta = \pi/4$ and no enhancement is observed. Nonetheless, we can significantly increase the VORD signal by reducing the angle θ of the first polariser, at the cost of reducing the amount of light on the detector, the enhancement factor is equal (as for VCD) to $\cos\theta/\sin\theta$. Note that in the case of VORD, no VORD signal can be recorded without the presence of the analyser.

Similar results have been derived previously by the Kliger group [14,33], who demonstrated a similar scheme for nanosecond time-resolved electronic CD and ORD spectroscopy. In their initial set-up a strain plate was used instead of a PEM, which had to be rotated mechanically from -45 ° to +45 ° with respect to the first polariser in order to produce elliptical light of opposite handedness [14]. The strain plate gave rise to a very small retardation $\theta \approx 10^{-2}$, which corresponds to an enhancement factor of 100.

5.3.2 Linear response picture

It is instructive to look at the above result from a linear response point of view. Indeed, the Jones matrix of Equation 5.2, in the language of linear response theory, reflects the fact that an incident x-polarised electromagnetic field $E(t) = E_x e^{i\omega t}$ interacting with an isotropic ensemble of chiral molecules gives rise to a linear polarisation, which is the source of a y-polarised electromagnetic field (free induction decay) $\tilde{E}_y(t) = e^{-\kappa L/2}(\delta L/2 + i\eta L/4)E(t)$. Singled out by a polariser oriented in the y-direction, $\tilde{E}_y(t)$ can be superimposed with a y-polarised local oscillator field $E^{LO} = E_0 e^{i\omega(t+\tau)}$. After dispersion (before or after the sample) a square-law detector then measures the signal in the frequency-domain

$$\begin{aligned} & |\tilde{E}_y(\omega) + E^{LO}(\omega,\tau)|^2 \\ = \; & |E_0(\omega)|^2 + |\tilde{E}_y(\omega)|^2 + 2Re[\tilde{E}_y E_0 \exp(-i\omega\tau)] \\ = \; & |E_0(\omega)|^2 + |(\frac{\delta L}{2} + i\frac{\eta L}{4})E_x(\omega)\exp(-\frac{\kappa L}{2})|^2 \\ & +2Re[(\frac{\delta L}{2} + i\frac{\eta L}{4})E_x(\omega)\exp(-\frac{\kappa L}{2})E_0(\omega)\exp(-i\omega\tau)] \end{aligned} \tag{5.13}$$

For a given frequency ω we may choose both $E_0(\omega)$ and $E_x(\omega)$ to be real. We must also neglect non-linear terms in η and δ, which simplifies the above expression

$$\begin{aligned} & |\tilde{E}_y(\omega) + E^{LO}(\omega,\tau)|^2 \\ = \; & E_0^2(\omega) + Re[(\delta L + i\frac{\eta L}{2})E_x(\omega)e^{-\frac{\kappa L}{2}}E_0(\omega)\exp(-i\omega\tau)] \end{aligned} \tag{5.14}$$

In our set-up (or that of reference [33]), the x-component of the incident elliptically polarised light induces the y-polarised free induction decay while the weaker y-component of the incident field acts as the local oscillator with $\tau = \pm\frac{\pi}{2\omega}$ for right- and left-handed pulses, respectively (self-heterodyning). (E_0 is equally attenuated by $e^{-\kappa L/2}$ at the detector and this factor therefore cancels). Taking the logarithm of the ratio of the corresponding intensities again yields the result of Equation 5.6

$$\begin{aligned} & \log\frac{|\tilde{E}_y(\omega) + E^{LO}(\omega,\tau=\frac{\pi}{2\omega})|^2}{|\tilde{E}_y(\omega) + E^{LO}(\omega,\tau=\frac{-\pi}{2\omega})|^2} \\ = \; & \log\frac{E_0^2(\omega) + Re[-i(\delta L + i\frac{\eta L}{2})E_x(\omega)E_0(\omega)]}{E_0^2(\omega) + Re[i(\delta L + i\frac{\eta L}{2})E_x(\omega)E_0(\omega)]} \\ = \; & \log\frac{1 + (\eta L/2)E_x(\omega)/E_0(\omega)}{1 - (\eta L/2)E_x(\omega)/E_0(\omega)} \approx \frac{\eta L}{\ln(10)}\frac{E_x(\omega)}{E_0(\omega)} \end{aligned} \tag{5.15}$$

Instead of elliptical light, two independent, linearly polarised beams may be also be used. The enhancement of the VCD signal measured using elliptical light and two crossed polarisers is indeed fully equivalent to the signal enhancement obtained by spectral interferometry, which was proposed by Rhee et al. [32, 95]. In that set-up the local oscillator field is split off before and guided around the sample and overlapped with the free induction decay $\tilde{E}_y(t)$ only after the second polariser. The phase factor $\exp(-i\omega\tau)$ in Equation 5.14 depends on the relative optical path of the two beams and is not known a priori in this case. However, it can be eliminated by measuring a second signal with both polarisers and the local oscillator polarised parallel to the incoming field $E(t)$ [95, 99]. The two measurements together allow one to simultaneously determine VCD and vibrational ORD signals.

The same analysis can be done for ORD signals. Recall that for ORD, the modulator acts alternatingly as inactive or as a $\lambda/2$ waveplate. The phase factor τ in Equation 5.14 is then alternatingly zero or $\tau = \frac{\pi}{\omega}$ and the measured signal becomes

$$\begin{aligned} & \log \frac{|\tilde{E}_y(\omega) + E^{LO}(\omega, \tau = 0)|^2}{|\tilde{E}_y(\omega) + E^{LO}(\omega, \tau = \frac{\pi}{\omega})|^2} \qquad (5.16) \\ = \; & \log \frac{E_0^2(\omega) + Re[(\delta L + i\frac{\eta L}{2})E_x(\omega)E_0(\omega)]}{E_0^2(\omega) + Re[-(\delta L + i\frac{\eta L}{2})E_x(\omega)E_0(\omega)]} \\ = \; & \log \frac{1 + \delta L E_x(\omega)/E_0(\omega)}{1 - \delta L E_x(\omega)/E_0(\omega)} \approx \frac{2\delta L}{\ln(10)} \frac{E_x(\omega)}{E_0(\omega)} \end{aligned}$$

The relative magnitude of the x-polarised excitation field E_x and the y-polarised local oscillator E_0 is $\cos\theta'/\sin\theta'$ and significant enhancement of the ORD signal is thus achieved by reducing the inclination θ' of the first polariser.

It is not difficult to show that, as long as the linear response approximation is valid, modulator and sample can be exchanged without affecting Equations 5.6 and 5.16. The role of the second polariser is to completely block the x-polarised free induction decay created by the y-polarised local oscillator component of the elliptically polarised light. Likewise, any polarisation component in the x-direction created by the modulator behind the sample originating from a y-polarised FID is eliminated. We may therefore, create the local oscillator field behind the sample and use a linearly (x-)polarised probe beam without changing the transmitted light intensities. A similar analysis shows that ORD measurements with exchanged sample and modulator positions are equally possible, if the second polariser instead of the first one is now inclined at a small angle with respect to the optical axis of the PEM. This configuration might be more adapted to pump-probe techniques as the probe and the pump are then both linearly polarised and their orientation can be chosen to minimize polarisation artefacts.

5.4 Experimental results

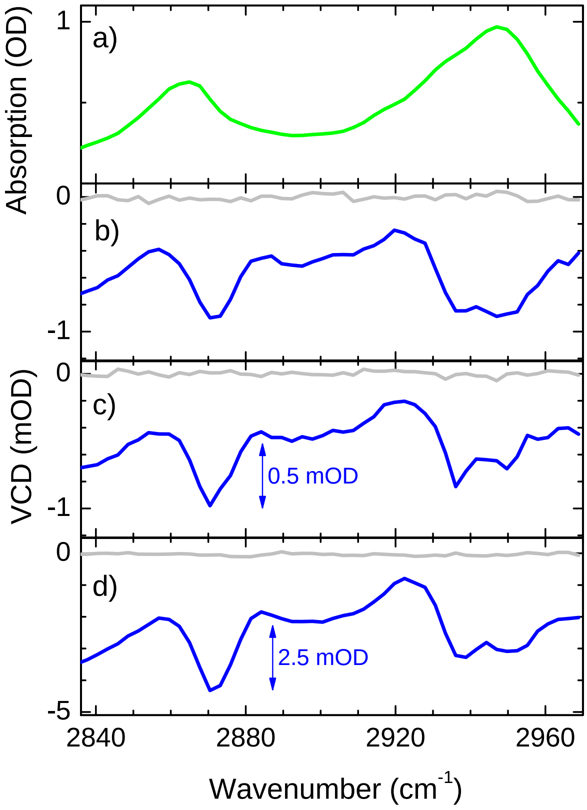

Figure 5.4: a) CH-stretch absorption of Co(sp)Cl_2 dissolved in $CHCl_3$ (sample thickness 100 μm). b) VCD signal , recorded with the dispersive VCD spectrometer using alternatingly left- and right-circular polarised laser pulses (PEM retardation $\lambda/4$). c) same VCD spectrum recorded with a second polariser placed between sample and detector. d) Data recorded using elliptical pulses (PEM retardation $\lambda/16$). The noise level is indicated by the grey lines, which show the difference between two consecutive sets of scans of 200 seconds each.

We first demonstrate VCD signal enhancement on the (-)-sparteine cobalt complex investigated in Chapter 4. Low-lying magnetic dipole-allowed $d-d$ transitions of the open-shell transition metal atom give rise to a broad electronic CD signal, which underlies the vibrational CD in the C-H stretch region. They are responsible for the negative offset in the spectra shown in Figure 5.4 and enhance the vibrational signal by an order of magnitude with respect to that of the corresponding Zinc complex [24]. Already the conventional VCD signal, recorded using circular polarised pulses is therefore, relatively large and could be recorded within a few minutes (Figure 5.4b). Still using circular polarised pulses, we placed the second crossed polariser behind the sample and repeated the same scan (Figure 5.4c). Subsequently the modulator retardation was reduced to $\lambda/16$. Neutral density filters were removed from the laser beam path in order to maintain the same light level at the detector as in the measurements with circular polarised light. Consistent with the prediction of Equation 5.3, the measured signal is now five times larger, while the noise level is practically unchanged (see Figure 5.4d).

As a second example, we show the enhanced VCD signal of azide bound to ferric myoglobin (from horse skeletal muscle, Aldrich) in Figure 5.5b, equally recorded with elliptically polarised laser pulses (PEM retardation $\lambda/16$). Although our intense laser light source allows us to use an unusually thick sample cell (100 μm), which causes the large background absorption of the D_2O phosphate buffer (Figure 5.5a), the size of the VCD signal recorded with circular polarised pulses at a myoglobin concentration of 20 mM is only 200 μOD (data not shown). With an enhancement factor of 5, the signal could nevertheless be recorded reliably within only 10 minutes (Figure 5.5b).

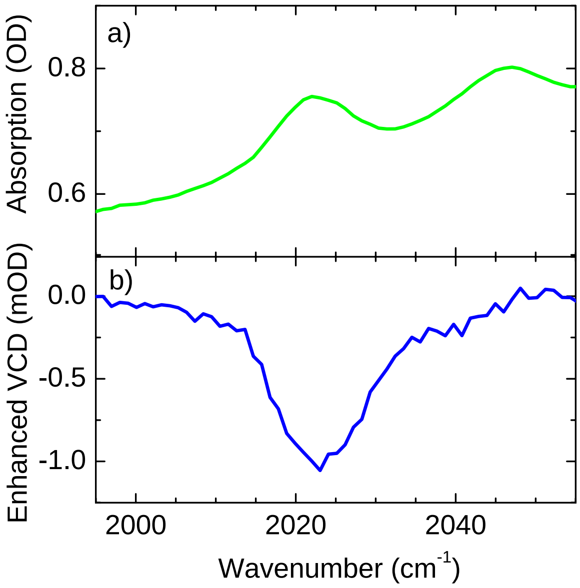

Figure 5.5: Asymmetric stretch of azide bound to myoglobin in 0.1 M D_2O phosphate buffer (sample thickness 100 μm). a) Absorption b) Enhanced VCD signal recorded with elliptical polarised pulses. The PEM retardation was set to $\lambda/16$, corresponding to an enhancement factor of 5.

Note that the second absorption band at 2044 cm^{-1}, which shows no dichroism is due to weakly bound N_3 in the heme pocket [100] as well as free azide ions in the buffer solution.

As an example of the second application of our modulator set-up, Figure 5.6 shows the vibrational optical rotary dispersion spectrum in the C-H stretch region of (R) and (L)-limonene (Aldrich) dissolved in CCl_4. This molecule was chosen in order to allow a direct comparison between the modulator- and interferometric technique [32] for ORD measurements. We recorded data with a polariser inclination $\theta' = 5°$, using both the set-up shown in Figure 2.5b (squares) as well as Figure 2.5c (solid lines), i.e. with the PEM placed before and after the sample. Despite a very small optical rotation of 2×10^{-5} radians [32], enhancement leads to a peak to peak signal equivalent to a 1 mOD absorption change, which can be readily measured. The subtracted ORD spectra of the two enantiomers (L-R, Figure 5.6 bottom) are quasi identical (differences in signal to noise are mainly due to laser performance on different days). On the other hand, the individual spectra, which are obtained by subtracting a background scan of pure solvent, are not perfect mirror images and small, but systematic deviations between the two sets of data can be seen. Larger uncertainties in the background spectrum can be attributed to the fact that it must be recorded using additional filters in the beam path in order to compensate the much higher solvent transmission, an illustration of the dynamic range problem of mid-IR detectors. However, this should not pose any problem in transient measurements, where pump-induced transmission changes are very small. A much smoother background signal was obtained in the second set of measurements (solid lines, PEM behind the sample) where calcite polarisers with a very high extinction ratio in this very narrow wavelength range ($10^{-8} - 10^{-9}$) were used [76]. Nevertheless, our data shows that wire-grid polarisers with an extinction ratio just greater than 10^{-4} throughout the mid-IR are, in principle, sufficient to record useful data.

5.5 Single-shot ORD enhancement

Polarisation-based artefacts are a great source of concern in static and transient vibrational chiral spectroscopy. They prevent, in static dispersive VCD/VORD spectrometers, the dispersion of the light after the sample (see Figure 1.6 representing a typical dispersive VCD/VORD set-up). Spectra are obtained rotating the monochromator's grating, which increases the measurement time and allows low frequency noise to be picked up during the scanning process. In the case of a transient VCD/VORD experiment, selecting a narrow bandwidth of the infrared probe beam before the sample, also limits the time resolution achievable. In a pump-probe experiment, the time resolution is mainly dictated by the duration of the pulses ($\approx$ 150 fs in the case of our set-up), narrowing the probe pulses to few nanometres restricts the time resolution to a few picoseconds. In classical infrared pump-probe spectroscopy, probe light is dispersed after the sample on an MCT array detector allowing the whole spectrum to be acquired, with correlated noise, in a single laser shot. Multichannel detection causes a dramatic improvement of the SNR.

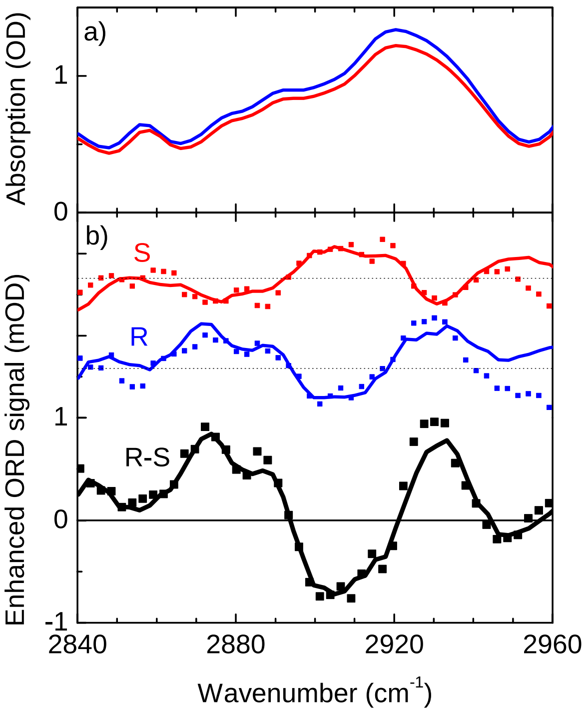

Figure 5.6: CH stretch vibrations of limonene dissolved in CCl_4 (sample thickness 100 μm). a): Absorption b): Vibrational ORD signal of R- and L-forms (blue and red) recorded with a polariser inclination of 5°. The difference between the two enantiomer spectra is shown at the bottom (measurement time 13 minutes for each enantiomer and the solvent background). Solid squares: Polarisation modulation before the sample, wire-grid polarisers; Solid lines: Polarisation modulation after the sample, calcite polarisers.

Such a configuration has unfortunately not been implemented due to polarisation-based artefacts. Grating and concave mirrors are polarisation sensitive optics and light has to be linearly polarised prior entering the monochromator to avoid spurious artefacts. Simplest way to ensure this, is to place a second polariser after the sample. This second polariser, compulsory for VORD measurements, should not influence the VCD signal. Unfortunately, a polariser is nothing else than an extreme linear dichroic plate, which will interact with the linear components of the probe beam giving rise to dominating artefacts (see the section about polarisation artefacts in Chapter 3).

Thanks to the very good control of the polarisation probe beam, we could already measure static VCD and VORD spectra with an additional polariser after the sample (see, for example, Figure 5.4 and Figure 5.5) without experiencing disturbing artefacts. Those spectra were a prerequisite for the implementation of multichannel detection. The set-up built to achieve single-shot VCD/VORD measurements is described in Figure 5.7. A small part of the mid-IR beam coming out the optical parametric amplifier (see Chapter 2) is

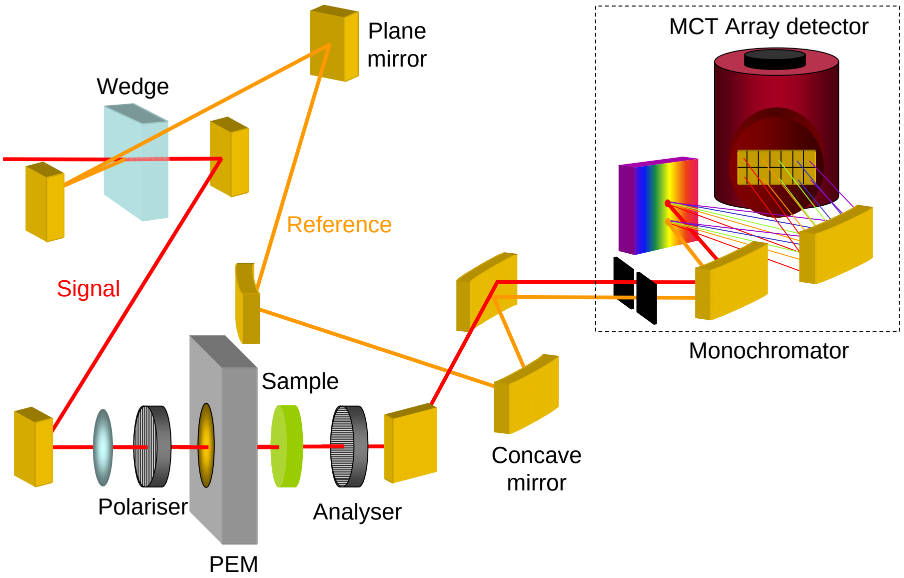

Figure 5.7: Schematic description of the multichannel detection VCD/VORD set-up. See text for details.

reflected off a wedged BaF_2 window and will be used as a reference for compensating laser fluctuations. The transmitted part is used as IR-probe beam.

The probe beam is then directed onto a typical set-up to measure VCD/VORD signals (see Figure 5.7): A ZnSe lens focuses the beam onto the sample and a combination of a polariser and a PEM generates the desired polarisation modulation. After the sample, a compulsory polariser is placed. Both the reference and the probe beam are then spectrally dispersed in a grating spectrometer and focused onto a double array MCT (Mercury Cadmium Telluride, HgCdTe) detector (2×31). The typical resolution at 6 μm is 4 cm^{-1} with a total IR-probe window of 120 cm^{-1}. As described in Chapter 3, we synchronize the laser source to the fix PEM natural frequency (50.01 kHz) so that pulses cross the modulator each time it acts as a quarter waveplate for VCD measurements or as a half waveplate for VORD, with an opposite sign for consecutive pulses. The intensities on each pixel is recorded for every laser shot using home built gated amplifiers followed by 12 bits analogue/digital conversion. The VCD signal is then evaluated for each pixel in the computer as the log-ratio of an average (typically 300-1000) probe pulse intensities, corrected by the appropriate reference signals.

For enhanced VORD measurements, the first polariser is inclined by a small angle α in comparison to the vertically oriented modulator. The analyser is horizontal, perpendicular to the PEM's axis. As mentioned earlier, we can invert the sample and the photo elastic modulator without modifying the signal; the analyser, instead of the first polariser, has then to be inclined by a small angle α. This second configuration where the sample is illuminated by linearly polarised light should be less sensitive to linear dichroism artefacts

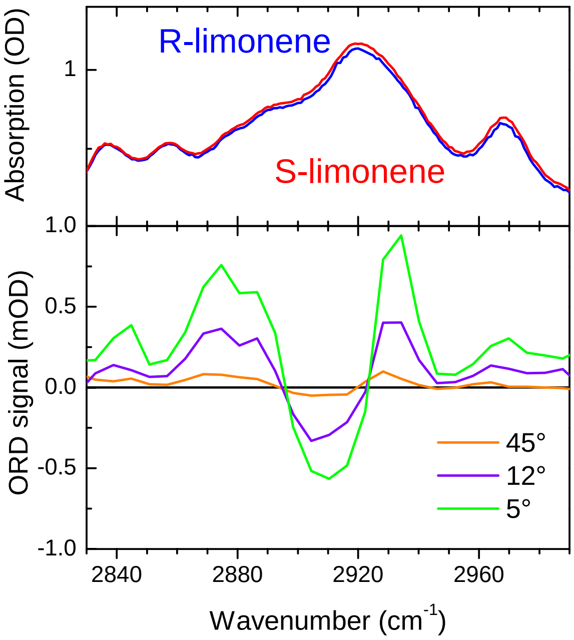

Figure 5.8: Single-shot ORD enhancement of limonene. Top: Absorption spectrum of R and S limonene in the C-H stretch region. Bottom: ORD spectrum of limonene recorded for different enhancement factors. The green curve has been acquired with the analyser at 5 ° corresponding to an amplification of roughly 11, the violet with an analyser angle of 12 ° corresponding to an amplification of roughly 5. The orange curve has been acquired with the analyser at 45 ° which corresponds to no amplification. The spectra are difference spectra of the two enantiomers (R minus the S)to remove spurious background signals. See text for details.

originating from pump-induced anisotropy.

We could successfully record, with this set-up, enhanced VORD spectrum in the C-H stretch region of the terpene molecule limonene (Aldrich) within few minutes. The VORD spectra for different enhancement factors are represented on Figure 5.8. Those are, to our knowledge, the first single-shot vibrational chiral spectra ever recorded. However, some technical difficulties still remain. Spectra presented in Figure 5.8 are difference spectra of the two enantiomers (R and S). This subtraction allows the removal of a large intensity-sensitive background. This background, impossible to remove by classical procedures such as the subtraction of the solvent signal, is not fully understood yet. The quality of the polarisers, used to clean the polarisation of the incident probe beam and as an analyser after the sample, remains an issue. We are using at the moment two different types of polarisers: Wire grid and dichroic calcite polarisers. Wire grid polarisers [75] can be used over an extended frequency range with an acceptable extinction ratio ($\approx 10^{-4}$). Dichroic calcite polarisers exhibit an exceptional extinction ratio ($\leq 10^{-8}$) but are only usable over a really limited frequency ranges [76]. For reasons still unclear to us, the wire grid polarisers give rise to a spurious, structured, intensity-dependent baseline. Spectra recorded with dichroic calcite polarisers are less sensitive to this background signal and exhibit a significant better quality (see Figure 5.6). Unfortunately, their small usable frequency range, limits their utilisation to the C-H stretch region. High quality Brewster angle polarisers consisting of four germanium plates arranged in a chevron geometry [77] are currently used in Cho's group in a Fourier-like experimental set-up with good results [32, 101]. Such polarisers, susceptible to reduce the spurious baseline artefacts, are currently built in our laboratory.

5.6 Conclusion

The examples above illustrate, how the use of crossed polarisers in combination with a photo elastic modulator opens new possibilities for the independent manipulation of the incident light field and the chiral component of the linear free induction decay in vibrational CD and ORD measurements. This is particularly attractive when short laser pulses are used, allowing to record transient VCD signals with picosecond time resolution (see Chapter 4). In addition, the intensity of short laser pulses is much higher than that of (quasi-)continuous light sources usually employed in static or nanosecond time-resolved chiral spectroscopy [98]. The strong attenuation of the probe beam by the second polariser placed behind the sample does therefore, not lead to low light levels at the mid-IR detectors provoking larger noise. Rather, a much larger chiral FID is created by photons, which would otherwise be lost in filters that are necessary in single-polariser measurements because of the limited dynamic range of mid-IR detectors.

The crossed polariser or quasi-null technique was introduced and is currently used by the Kliger group for time-resolved UV-visible CD and ORD spectroscopy [14, 15, 98]. The most important practical modification of this method in our mid-infrared set-up is the use of the photo elastic modulator, which replaces the mechanical rotation of a polariser or a strain plate. We anticipate that the combination of kiloherz switching between two well-defined polarisation states (which reduces the noise level to less than 3×10^{-5} OD per second integration time), signal enhancement (affording static signal levels of 10^{-3} OD) and multichannel detection (affording the whole laser spectrum with one single-shot, with correlated noise) will significantly improve our capability to record transient chiral vibrational spectra. Our enhancement method can equally be related to that developed by Hache and co-workers for femtosecond chiral UV-vis spectroscopy. This group has placed a variable waveplate (Babinet-Soleil compensator) between the sample and the second polariser and measures signals as a function of waveplate retardation (CD) or polariser angle (ORD) [102]. This is fully analogous to our set-up, when the photo elastic modulator is placed behind the chiral sample. The shot-to-shot switching between opposite polarisation states replaces the slow variation of Babinet-Soleil retardation or analyser angle, promising the signal to noise enhancement necessary to tackle small mid-IR signals.

In contrast to the spectral interferometer technique introduced by Cho and co-workers, which uses a local oscillator guided around the sample [32, 101], our modulator-based approach is based on self-heterodyning, i.e. the local oscillator can be viewed as a polarisation component of the probe beam. This automatically assures a fixed phase relation between local oscillator and (chiral) free induction decay, which is maintained regardless of the mechanical instability of optical components or the refractive index changes in the sample that always accompany the photo-triggering of a chemical reaction. In (achiral) transient two-dimensional infrared (2D-IR) spectroscopy, these refractive index changes can create serious difficulties for the heterodyne detection of the third-order non-linear response unless the local oscillator field equally passes the excited sample volume [103,104]. This problem is automatically avoided in a self-heterodyning pump-probe approach [93] in full analogy to a single-beam transient VCD or ORD spectrometer.

Chapter 6

Summary and Outlook

In this thesis, we have reported on the development of the first transient vibrational chiral spectrometer, capable of detecting photo-induced VCD changes with picosecond time resolution. Due to very small signals size and the possibility of large polarisation artefacts, the building of a transient chiral spectrometer in the infrared spectral region had remained a challenge.

Artefacts in vibrational chiral spectroscopy mainly originate from the interaction of a non-perfectly polarised probe beam with an anisotropic sample. In VCD spectroscopy, for example, remaining non symmetric linearly polarised components of the probe beam polarisation will give rise to dominating linear dichroic signals. The probe beam polarisation can be distorted by the static residual linear birefringence of the modulator but also by the stress-induced birefringence of optics such as lenses or cells windows. Sample isotropy can be broken by the pump beam.

To minimise those spurious signals, we have developed a method based on an asymmetric triggering scheme between the polarisation modulator and our laser system the aim of which is to compensate for the residual static birefringence of the modulator and the stressed optics. The generated probe beam polarisation is almost perfect which largely reduces the possible unwanted linear dichroic signals.

With the transient set-up developed in our laboratory, we could detect VCD changes in the CH-stretch region following visible excitation of a cobalt spartein complex ($\mathrm{Co(sp)Cl_2}$) with picosecond time resolution. A transient VCD change of several μODs could be resolved in single wavelength scans for this model compound. This is to our knowledge the first transient VCD signal ever recorded. Vibrational chiral signals remain small and the quality of the transient signals recorded need to be improved before being able to investigate the dynamics of more complex biological systems. Toward this goal, we have implemented two technical improvements which have significantly increased the signal to noise ratio of the static VCD/VORD spectra and should, the same way, ameliorate the quality of the transient chiral signals.

First, we have proposed a self-heterodyning chiral signal enhancement configuration: VCD spectra are recorded using elliptically polarised pulses, the short axis of the elliptical light acting as a phase-locked local oscillator field heterodyning the chiral signal generated by the field along the long polarisation axis. This leads to VCD signals that increase linearly with the ellipticity of the probe pulses and enhance the signal to noise ratio. An analogue scheme has been developed for vibrational optical rotatory dispersion measurements with comparable enhancement. As a proof of principle, this technique has been applied to record the VCD signals of Co(sp)Cl_2 and (MbN_3) and to the VORD spectrum of limonene.

The second improvement consists of multi channel detection of the vibrational chiral signals. This had been prevented so far by the polarisation sensitive optics of the monochromators. Indeed, in dispersive vibrational chiral spectrometers, the light is usually dispersed before the modulator to avoid the interaction of the probe beam with the polarisation sensitive optics of the monochromator, such as grating or concave mirrors. This dispersion, prior to the sample, slows down the measurement, allows low frequency noise to be picked up during the scanning process and in the case of transient measurements limits the time resolution achievable to a few picoseconds. Thanks to the very good control of our probe beam polarisation, we could successfully develop a configuration where the light is dispersed after the sample and detected by an array detector affording “single-shot” spectra with correlated noise. VORD spectra in the C-H stretch region of limonene could be measured within a few minutes.

The implementation of multichannel detection and self-heterodyning enhancement on the time-resolved vibrational chiral set-up is quite promising and will probably be the next step in the development of the transient VCD/VORD spectrometer built in our laboratory. It should enable to achieve femtosecond resolution for transient experiments and thanks to a much better signal to noise ratio, allow the measurement of a full transient spectrum instead of single wavelength transient VCD/VORD signals.

However, remaining technical problems such as the quality of the polarisers and the removal of residual baseline artefacts, not totally understood yet, need to be addressed. Wire grid polarisers which we think are the cause of an unknown structured baseline are currently replaced by reflective Brewster polarisers.

For the sake of simplicity and intrinsic phase stability, we have implemented a dispersive version of our transient vibrational chiral spectrometer, although a Fourier transform configuration presents many advantages for static measurements. Very recently, Cho and co-workers were able to record static vibrational optical activity using femtosecond infrared pulses and a Fourier-like experimental set-up. Such a configuration is also currently under development in our laboratory, to test its ability for transient vibrational chiral measurements.

After the proof of feasibility of transient vibrational chiral spectroscopy, the technical developments presented in this thesis should allow, in a near future, the measurement of transient vibrational chiral spectra of biomolecules. The technique will make it possible to identify chiral intermediates in the course of a chemical reaction or to probe with unprecedented details, local secondary structure formation in peptides and proteins, a field of current intense research.

Appendix - The description of polarisation in classical physics

Introduction

There are several mathematical ways of representing light. The most common representations are the Jones vector, the Stokes vector and the density matrix; those have been extensively described in the literature.
The Jones vectors [105] may be thought of as being analogous to any of the Maxwell field vectors E, H or to the potential vector A. Like the transverse components of these vectors, the Jones vector is two dimensional and is written in complex form in order to introduce phase difference between the components.
The components of the Stokes vectors [106] are intensities. The first component is the total intensity and the other three components describe the polarisation of the light in terms of the extend to which it is linearly polarised at 0 ° and 45 ° relative to a chosen axis and the degree to which it is circular polarised. For completely polarised light, one can transform freely from the Jones representation to the Stokes representation.
The two representation are thought limited in different ways. The stokes vector can describe unpolarised or partially polarised light but contains no phase information. The Jones vector is associated with a phase factor and can be used in describing interference phenomena but it cannot be used for partially or unpolarised light. In practical experiments, one ultimately measures intensities and Stokes representation is convenient. On the other hand, it is easier to develop fundamental relationship with the Jones vectors because they are two-dimensional and satisfy a simple spinor algebra.
The coherency matrix formalism is the most recent description [107]. In this formulation, a 2×2 complex matrix describes the polarisation of perfectly polarised, partially polarised and unpolarised light. The coherency matrix is a special occurrence of the more general density matrix used in quantum theory to deal with pure and mixed quantum states.
The aim of this appendix is to introduce those different representations: The first section introduces the basic concept of polarisation state, the second and third section present the

Jones and Stokes formalism respectively. The fourth part briefly introduces the coherency matrix formalism and develop mathematical tools to go from Jones to Stokes representation whereas the fifth part introduces the basic modulation techniques. Finally, the last part builds the bridge between Jones matrix parameters and the linear response theory used to describe advanced spectroscopic systems.

We restrict ourselves in the rest of the document to quasi-monochromatic plane waves, by quasi-monochromatic we mean that the wavelength range $\Delta\lambda_0$ is small compare to the mean wavelength λ_0 and by planar that the electric field is restricted to a plane perpendicular to the direction of propagation. More complex representations capable of handling arbitrary wave forms [108, 109] are not discussed here.

The referential used is depicted on Figure 6.1.

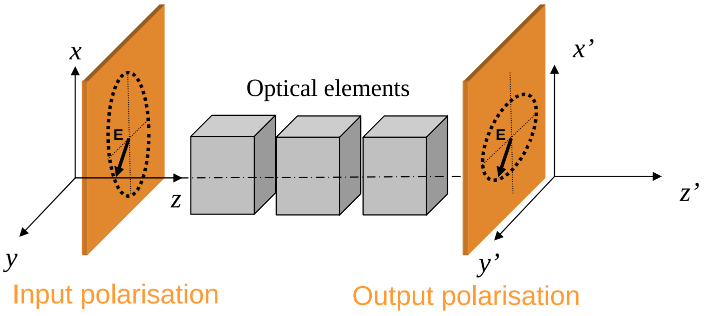

Figure 6.1: Optical elements acting on the input polarisation

A series of optical instruments are placed in the beam modifying its polarisation, z-axe is taken as the direction of propagation. The only phenomena we consider are: Absorption, refraction, dichroism and birefringence; we thus neglect all effects coming from light scattering. The discussion will also be restricted to linear optical systems which can be represented by an operator O_p so that

$$v_f = O_p v_i. \tag{6.1}$$

where v_i and v_f comprise the set of parameters that describe the state of the incoming and outgoing (final) light beam, i.e., intensity polarisation and phase.

State of polarisation

The polarisation ellipse A planar, quasi-monochromatic light beam can always be represented by a two dimensional vector containing the transverse Maxwell electric fields [110]

$$\vec{E} = \begin{pmatrix} E_x(t) = E_{0x}(t)e^{i(-2\pi\overline{\nu}t+\phi_x(t))} \\ E_y(t) = E_{0y}(t)e^{i(-2\pi\overline{\nu}t+\phi_y(t))} \end{pmatrix}. \tag{6.2}$$

Where $E_{0x}(t)$ and $E_{0y}(t)$ are the instantaneous vertical and horizontal amplitudes of the two components, $\phi_x(t)$ and $\phi_y(t)$ their instantaneous phase factor, $\overline{\nu}$ the average frequency and we adopted the complex representation of the cosinusoids.
At all times the amplitudes and phase factors fluctuate slowly compared to the rapid vibrations of the cosinusoids. The explicit removal of the time dependence between the two components of 6.2 leads to [110]

$$\frac{E_x^2(t)}{E_{0x}^2(t)} + \frac{E_y^2(t)}{E_{0y}^2(t)} - \frac{2E_x(t)E_y(t)}{E_{0x}(t)E_{0y}(t)} \cos\delta(t) = \sin^2\delta(t). \tag{6.3}$$

Where $\delta(t) = \phi_x(t) - \phi_y(t)$.
Equation 6.3 is recognized as the equation of an ellipse and shows that at any instant of time the locus of points described by the optical field as it propagates is an ellipse. This behaviour is spoken of as optical polarisation and 6.3 represents the **polarisation ellipse**. In Figure 6.2 the ellipse is shown inscribed within a rectangle whose sides are parallel to the coordinate axes and whose lengths are $2E_{0x}$ and $2E_{0y}$.

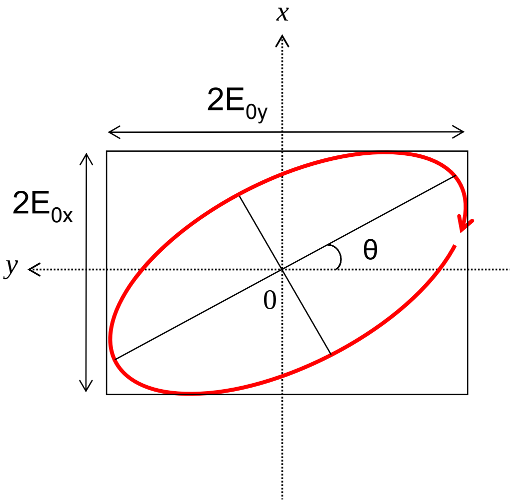

Figure 6.2: An elliptically polarised wave.

Special degenerated forms of the polarisation ellipse The polarisation ellipse degenerates to special forms for certain values of E_{0x}, E_{0y} and δ. For example, if $E_{0y} = 0$ then, the oscillation only occurs in the vertical direction. The light is then said to be linearly polarised in the x direction and we call this linear vertical polarised light. Similarly,

if $E_{0x} = 0$, then we have a linear oscillation along the y axis and we speak of linear horizontally polarised light.
If $E_{0x} = E_{0y} = E_0$ and $\delta = \frac{\pi}{2}$ or $\frac{3\pi}{2}$ then, the ellipse Equation 6.3 reduces to the equation of a circle. Two cases of polarisation are distinguished according to the sense in which the end point of the field vector describes the circle. If $\delta = \frac{\pi}{2}$ the polarisation is said to be right-circular (For an observer looking in the direction from which the light is coming, the end point of the electric vector would appear to describe the ellipse in the clockwise sense) or left-handed if $\delta = \frac{3\pi}{2}$ (For an observer looking in the direction from which the light is coming, the end point of the electric vector would appear to describe the ellipse in the counter-clockwise sense).

Conclusions We have seen that the elimination of the time dependence between the transverse components of the optical field led to the polarisation ellipse. Analysis of the ellipse showed that for special cases it led to forms which can be interpreted as linearly polarised light and circular polarised light, those are called the **polarisation states** of the light. This description in terms of the polarisation ellipse is useful as it enables to describe by the mean of a single equation, various states of polarisation. This representation is however limited to perfectly polarised light.
A natural light source is constituted from many atomic randomly oriented emitters, each emits a pulse of polarised light those duration is approximately 10^{-8} s. New pulses are continuously emitted and the global polarisation changes in a completely unexpected way. The light is said to be natural or unpolarised. It is not possible to detect a well defined state of polarisation. The only measurable quantity would be a time average of the transverse electric components. Averaging Equation 6.3 leads to the Stokes description of polarisation and will be developed later in this appendix. Nonetheless, a simplification happens when the light is purely monochromatic (laser light for example). In this case, the emitted pulses are infinitely long and the polarisation is conserved, E_{0x}, E_{0y} and δ are constant with time leading to only one state of polarisation. This monochromatic approximation is assumed in the Jones formalism.

The Jones formalism

The Jones vectors Jones formalism restricts itself to perfectly monochromatic (and hence perfectly polarised) radiation. In the case of perfectly polarised light, the phase difference between the two transverse components is constant so that the vector $\vec{E}$ representing the transverse electric field can be rewritten in a simpler manner

$$\vec{E} = \frac{1}{\sqrt{E_{0x}^2 + E_{0y}^2}} \begin{pmatrix} E_{0x} \\ E_{0y}e^{i\delta} \end{pmatrix}. \tag{6.4}$$

Where we normalized the vector and dropped the time dependence $e^{-i2\pi\nu t}$. $\vec{E}$ is called the **Jones vector** [105]: It is a complex vector which fully describes the polarisation of a monochromatic wave at a spatial position z.

We can derive the different Jones vectors for usual polarisation states [49] (see Table 6.1)

Table 6.1: Normalised Jones vectors for typical polarisation states

State of polarisation	Normalized Jones vectors
$\vec{E}_v$, Plane of polarisation in the x direction	$\begin{pmatrix} 1 \\ 0 \end{pmatrix}$
$\vec{E}_h$, Plane of polarisation in the y direction	$\begin{pmatrix} 0 \\ 1 \end{pmatrix}$
$\vec{E}_{45}$, Plane of polarisation at 45 ° of the x axis direction	$\frac{1}{\sqrt{2}} \begin{pmatrix} 1 \\ 1 \end{pmatrix}$
$\vec{E}_r$, Right-circular polarisation	$\frac{1}{\sqrt{2}} \begin{pmatrix} 1 \\ i \end{pmatrix}$
$\vec{E}_l$, Left-circular polarisation	$\frac{1}{\sqrt{2}} \begin{pmatrix} 1 \\ -i \end{pmatrix}$

As we saw in the first section, linear and circular polarisation are degenerated form of the more general elliptical polarisation. The Jones vector for elliptical polarisation can be written in the condensed form

$$\vec{E} = \begin{pmatrix} cos\theta \\ \pm isin\theta \end{pmatrix}. \tag{6.5}$$

Where θ is the ellipticity angle and $\pm$ correspond to the right and left-handed ellipses.

If two coherent beams propagate in the same z direction, we can simply add their two Jones vectors. Reciprocally, any Jones vector can always be decomposed on a complete orthogonal basis. The vectors $\vec{E}_r$ and $\vec{E}_l$, as the vectors $\vec{E}_h$ and $\vec{E}_v$ form such an orthogonal basis.

$$\vec{E}_r\vec{E}_r^* = \vec{E}_l\vec{E}_l^* = 1, \tag{6.6}$$

$$\vec{E}_r\vec{E}_l^* = \vec{E}_l\vec{E}_r^* = 0, \tag{6.7}$$

$$\vec{E}_h\vec{E}_h^* = \vec{E}_v\vec{E}_v^* = 1, \tag{6.8}$$

$$\vec{E}_h\vec{E}_v^* = \vec{E}_h\vec{E}_v^* = 0. \tag{6.9}$$

In other words, every polarisation state can always be decomposed into the sum of two perpendicular linearly polarised or two circular polarised beams. In Jones formalism, addition of non-coherent beams is not possible.

The Jones matrices The Maxwell equations governing the transverse electric fields are linear equations meaning that the output Jones vector representing the field $\vec{E}_{out}$ is a linear combination of the input Jones vector $\vec{E}_{in}$. That is why any optical element can be modelled by a 2 × 2 matrix acting on the input Jones vector. This matrix is denoted the Jones **M-matrix** [111]

$$M = \begin{pmatrix} a & b \\ c & d \end{pmatrix}. \tag{6.10}$$

a, b, c and d are four complex numbers, making all together eight numerical parameters. Those eight parameters are related to the independent optical properties of any transmitting system. Those are:

- Absorbance (one parameter required)
- Refraction (one parameter required)
- Linear dichroism (LD): The absorption is privileged in one direction (two parameters required, one to define the axis of preferential absorption, another to determine its magnitude)
- Linear birefringence (LB): The refraction is privileged in one direction (two parameters required, one to describe the axis of preferential refraction, another to determine its magnitude)
- Circular dichroism (CD): Left- and right-circular polarised beams are absorbed to different extend (one parameter required, the difference between the imaginary parts of the refraction indexes)
- Circular birefringence (CB): Left- and right-circular polarised beams are refracted to different extend(one parameter required, the difference between the real parts of

the refraction indexes)

The outgoing Jones vector $\vec{E}_{out}$ after the optical element is obtained by matrix multiplication [105]

$$\vec{E}_{out} = M\vec{E}_{in}. \tag{6.11}$$

Operators can be derived for all optical properties separately. The different matrices are defined in Table 6.2 following the notations introduced by Schnellman and Jensen [112, 113]

Table 6.2: Jones matrices for classical polarisation effects (see Table 6.3 for symbol definition

Effect	Jones M-matrix
Phase retardation	$e^{-i\rho L}\begin{pmatrix}1 & 0\\ 0 & 1\end{pmatrix}$
Absorption	$e^{-\kappa L/2}\begin{pmatrix}1 & 0\\ 0 & 1\end{pmatrix}$
Linear dichroism at x-axis	$\begin{pmatrix}e^{-\alpha L/2} & 0\\ 0 & e^{\alpha L/2}\end{pmatrix}$
Linear birefringence at x-axis	$\begin{pmatrix}e^{-i\tau L/2} & 0\\ 0 & e^{i\tau L/2}\end{pmatrix}$
Circular dichroism	$\begin{pmatrix}\cosh\eta L/2 & i\sinh\eta L/2\\ -i\sinh\eta L/2 & \cosh\eta L/2\end{pmatrix}$
Circular birefringence	$\begin{pmatrix}\cosh\delta L/2 & \sinh\delta L/2\\ -\sinh\delta L/2 & \cosh\delta L/2\end{pmatrix}$

If we want to calculate the M-matrix of a linear birefringent (or dichroic) sample which principal axis is no more collinear with the referential axis but rotated by an angle θ, we can simply use the rotation matrix defined as

$$R(\theta) = \begin{pmatrix}\cos\theta & \sin\theta\\ -\sin\theta & \cos\theta\end{pmatrix}. \tag{6.12}$$

and

Table 6.3: Definition of the polarisation effects in terms of absorbances and extinction coefficients. A stands for standard absorbance, n for refractive index, L for path length, λ_0 vacuum wavelength and β is the rotation in degrees. Subscripts $_+$ and $_-$ stands for right- and left-circular polarised light.

Effect	Symbol	Definition	Relation to expt.
Mean refraction index	ρ	$2\pi\cdot$ n $\cdot$ / λ_0	$2\pi\cdot$ n $\cdot$ λ_0
Mean absorbance	κ	$\mathrm{Ln}_{10}(A_x + A_y)/2L$	$\mathrm{Ln}(10)\cdot\varepsilon\cdot c\cdot$
Linear dichroism	α	$\mathrm{Ln}_{10}(A_x - A_y)/2L$	$\mathrm{Ln}(10)\cdot\Delta\varepsilon\cdot c\cdot/2$
Linear birefringence	τ	$2\pi(n_x - n_y)/\lambda_0$	$2\pi\cdot\Delta\varepsilon\cdot/\lambda_0$
Circular dichroism	η	$\mathrm{Ln}_{10}(A_- - A_+)/2L$	$\mathrm{Ln}(10)\cdot\Delta\varepsilon\cdot c\cdot/2$
Circular birefringence	δ	$2\pi(n_- - n_+)/\lambda_0$	$\pi\beta$ /(90L)

$$M_{lb}(\theta) = R(\theta)MR^{-1}(\theta). \tag{6.13}$$

In the case of several cascade elements inserted in the beam (see Figure 6.1 , the output electric field is calculated by multiplying the different matrices representing each elements in the right order [105]

$$\vec{E}_{out} = M_n M_{n-1} \cdots M_0 \vec{E}_{in}. \tag{6.14}$$

N-Matrix technique Problems arise when an optical element exhibits simultaneously several polarisation properties. As an example, a sample can be both linearly birefringent and circular dichroic. Complications appear when the matrices representing the two effects do not commute: The matrix describing the sample depends then on the order of matrices multiplication. Jones has introduced a method to treat the case in which an optical element exhibits several different properties whose matrix do not commute. This method is know as the **N-matrix** technique [105]. The basic idea is that one can divide the element into small slices and evaluate the polarisation of the transmitted light after each consecutive slice using Jones calculus. Each slide is further viewed as composed of sub-slides that individually exhibit the various optical properties of the total element. In the case of a very large number of slices (slices infinitesimally thin), the final result is independent of the order of the sub-slices. The N-matrix or infinitesimal matrix is defined as

$$N = \frac{dM}{dz}M^{-1}. \tag{6.15}$$

Where z is the length of the optics being modelled and M is the classical Jones matrix Using Equation 6.15, a N-matrix can be computed for each coherent polarisation effects previously defined (see Table 6.4).

Table 6.4: N-matrices for different polarisation effects

Effect	Jones N-matrix
Absorption	$\begin{pmatrix} -\kappa/2 & 0 \\ 0 & -\kappa/2 \end{pmatrix}$
Refraction	$\begin{pmatrix} -i\rho & 0 \\ 0 & -i\rho \end{pmatrix}$
Linear dichroism x-axis	$\begin{pmatrix} -\alpha/2 & 0 \\ 0 & \alpha/2 \end{pmatrix}$
Linear birefringence x-axis	$\begin{pmatrix} -i\,\tau/2 & 0 \\ 0 & i\,\tau/2 \end{pmatrix}$
Circular dichroism	$\begin{pmatrix} 0 & -i\,\eta/2 \\ i\,\eta/2 & 0 \end{pmatrix}$
Circular birefringence	$\begin{pmatrix} 0 & -\delta/2 \\ \delta/2 & 0 \end{pmatrix}$

For an element exhibiting several different properties, the total N-matrix is the sum of the N-matrices

$$N_{tot} = N_{lb} + N_{ld} + N_{cd} + \cdots . \tag{6.16}$$

From Equation 6.15, one can re-obtain the total M-matrix with

$$M_{tot} = e^{N_{tot}z}. \tag{6.17}$$

Example As an example, we consider a chiral sample that exhibits circular birefringence (different refraction of left- and right-circular polarised light) and circular dichroism (different absorption of left- and right-circular polarised light). We would like compute the total M-matrix for the two effects. The M matrices for each phenomenon taken separately were described in Table 6.2, they do not commute. We have then to consider the N-matrices for the two phenomena (see Table 6.3). The total N-matrix is the sum of the two sub-matrices

$$N_{cb,cd} = \begin{pmatrix} 0 & -\delta/2 \\ \delta/2 & 0 \end{pmatrix} + \begin{pmatrix} 0 & -i\,\eta/2 \\ i\,\eta/2 & 0 \end{pmatrix} = \begin{pmatrix} 0 & -\delta/2 - i\,\eta/2 \\ \delta/2 + i\,\eta/2 & 0 \end{pmatrix}.$$

Using Equation 6.17, we can calculate the M-matrix

$$M_{cb,cd} = \begin{pmatrix} \cos(\frac{\delta L}{2} - i\frac{\eta L}{4}) & \sin(\frac{\delta L}{2} - i\frac{\eta L}{4}) \\ \\ -\sin(\frac{\delta L}{2} - i\frac{\eta L}{4}) & \cos(\frac{\delta L}{2} - i\frac{\eta L}{4}) \end{pmatrix}. \tag{6.18}$$

Following this method, Jones has computed the general M-matrix containing all the eight optical effects [105]. This matrix, although being complete, is difficult to handle and most of the time simplifications are made depending on the experimental configuration [12, 112].

Conclusions The Jones formalism is a powerful tool to compute polarisation of complex systems. Complicated polarisation calculation reduce to matrix multiplication. The N-matrix technique allows to treat samples exhibiting altogether different polarisation effects. However, Jones formalism restricts to perfectly polarised light and this is a particularly serious limitation as in nature light is very often unpolarised or partially polarised. Depolarising effects cannot be treated within this framework.

The Stokes formalism

In the last section, we saw that light could be represented by a 2-dimensional vector, containing the transverse Maxwell electric fields. The Jones vector representation has a major limitation, it is only applicable to describe light that is perfectly polarised and cannot be used to describe either unpolarised or partially polarised light. In 1852, Sir Gabriel Stokes [106] discovered that polarisation behaviour could be represented in terms of measurable quantities. The Stokes formalism allows to handle unpolarised or partially polarised light.

Stokes vectors The Stokes parameters are defined as [106]

$$s_0 = \langle E_x(t)^2 + E_y(t)^2 \rangle, \tag{6.19}$$

$$s_1 = \langle E_x(t)^2 - E_y(t)^2 \rangle, \tag{6.20}$$

$$s_2 = \langle 2E_x(t)E_y(t) \cos\delta(t) \rangle, \tag{6.21}$$

$$s_3 = \langle 2E_x(t)E_y(t) \sin\delta(t) \rangle. \tag{6.22}$$

Where $E_x(t)$ and $E_y(t)$ are the instantaneous transverse Maxwell electric field components, $\delta(t) = \phi_x(t) - \phi_y(t)$ the instant de-phasing between the two and $\langle \cdots \rangle$ represent time averaged quantities. The four parameters can be rearranged in a column vector: **The Stokes vector**.

$$\vec{S} = \begin{pmatrix} s_0 \\ s_1 \\ s_2 \\ s_3 \end{pmatrix}. \tag{6.23}$$

Unpolarised light In the case of unpolarised light, the electric vector is changing rapidly and erratically with time both in amplitude and absolute phase. In this case, s_0 is the measured total intensity I_0 and the three other parameters average out to zero.

$$\vec{S}(unpolarised) = \begin{pmatrix} I_0 \\ 0 \\ 0 \\ 0 \end{pmatrix}. \tag{6.24}$$

Perfectly polarised light In the case of perfectly polarised light, one Stokes parameter is redundant as

$$s_0^2 = s_1^2 + s_2^2 + s_3^2. \tag{6.25}$$

Equation 6.25 is an equivalent formulation of the ellipse Equation [114]

Partial polarisation The case of partial polarisation can be seen as the sum of some amount of perfectly polarised light plus another amount of unpolarised light [114] and we have

$$s_0^2 \geq s_1^2 + s_2^2 + s_3^2. \tag{6.26}$$

One can define the **degree of polarisation** V as

$$V = \frac{\sqrt{s_1^2 + s_2^2 + s_3^2}}{s_0}. \tag{6.27}$$

The Stokes parameters are real and related to observable quantities [115]. The first parameter is the total intensity of the light, the parameter δ_1 describes the amount of linear horizontal or vertical polarisation, the parameter δ_2 describes the amount of linear +45 ° or -45 ° polarisation and the parameter δ_3 describes the amount of right- or left-circular polarisation contained within the beam.

We can compute the normalized Stokes vectors for some typical pure polarisation states (see Table 6.5)

Table 6.5: Normalized Stokes vectors for some pure polarisation states

State of polarisation	Stokes vectors
$\vec{S}_v$, Plane of polarisation in the x direction	$\begin{pmatrix}1\\-1\\0\\0\end{pmatrix}$
$\vec{S}_h$, Plane of polarisation in the y direction	$\begin{pmatrix}1\\1\\0\\0\end{pmatrix}$
$\vec{S}_{45}$, Plane of polarisation at 45 ° of the x axis direction	$\begin{pmatrix}1\\0\\1\\0\end{pmatrix}$
$\vec{S}_r$, Right-circular polarisation	$\begin{pmatrix}1\\0\\0\\1\end{pmatrix}$
$\vec{S}_l$, Left-circular polarisation	$\begin{pmatrix}1\\0\\0\\-1\end{pmatrix}$

A direct consequence to the fact that Stokes vectors deal with intensities is that if we superimpose two independent beams, we can directly add their Stokes vectors. Stokes formalism allows to describe the superposition of incoherent beams.

Mueller matrices The action of an optical device is to transform the polarisation of a beam from one state to another. A 4 × 4 matrix is the mathematical device to transform one 4 dimensional vector into another to which it is linearly related.

$$\vec{S}_{out} = T\vec{S}_{in}. \tag{6.28}$$

The Matrix T matrix is known as the **Mueller matrix** [111]. It was introduced by Hans Mueller during the early 1940's based on the work of Perrin [116] and Soleillet [117].

Keeping the notations from Schnellman and Jensen [112, 113], we can compute the Mueller matrices for classical polarising elements [112] (see Table 6.5).

Table 6.6: Mueller matrices for classical polarisation effects (see table 6.3 for symbols definition)

Effect	Mueller matrices
Absorption	$e^{-\kappa L}\begin{pmatrix}1&0&0&0\\0&1&0&0\\0&0&1&0\\0&0&0&1\end{pmatrix}$
Linear dichroism at x-axis	$\begin{pmatrix}\cosh\alpha L&0&0&-\sinh\alpha L\\0&1&0&0\\0&0&1&0\\-\sinh\alpha L&0&0&\cosh\alpha L\end{pmatrix}$
Linear birefringence at x-axis	$\begin{pmatrix}1&0&0&0\\0&\cos\tau L&-\sin\tau L&0\\0&\sin\tau L&\cos\tau L&0\\0&0&0&1\end{pmatrix}$
Circular dichroism	$\begin{pmatrix}\cosh\eta L&0&\sinh\eta L&0\\0&1&0&0\\\sinh\eta L&0&\cosh\eta L&0\\0&0&0&1\end{pmatrix}$
Circular birefringence	$\begin{pmatrix}1&0&0&0\\0&\cos\delta L&0&-\sin\delta L\\0&0&1&0\\0&\sin\delta L&0&\cos\delta L\end{pmatrix}$

In the case of several cascade elements inserted in the beam, the output Stokes vector is calculated by multiplying the different matrices representing each elements in the right order

$$\vec{S}_{out} = T_n T_{n-1} \cdots T_0 \vec{S}_{in}. \tag{6.29}$$

Infinitesimal Mueller matrix As for Jones formalism, problems arise when an optical element exhibits simultaneously several polarisation properties. When the matrices representing the two effects do not commute, the matrix describing the sample depends then on the order of matrices multiplication. The same procedure as the Jones N-matrix technique can be used [112,118] to compute microscopic or infinitesimal Mueller matrices (see Table 6.7).

Table 6.7: Infinitesimal Mueller matrices for classical polarisation effects (see table 6.3 for symbols definition)

Effect	Mueller matrices
Absorption	$\kappa L \begin{pmatrix} 1 & 0 & 0 & 0 \\ 0 & 1 & 0 & 0 \\ 0 & 0 & 1 & 0 \\ 0 & 0 & 0 & 1 \end{pmatrix}$
Linear dichroism at x-axis	$\begin{pmatrix} 1 & 0 & 0 & \alpha L \\ 0 & 1 & 0 & 0 \\ 0 & 0 & 1 & 0 \\ \alpha L & 0 & 0 & 1 \end{pmatrix}$
Linear birefringence at x-axis	$\begin{pmatrix} 1 & 0 & 0 & 0 \\ 0 & 1 & \tau L & 0 \\ 0 & -\tau L & 1 & 0 \\ 0 & 0 & 0 & 1 \end{pmatrix}$
Circular dichroism	$\begin{pmatrix} 1 & 0 & -\eta L & 0 \\ 0 & 1 & 0 & 0 \\ -\eta L & 0 & 1 & 0 \\ 0 & 0 & 0 & 1 \end{pmatrix}$
Circular birefringence	$\begin{pmatrix} 1 & 0 & 0 & 0 \\ 0 & 1 & 0 & \delta L \\ 0 & 0 & 1 & 0 \\ 0 & -\delta L & 0 & 1 \end{pmatrix}$

Example The main advantage of Stokes formalism is the ability to deal with partial polarisation. Let's take the example of a polariser. A polariser is nothing else than an extreme linear dichroic (LD) plate. In the Jones formalism, a extreme LD plate inclined by an angle θ is represented by (see Table 6.2).

$$M_{pol} = \begin{pmatrix} \cos^2\theta & \sin\theta\cos\theta \\ \sin\theta\cos\theta & \sin^2\theta \end{pmatrix}. \tag{6.30}$$

This is a perfect polariser in the sense that the extinction ratio is zero. There is no way with Jones matrices to represent a non-perfect polariser as it would lead to partially polarised light. This is not a problem with Mueller matrices. The Mueller matrix for a non perfect polariser is [34]

$$T_{pol} = \frac{t_{max}}{2}\begin{pmatrix} 1+r & (1-r)\cos 2\theta & (1-r)\sin 2\theta & 0 \\ (1-r)\cos 2\theta & (1-\sqrt{r})^2\cos^2 2\theta + 2\sqrt{r} & (1-\sqrt{r})^2\cos 2\theta \sin 2\theta & 0 \\ (1-r)\sin 2\theta & (1-\sqrt{r})^2\cos 2\theta\sin 2\theta & (1-\sqrt{r})^2\sin^2 2\theta + 2\sqrt{r} & 0 \\ 0 & 0 & 0 & 2\sqrt{r} \end{pmatrix}. \tag{6.31}$$

Where t_{max} is the maximum transmission, $r = \frac{t_{min}}{t_{max}}$ is the extinction ratio and θ the angle of inclination.

As for the Jones M matrix, one can compute the general Mueller matrix containing the height optical effects. This produces a rather complex and difficult to grasp matrix. Therefore, it is usually necessary to investigate simplifications [112].

Conclusions Stokes vectors and Mueller matrices constitute a powerful formalism for polarisation calculations. They allow to take into account not only perfectly polarised light like Jones representation but also partially and unpolarised light. Stokes formalism can be applied to solve many different problems in classical physics where polarisation is involved [114].

The matrix of coherency

In this section, we briefly introduce the most recent formalism introduced by Wolf [107]. In this formalism, light polarisation can be fully described by a 2×2 complex matrix called the **coherency matrix**. This matrix is a special occurrence of the general density matrix familiar in quantum mechanics to deal with pure and mixed states. In this analogy, a pure state would correspond to a perfect polarisation as a mixed state would correspond to partial polarisation.

Starting with the two dimensional vector containing the transverse Maxwell electric fields

$$\vec{E} = \begin{pmatrix} E_x(t) = E_{0x}(t)e^{i(-2\pi\overline{\nu}t+\phi_x(t))} \\ E_y(t) = E_{0y}(t)e^{i(-2\pi\overline{\nu}t+\phi_y(t))} \end{pmatrix}. \tag{6.32}$$

We consider the 2×2 matrix defined by

$$C = \begin{pmatrix} \langle E_x E_x^* \rangle & \langle E_x E_y^* \rangle \\ \langle E_y E_x^* \rangle & \langle E_y E_y^* \rangle \end{pmatrix} = \begin{pmatrix} \langle E_{0x}^2 \rangle & \langle E_{0x}E_{0y}e^{i(\phi_x-\phi_y)} \rangle \\ \langle E_{0y}E_{0x}e^{-i(\phi_x-\phi_y)} \rangle & \langle E_{0y}^2 \rangle \end{pmatrix}. \tag{6.33}$$

Where * stands for the complex conjugate and $\langle \cdots \rangle$ are time averaged quantities.

This matrix is hermitian and positive definite [107]. The diagonal elements are real and non-negative, they represent the average intensities of the x and y polarisation components. The off-diagonal elements represent the cross-correlations, they are conjugate to each other. The trace of the matrix represents the average total intensity I of the wave.

Natural light Natural light or completely unpolarised light has the property that the intensity of its components in any direction perpendicular to the propagation is the same and that this intensity is not modified by any de-phasing optical device inserted in the beam. The two off-diagonal elements of the coherency matrix are then null and the diagonal elements are equal and positive.

$$\langle E_x E_x^* \rangle = \langle E_y E_y^* \rangle. \tag{6.34}$$

and

$$\langle E_x E_y^* \rangle = \langle E_y E_x^* \rangle = 0. \tag{6.35}$$

This leads to a coherency matrix for natural light of the form

$$C = \frac{1}{2} I \begin{pmatrix} 1 & 0 \\ 0 & 1 \end{pmatrix}. \tag{6.36}$$

Perfectly polarised light If the light is perfectly polarised, E_{0x}, E_{0y}, ϕ_x et ϕ_y is independent of time and

$$C = \begin{pmatrix} E_{0x}^2 & E_{0x} E_{0y} e^{i\delta} \\ E_{0x} E_{0y} e^{-i\delta} & E_{0y}^2 \end{pmatrix}. \tag{6.37}$$

In this special case, the determinant of the matrix is equal to zero

$$\det\{C\} = 0. \tag{6.38}$$

Examples of coherency matrices for perfectly polarised beams are shown in Table 6.8.

Degree of polarisation We treated the two extreme cases where the light is either unpolarised or perfectly polarised. Partially polarised light can be seen as the sum of a perfectly polarised component C^{pol}, plus a completely unpolarised one C^{unpol} [119]

$$C = C^{pol} + C^{unpol}. \tag{6.39}$$

C^{pol} as we seen before, must have the following form

Table 6.8: Coherency matrix for classical polarisation states

State of polarisation	Coherency matrix
C_v, Plane of polarisation in the x direction	$\frac{1}{2}I\begin{pmatrix}1 & 0\\0 & 0\end{pmatrix}$
C_h, Plane of polarisation in the y direction	$\frac{1}{2}I\begin{pmatrix}0 & 0\\0 & 1\end{pmatrix}$
C_{45}, Plane of polarisation at 45 ° of the x axis direction	$\frac{1}{2}I\begin{pmatrix}1 & 1\\1 & 1\end{pmatrix}$
C_r, Right-circular polarisation	$\frac{1}{2}I\begin{pmatrix}1 & i\\-i & 1\end{pmatrix}$
C_l, Left-circular polarisation	$\frac{1}{2}I\begin{pmatrix}1 & -i\\i & 1\end{pmatrix}$

$$\begin{pmatrix}A & 0\\0 & A\end{pmatrix}. \tag{6.40}$$

with $A \geq 0$

On the other hand, C^{unpol} should be

$$\begin{pmatrix}B & D\\D^* & C\end{pmatrix}. \tag{6.41}$$

with $B, C \geq 0$ and $BC - DD^* = 0$

solving the system

$$\begin{aligned}
&A + B = C_{xx},\\
&A + C = C_{yy},\\
&D = C_{xy},\\
&D^* = C_{yx}.
\end{aligned}$$

gives

$$
\begin{aligned}
A &= \frac{1}{2}(C_{xx} + C_{yy}) - \frac{1}{2}\sqrt{(Tr\{C\})^2 - 4\det\{C\}}, \\
B &= \frac{1}{2}(C_{xx} - C_{yy}) - \frac{1}{2}\sqrt{(Tr\{C\})^2 - 4\det\{C\}}, \\
D &= C_{xy}, \\
D^* &= C_{yx}.
\end{aligned}
$$

The trace of the second matrix represent the total intensity of the polarised part as the trace of the coherency matrix represent the total intensity. The ratio of the two is called the **degree of polarisation** V of the wave

$$V = \frac{I_{pol}}{I_{tot}} = \sqrt{1 - \frac{4\det\{C\}}{Tr\{C\}^2}}. \tag{6.42}$$

For completely polarised light, $V = 1$, for completely unpolarised light $V = 0$ and for partial polarised light $0 \leq V \leq 1$.

Representation of an optical element Calling C_{in} the coherency matrix describing the input beam and C_{out} the output one, any optical element can be represented by a matrix L [119]

$$C_{out} = LC_{in}L^{\dagger}. \tag{6.43}$$

Where † represent the hermitian conjugate. This is the transformation law for the coherency matrix in the quasi-monochromatic approximation. Matrices can be derived for each effects and are identical to the Jones matrices (see Table 6.2). For practical polarisation calculations, Stokes vectors and Mueller matrices are preferred over the coherency formalism. Nonetheless, coherency matrix is useful to bridge the Jones and Stokes representation together as we will see in the next paragraph. The coherency matrix is treated in an elegant manner by Born and Wolf and the reader is referred to their text for further information on this subject [120].

Going from Jones to Stokes representation We present here two approaches. One is due to Parke and consists of going from a two dimensional basis into a four dimensional one taking the direct product [121], the other uses the coherency matrix and its decomposition in terms of Pauli matrices [122].

The Parkes coherency representation basis One way of converting a two-dimensional basis into a four-dimensional one is by taking the direct product. Defining the vector $\vec{P}$

as

$$\vec{P} = \vec{E}^* \otimes \vec{E} = \begin{pmatrix} E_{0x}^2 \\ E_{0x}E_{0y}e^{i\delta} \\ E_{0x}E_{0y}e^{-i\delta} \\ E_{0y}^2 \end{pmatrix}. \tag{6.44}$$

Where $\otimes$ is the direct product and * stands for the complex conjugate. Careful inspection of 6.44 shows that the Stokes parameters can linearly be obtained directly from $\vec{P}$ with

$$\begin{aligned} s_0 &= p_1 + p_4, \\ s_1 &= p_2 + p_3, \\ s_2 &= i(p_3 - p_2), \\ s_3 &= p_1 - p_4. \end{aligned}$$

This gives

$$\vec{S} = A\vec{P}. \tag{6.45}$$

With

$$A = \begin{pmatrix} 1 & 0 & 0 & 1 \\ 0 & 1 & 1 & 0 \\ 0 & -i & i & 0 \\ 1 & 0 & 0 & -1 \end{pmatrix}. \tag{6.46}$$

The relation between the Stokes vector and the Jones vector is then

$$\vec{S} = A(\vec{E}^* \otimes \vec{E}). \tag{6.47}$$

It is also straightforward from 6.47 to compute the relation between Jones matrix, M and Mueller matrix T

$$M = A(T^* \otimes T)A^{-1}. \tag{6.48}$$

Pauli spin matrices Another method to find a relation between Jones vectors and Stokes vectors is to consider the expansion of the coherency matrix in terms of a complete set of 2×2 matrices [122].

The coherency matrix for perfectly polarised light is defined as

$$C = \begin{pmatrix} E_{0x}^2 & E_{0x}E_{0y}e^{i\delta} \\ E_{0x}E_{0y}e^{-i\delta} & E_{0y}^2 \end{pmatrix}. \tag{6.49}$$

We can notice that the parameters of the coherency matrix can be be defined as a function of the Stokes parameters by [110]

$$C = \frac{1}{2}\begin{pmatrix} s_0 + s_1 & s_2 - is_3 \\ s_2 + is_3 & s_0 - s_1 \end{pmatrix}. \tag{6.50}$$

C can be decomposed into 2×2 matrices such

$$C = \frac{1}{2}\sum_{i=0}^{3} \sigma_i s_i. \tag{6.51}$$

with

$$\sigma_0 = \begin{pmatrix} 1 & 0 \\ 0 & 1 \end{pmatrix} \qquad \sigma_2 = \begin{pmatrix} 0 & -i \\ i & 0 \end{pmatrix}$$

$$\sigma_1 = \begin{pmatrix} 0 & 1 \\ 1 & 0 \end{pmatrix}$$

$$\sigma_3 = \begin{pmatrix} 1 & 0 \\ 0 & -1 \end{pmatrix}$$

σ_0 is the identity matrix and σ_1, σ_2, σ_3 are the three Pauli matrices in the usual representation. s_i are the Stokes parameters. This connexion between the matrix of coherency, the Stoke parameters and the Pauli matrices has been first pointed out by Fano [123]. It is surprising to see here the appearance of the Pauli matrices which has been originally introduced in quantum mechanics by Pauli to describe the behaviour of the spin of electrons. Further explanation of the appearance of the Pauli matrices and the vision of the Stokes parameters as a statistical average of the spin vector can be found in [122] and Chapter 9 of the book of Edward O'Neill [119].

From 6.51, one can derive the parameters T_{ij} of the 4×4 Mueller matrices from the 2×2 Jones M matrices

$$T_{ij} = \frac{1}{2}(M\sigma_i M^\dagger \sigma_j). \tag{6.52}$$

Modulation techniques

We briefly present in the next section modulation techniques used to measure CD, CB, LD and LB.

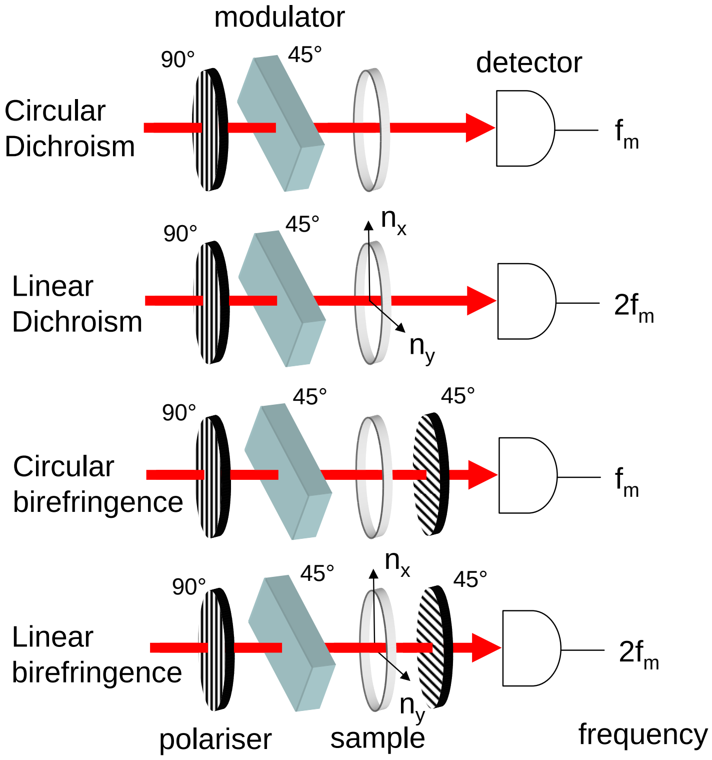

Figure 6.3: Classical arrangements for polarisation spectroscopy. From left to right, the optical elements are the polariser, modulator, optional analyser and the detector. See text for more details.

Optical set-ups usually consist of a first vertical polariser who cleans the input linear polarisation, followed by a modulator whose optical axis is at 45 ° regarding the polariser (see Figure 6.3. The modulator can be an electro-optical cell that use the Pockels effects or a more recent photo elastic modulator (PEM) [30] [1]. The sample, which has to be spatially oriented in case of linear measurements, is placed after the modulator. A second analyser at 45 ° compulsory for circular and linear birefringence measurements, has to be placed after the sample. At the end, a detector records the intensity. The signal is usually filtered to separate the dc and ac components. The ac component is then processed by a lock-in amplifier which essentially measures an average value at the modulation frequency

---

[1] Although a number of polarisation modulators such as Faraday modulators and those involving mechanical rotation of birefringent elements have been used, we only describe here modulators introducing a varying relative phase shift.

f_m for circular dichroism and linear birefringence measurements and twice the modulator frequency $2f_m$ for linear dichroism and circular birefringence. The Jones matrix for the modulator is given by

$$M_{modulator} = \begin{pmatrix} \cos\delta/2 & i\sin\delta/2 \\ i\sin\delta/2 & \cos\delta/2. \end{pmatrix} \tag{6.53}$$

where δ is the instantaneous value of the relative phase shift induced by the modulator for radiation polarised in the direction of its two axis. Using the transformation methods presented previously, the Mueller matrix of the modulator can be calculated as

$$T_{modulator} = \begin{pmatrix} 1 & 0 & 0 & 0 \\ 0 & \cos\delta & 0 & -\sin\delta \\ 0 & 0 & 1 & 0 \\ 0 & \sin\delta & 0 & \cos\delta \end{pmatrix}. \tag{6.54}$$

δ may take the form of any periodic signal used to drive a Pockel cell, whereas acoustic modulator are restricted to sinusoidal form. We consider only sinusoidal signals $\delta = \delta_0 \sin 2\pi f_m t$, where f_m is the modulator frequency and δ_0 the maximal retardation, so that $\cos\delta$ and $\sin\delta$ can be expanded as

$$\sin\delta = 2J_1(\delta_0)\sin f_m t + 2J_3(\delta_0)\sin 3f_m t + \cdots . \tag{6.55}$$

$$\cos\delta = J_0(\delta_0) + 2J_2(\delta_0)\cos 2f_m t + 2J_4(\delta_0)\cos 4f_m t + \cdots . \tag{6.56}$$

Where J_n are the Bessel function of the first kind. If we calculate using Jones formalism the intensity falling on the detector in the first arrangement of Figure 6.3, supposing that the sample can be represented by the chiral matrix of Equation 6.18, one get

$$I_d = \cosh\eta L/2 + \sinh\eta L/2(\sin(\delta_0 \sin f_m t)). \tag{6.57}$$

Taking the ratio of the ac component at f_m and the dc gives

$$\frac{I_{ac}}{I_{dc}} = 2J_1(\delta_0)\tanh(\eta L/2)\sin f_m t. \tag{6.58}$$

Measuring the ratio of $\frac{I_{ac}}{I_{dc}}$ at f_m yields to the circular dichroism parameter η. Similar calculations allow to retrieve circular birefringence, linear dichroism and birefringence.

The Jones matrices parameters and linear response functions

The purpose of this appendix is to outline the connection between the Jones matrices calculus describe in appendix 1 and the linear response theory. We express the complex Jones matrices parameters in term of magnetic and electric transition dipole moments. Let us start with the light-matter coupling Hamiltonian. As we saw in Chapter 1, in order to describe circular dichroism and optical rotation phenomena, the light-matter coupling Hamiltonian H' must be expanded beyond the linear dipole approximation to next higher order in the spatial dependence of the electromagnetic field $\exp[i\vec{k}\cdot\vec{r}]$. The additional terms can be collected in magnetic dipole - magnetic field and electric quadrupole - electric field interactions (see Chapter 1):

$$\hat{\mathcal{H}}_{int} = -\hat{p}\cdot\vec{E} - \hat{m}\cdot\vec{H} - \sum \hat{Q}_{pq}\nabla_q E_p. \tag{6.59}$$

Averaging over an isotropic sample eliminates electric quadrupole contributions to the linear polarisation and the only remaining terms are [95]

$$\begin{aligned} P_x(t) &= -\int_0^\infty S_{xx}^{pp}(t')E_x(t-t')dt' \\ &\quad + \int_0^\infty S_{xx}^{mp}(t')E_y(t-t')dt', \\ P_y(t) &= -\int_0^\infty S_{yy}^{pp}(t')E_y(t-t')dt' \\ &\quad - \int_0^\infty S_{yy}^{mp}(t')E_x(t-t')dt'. \end{aligned} \tag{6.60}$$

with the orientationally averaged linear response functions

$$\begin{aligned} S_{kk}^{pp}(t) &= \frac{i}{\hbar}\langle[\hat{p}_k(t),\hat{p}_k(0)]\rho_0\rangle \\ ,S_{kk}^{mp}(t) &= \frac{i}{\hbar}\left(\langle[\hat{p}_k(t),\hat{m}_k(0)]\rho_0\rangle - \langle[\hat{m}_k(t),\hat{p}_k(0)]\rho_0\rangle\right) \\ &. \end{aligned} \tag{6.61}$$

The opposite signs of the second integral terms in Equation 6.60 can be regarded as a consequence of the fact that, with $\vec{H} = \hat{k}\times\vec{E}$, a wave propagating in the z-direction has its magnetic field vector pointing into the $+y$ and $-x$ direction when the electric field vector points into $+x$ and $+y$ direction, respectively.

For better clarity we assume that the system is initially in the ground state and consider a single, isolated homogeneously broadened transition with frequency ω_j. In this case, the bath degrees of freedom in the ensemble average $\langle\dots\rangle$ in Equation 6.61 contribute a common dephasing factor $\exp[-\Gamma t]$, while the traces over the molecular eigenstates yield

$$\begin{aligned} & \langle[\hat{p}_k(t), \hat{p}_k(0)]\rho_0\rangle_{mol} = \frac{1}{3}\langle[\hat{p}(t), \hat{p}(0)]\rho_0\rangle_{mol} \qquad (6.62) \\ = & \frac{1}{3}\vec{p}_{0j}\vec{p}_{j0}(e^{-i\omega_j t} - e^{i\omega_j t}) = \frac{1}{3}|\vec{p}_{0j}|^2(e^{-i\omega_j t} - e^{i\omega_j t}) \end{aligned}$$

and

$$\begin{aligned} & \langle[\hat{p}(t), \hat{m}(0)]\rho_0\rangle_{mol} - \langle[\hat{m}(t), \hat{p}(0)]\rho_0\rangle_{mol} \qquad (6.63) \\ = & (\vec{p}_{0j}\vec{m}_{j0} - \vec{m}_{0j}\vec{p}_{j0})e^{-i\omega_j t} + (\vec{p}_{0j}\vec{m}_{j0} - \vec{m}_{0j}\vec{p}_{j0})e^{i\omega_j t} \\ = & 2iIm[\vec{p}_{0j}\vec{m}_{j0}](e^{-i\omega_j t} + e^{i\omega_j t}) \end{aligned}$$

(where $\vec{p}_{j0} = \langle j|\hat{p}|0\rangle = \vec{p}^{*}_{0j}$ and $\vec{m}_{j0} = \langle j|\hat{m}|0\rangle$ stand for the electric and magnetic $0 \rightarrow j$ transition dipole moments). As a result, the chiral part of the linear polarisation is not only perpendicular to the achiral linear polarisation but also phase-shifted by $\pi/2$.

Fourier transformation converts convolution integrals in the time domain to simple products in the frequency domain yielding Equations 6.60 in matrix form

$$\begin{aligned} \vec{P}(\omega) &= -\frac{1}{3}\chi(\omega) \times \qquad (6.64) \\ & \begin{pmatrix} |\vec{p}_{0j}|^2 & -2iIm[\vec{p}^{*}_{0j}\vec{m}_{0j}] \\ 2iIm[\vec{p}^{*}_{0j}\vec{m}_{0j}] & |\vec{p}_{0j}|^2 \end{pmatrix} \vec{E}(\omega) \end{aligned}$$

with the complex lineshape function (near resonance)

$$\begin{aligned} \chi(\omega) &= \frac{i}{\hbar}\int_0^\infty e^{-\Gamma t}e^{-i\omega_j t}e^{i\omega t} \\ &= \frac{1}{\hbar}\left(\frac{(\omega - \omega_j)}{\Gamma^2 + (\omega - \omega_j)^2} + i\frac{\Gamma}{\Gamma^2 + (\omega - \omega_j)^2}\right) \\ &= : \chi' + i\chi''. \qquad (6.65) \end{aligned}$$

The connection with the Jones matrix formalism is established by finding the electric field after the sample, which is a solution of the Maxwell equation (c_0 = speed of light)

$$\nabla \times \nabla \times \vec{E}(r,t) - \frac{1}{c_0^2}\frac{\partial^2}{\partial t^2}\vec{E}(r,t) = \frac{1}{c_0^2}\frac{\partial^2}{\partial t^2}\vec{P}(r,t). \qquad (6.66)$$

In the treatment of linear absorption and dispersion, this equation is usually solved self-consistently for the total electric field in space and time. However, if we consider only a sufficiently thin slice of sample, the difference between the field before and after matter interaction is very small, and the polarisation $\vec{P}(r,t)$ to lowest order only depends on the incoming electric field $\vec{E}_{in}$. Left and right hand side of Equation 6.66 are then decoupled, oscillatory terms can be eliminated and the remaining differential equation for the plane wave envelope functions $\vec{P}_0$ and $\vec{E}_0$ is greatly simplified by the slowly varying amplitude approximation [124] (time-derivatives of $\vec{P}_0$ and $\vec{E}_0$ are dropped because these envelope functions vary slowly with respect to the light field oscillations). The final equation

$$\frac{\partial \vec{E}_0}{\partial z} = -i\frac{\omega}{2c_0}\vec{P}_0(t) \tag{6.67}$$

leads to the well-known result that the field after a thin layer δz of sample is simply the sum of the incoming field plus the linear polarisation with a $\pi/2$ phase lag

$$\vec{E}_{out} = \vec{E}_{in} - i\frac{\omega}{2c_0}\delta z\vec{P} \tag{6.68}$$

Using the sample parameters we can now write

$$\begin{aligned} \vec{E}_{out} &= [1 + \delta z\frac{\omega}{6c_0}\chi(\omega) \\ &\times \begin{pmatrix} i|\vec{p}_{0j}|^2 & 2Im[\vec{p}^*_{0j}\vec{m}_{0j}] \\ -2Im[\vec{p}^*_{0j}\vec{m}_{0j}] & i|\vec{p}_{0j}|^2 \end{pmatrix}]\vec{E}_{in} \end{aligned} \tag{6.69}$$

In the Jones matrix formalism the electric field behind an infinitesimally thin chiral sample is described by

$$\vec{E}_{out} = (1 + N\delta z)\vec{E}_{in} \tag{6.70}$$

where N is the infinitesimal Jones matrix

$$N = \begin{pmatrix} \frac{-\kappa}{2} - i\,\rho & \frac{\delta}{2} - \frac{i}{4}\,\eta \\ -\frac{\delta}{2} + \frac{i}{4}\,\eta & \frac{-\kappa}{2} - i\,\rho \end{pmatrix} \tag{6.71}$$

from which the Jones matrix for a sample of thickness L is recovered via

$$M = \lim_{n\to\infty}(1 + \frac{L}{n}N)^n = e^{NL} \tag{6.72}$$

We can thus identify

$$N = const \times \omega\chi(\omega) \begin{pmatrix} i|\vec{p}_{0j}|^2 & 2Im[\vec{p}^*_{0j}\vec{m}_{0j}] \\ -2Im[\vec{p}^*_{0j}\vec{m}_{0j}] & i|\vec{p}_{0j}|^2 \end{pmatrix} \tag{6.73}$$

The constant contains only real quantities such as the number of molecules per area. We may include the term $\omega\chi(\omega)$ in a new lineshape function $\tilde{\chi}$ whose imaginary part is normalized such that $\tilde{\chi}''(\omega_j) = 1$. We thus obtain the useful result

$$\begin{aligned}
\text{absorption: } \kappa &= \epsilon c \ln(10) \tilde{\chi}''(\omega) && (6.74) \\
\text{dispersion: } \rho &= \frac{\epsilon c}{2} \ln(10) \tilde{\chi}'(\omega) && (6.75) \\
\text{circular dichroism: } \eta &= \Delta\epsilon c \ln(10) \tilde{\chi}''(\omega) && (6.76) \\
\text{optical rotation: } \delta &= -\frac{\Delta\epsilon c}{2} \ln(10) \tilde{\chi}'(\omega) && (6.77)
\end{aligned}$$

where c is the concentration, ϵ is the decadic molar extinction coefficient of the transition and $\Delta\epsilon = \epsilon_L - \epsilon_R = \frac{4Im[p \cdot m]}{|p|^2}\epsilon$.

Multiple bands can be described by summing over individual transitions, while different lineshapes and signals far from resonance can be taken into account by a more sophisticated evaluation of the linear response functions.

Bibliography

[1] C. Rulliere. *Femtosecond laser pulses: Principles and experiments.* Springer, 2004.

[2] H. Zewail. Femtochemistry: Atomic-scale dynamics of the chemical bond using ultra-fast lasers. *Angewandte Chemie International Edition*, 39:2586–2631, 2000.

[3] E. T. J. Nibbering, H. Fidder and E. Pines. Ultra-fast chemistry: using time-resolved vibrational spectroscopy for interrogation of structural dynamics. *Annual Review of Physical Chemistry*, 56:337–367, 2005.

[4] M. Khalili, M. Demirdroeven and A. Tokmakoff. Coherent 2D-IR spectroscopy: Molecular structure and dynamics in solution. *Journal of Physical Chemistry*, 107:5258–5279, 2003.

[5] M. Kozinski, S. Garrett-Roe and P. Hamm. 2D-IR spectroscopy of the sulfhydryl band of cysteines in the hydrophobic core of proteins. *Journal of Physical Chemistry B*, 112:425–463, 2008.

[6] J. Bredenbeck and P. Hamm. Transient 2D-IR spectroscopy: Towards a molecular movie. *Chimia*, 61:45–46, 2007.

[7] L. A. Nafie. Circular polarization spectroscopy of chiral molecules. *Journal of Molecular Structure*, 347:83–100, 1995.

[8] F. Arago. Mémoire sur une modification remarquable qu'éprouvent les rayons lumineux dans leur passage à travers certains corps diaphanes et sur quelques autres nouveaux phénomenes d'optique. *Mémoires de la classe des sciences mathématiques et physiques de l'institut imperial de France*, 93:313–316, 1811.

[9] C. Djerassi. *Optical rotatory dispersion.* Mc Graw-Hill book company, 1960.

[10] P. L. Polavarapu. Optical rotation: Recent advances in determining the absolute configuration. *Chirality*, 14:768–781, 2002.

[11] R. W. Woody. *Theory of circular dichroism of proteins. In Circular dichroism and the conformational analysis of biomolecules.* Plenum press, 1996.

[12] X. Xie and J. D. Simon. Picosecond circular dichroism spectroscopy - A Jones matrix analysis. *Journal of Optical Society of America B*, 7:1673–1684, 1990.

[13] X. Xie and J. D. Simon. Picosecond time-resolved circular dichroism spectroscopy: Experimental details and applications. *Review of Scientific Instrumentation*, 60:2614–2627, 1989.

[14] D. B. Shapiro, R. A. Goldbeck, D. P. Che, R. M. Esquera, S. J. Paquette and D. S. Kliger. Nanosecond optical-rotatory dispersion spectroscopy - application to photolyzed hemoglobin-CO kinetics. *Biophysical Journal*, 68:326–334, 1995.

[15] E. F. Chen, J. R. Kumita, G. A. Woolley and D. S. Kliger. The kinetics of helix unfolding of an azobenzene cross-linked peptide probed by nanosecond time-resolved optical rotatory dispersion. *Journal of Chemical Society of America*, 125:12443–12449, 2003.

[16] T. Dartigalongue and F. Hache. Observation of sub-100 ps conformational changes in photolyzed carbonmonoxy-myoglobin probed by time-resolved circular dichroism. *Chemical Physics*, 415:313–316, 2005.

[17] T. A. Keiderling. *Practical Fourier transform infrared spectroscopy*, chapter Vibrational circular dichroism: Comparison of techniques and practical considerations. Academic press Inc., 1990.

[18] J. R. Roy L. A. Nafie, F. J. Long, T. B. Freedman, H. Buijs, A. Rilling and R. K. Dukor. The determination of enantiomeric purity and absolute configuration by vibrational circular dichroism spectroscopy. In J. A. de Haseth, editor, *Fourier transform spectroscopy*, volume 430, pages 432–434, 1998.

[19] T. B. Freedman, X. Cao, R. K. Dukor and L. A. Nafie. Absolute configuration determination of chiral molecules in the solution state using vibrational circular dichroism. *Chirality*, 15:743–758, 2003.

[20] Site specific conformational determination in thermal unfolding studies of helical peptides using vibrational circular dichroism with isotopic substitution. *Proceedings of the National Academy of Science of America*, 97.

[21] J. Kubelka and T. A. Keiderling. Differentiation of β sheets forming structures: Ab initio based simulations of IR absorption and vibrational CD for model peptide and protein β sheets. *Journal of the American Chemical Society*, 123:12048–12058, 2001.

[22] P. Bour, J. Kubelka and T. K. Keiderling. Ab initio quantum mechanical models of peptide helices and their vibrational spectra. *Biopolymers*, 65:45–59, 2002.

[23] C. J. Barnett, A. F. Drake, R. Kuroda, S. F. Mason and S. Savage. Vibrational electronic interaction in the infrared circular dichroism spectra of transition-metal complexes. *Chemical Physics Letters*, 70:8–10, 1980.

[24] Y. N. He, X. L. Cao, L. A. Nafie and T. B. Freedman. Ab initio VCD, calculation of a transition-metal containing molecule and a new intensity enhancement mechanism for VCD. *Journal of the American Chemical Society*, 123:11320–11321, 2001.

[25] L. A. Nafie. Theory of vibrational circular dichroism and infrared absorption: Extension to molecules with low-lying excited electronic states. *Journal of Physical Chemistry A*, 35:7222–7231, 2004.

[26] J. T. Wrobleski and G. J. Long. Alkaloids as ligands. 1. synthesis and characterization of three cobalt(II) pseudohalide compounds containing l-sparteine. *Inorganic Chemistry*, 16:704–709, 1977.

[27] P. Xie and M. Diem. Measurement of dispersive vibrational circular dichroism: Signal optimization and artefacts reduction. *Applied Spectroscopy*, 5:675–680, 1996.

[28] T. Dartigalongue and F. Hache. Precise alignment of a longitudinal pockels cell for time-resolved circular dichroism experiments. *Journal of Optical Society of America B*, 20:1780–1787, 2003.

[29] B. B. Wang. PEM-based VCD spectroscopy. Technical report, Hinds Instruments.

[30] J. C. Kemp. Piezo-optical birefringence modulators: New use for a long-known effect. *Journal of the Optical Society of America*, 59:950–954, 1969.

[31] D. Jonas. Two dimensional femtosecond spectroscopy. *Annual Review of Physical Chemistry*, 54:425–463, 2003.

[32] H.Rhee, Y. G. June, J. S. Lee, K. K. Lee, J. H. Ha, Z. H. Kim, S. J. Jeon and M. Cho. Femtosecond characterization of vibrational optical activity of chiral molecules. *Nature*, 458:310–313, 2009.

[33] J. Lewis, R. F. Tilton, C. M. Einterz, S. J. Milder, I. D. Kuntz, D. S. Kliger. New technique for measuring circular dichroism changes on a nanosecond time scale. application to (carbonmonoxy)myoglobin and (carbonmonoxy)hemoglobin. *Journal of Physical Chemistry*, 89:289–294, 1985.

[34] D. Che, D. Shapiro, R. Esquerra and D. Kliger. Ultrasensitive time-resolved linear dichroism spectral measurements using near crossed linear polarizers. *Chemical Physics Letters*, 224:145–154, 1994.

[35] L. D. Barron. Chirality and life. *Space Science Reviews*, 135:187–201, 2008.

[36] H. G. Brittain. Techniques of chiroptical spectroscopy. *Applied Spectroscopy Reviews*, 35:175–201, 2000.

[37] D. H. Turner, J. I. Tinoco and M. Maestre. Fluorescence detected circular dichroism. *Journal of American Chemical Society*, 96:4340–4342, 1974.

[38] F. S. Richardson and J. P. Riehl. Circularly polarized luminescence spectroscopy. *Chemical Review*, 77:773–792, 1977.

[39] L. D. Barron and J. Vrbancich. Natural vibrational raman optical activity. *Topics in Current Chemistry*, 123:151–182, 1984.

[40] J. B. Biot. Mémoire sur la polarisation circulaire et sur ses applications à la chimie organique. *Mémoires de l'Académie des Sciences de l'Institut de France*, 13:39–175, 1835.

[41] A. Fresnel. Mémoire sur les couleurs développées dans les fluides homogènes. *Mémoires de l'Académie des Sciences de l'Institut de France*, 20:163–194, 1849.

[42] T. Ruchon. *Magnetochiral interaction: Theoretical study and experiments in lasers.* PhD thesis, university of Rennes I, France, 2005.

[43] A. Cotton. Absorption et dispersion de la lumière par les milieux doués du pouvoir rotatoire. *Journal de Physique Théorique Appliquée*, 51:290–302, 1896.

[44] E. U. Condon. Theories of optical rotatory power. *Reviews of Modern Physics*, 9:432–457, 1937.

[45] J. C. Maxwell. *A treatise on electricity and magnetism.* Dover publications, 1954.

[46] P. Drude. *The theory of optics.* Dover Publications, 1959.

[47] F. I. Fedorov. On the theroy of optical activity in crystals. i. the law of conservation of energy and the optical activity tensors. *Optics and Spectroscopy*, 6:49–53, 1959.

[48] L. Rosenfeld. Quantenmechanische Theorie der natuerlichen optischen Aktivitaet von Fluessigkeiten und Gasen. *Zeitschrift fuer Physik*, 52:161–174, 1928.

[49] E. Hecht. *Optics.* Addison Wesley Publishing Company, 2005.

[50] I. Tinoco and M. P. Freeman. The optical activity of oriented copper helices. *Journal of Physical Chemistry*, 61:1196–1200, 1957.

[51] F. Gray. The optical activity of liquids and gases. *Physical Review*, 7:472–488, 1916.

[52] S. F. Boys. Optical rotatory power. (I) a theoritical calculation for a molecule containing only isotropic refractive centres. *Proceedings of the Royal Society of London*, 144:655–675, 1934.

[53] W. Kuhn. The physical significance of optical rotatory power. *Transaction of the Faraday Society*, 26:293–308, 1930.

[54] J. L. Mc Hale. *Molecular spectroscopy.* Prentice hall, 1999.

[55] E. Charney. *The molecular basis of optical activity.* Wiley-Interscience publication, 1979.

[56] B. Schrader and E. H. Korte. Infrared rotatory dispersion (IRD). *Angewandte Chemie international Edition*, 11:226–227, 1972.

[57] S. F. Mason R. J. Dudley, and R. D. Peacock. Infrared vibrational circular dichroism. *Journal of the Chemical Society*, 19:1084–1085, 1972.

[58] I. Chabay. Absorptive and scattering circular dichroism of cholesteric liquid crystals in infrared. *Chemical Physics Letters*, 17:283–287, 1972.

[59] I. Chabay, E. C. Hsu and G. Holzwarth. Infrared circular dichroism measurement between 2000 and 5000 cm-1: Pr3+-tartrate complexes. *Chemical Physics Letters*, 15:211–214, 1972.

[60] G. Holzwarth, E. C. Hsu, H. S. Mosher, T. R. Faulkner and A. Moscowitz. Infrared circular dichroism of carbon-hydrogen and carbon-deuterium stretching modes. Observations. *Journal of the American Chemical Society*, 96:251–252, 1974.

[61] L. A. Nafie, T. A. Keiderling and P. J. Stephens. Vibrational circular dichroism. *Journal of the American Chemical Society*, 98:2715–2723, 1976.

[62] M. Urbanova, V. Setnicha and K. Volka. Measurements of concentration dependence and enantiomeric purity of terpene solutions as a test of new commercial vcd spectrometer. *Chirality*, 12:199–203, 2000.

[63] O. McConnell, A. Bach, C. Balibar, N. Byrne, Y. Cai, G. Carter, M. Chlenov, L. Di, K. Fan, I. Golje, Y. He, D. Herold, M. Kagan, E. Kerns, F.Koehn., C. Kraml, V. Marathias, B. Marquez, L. McDonald, L. Nogle, C. Petucci, G.Schlingmann, G. Tawa, M. Tischler, R. T. Williamson, A. Sutherland, W.Watts, M. Young, M. Y. Zhang, Y.Zhang, D. Zhou, D. Ho. Enantiomeric separation and determination of absolute stereochemistry of asymmetric molecules in drug discovery - building chiral technology toolboxes. *Chirality*, 19:658–682, 2007.

[64] T. Taniguchi, N. Miuria, S. I. Nishimura and K. Monde. Vibrational circular dichroism: Chiroptical analysis of biomolecules. *Molecular Nutrition and Food Research*, 48:246–254, 2004.

[65] T. B. Freedman, R. K. Dukor, P. J. C. M. van Hoof, E. R. Kellenbach and L. A. Nafie. Determination of the absolute configuration of (-)-mirtazapine by vibrational circular dichroism. *Helvetica Chimica Acta*, 85:1160–1116, 2002.

[66] T. A. Keiderling. *Circular dichroism and the conformational analysis of biomolecules*, chapter 16 Vibrational circular dichroism: application to conformational analysis of biomolecules, pages 555–598. Plenum press, 1996.

[67] T. A. Keiderling. Protein and peptide secondary structure and conformational determination with vibrational circular dichroism. *Current Opinions in Chemical Biology*, 6:682–688, 2002.

[68] P. K. Bose and P. L. Polavarapu. Vibrational circular dichroism is a sensitive probe of the glycosidic linkage; oligosaccharides of glucose. *Journal of American Chemical Society*, 121:6094–6095, 1999.

[69] M. Grosjean and M. Legrand. Appareil de mesure du dichroism circulaire dans le visible et l'ultraviolet. *Comptes rendus hebdomadaires des séances de l'académie des sciences*, 251:2150–2152, 1960.

[70] L. A. Nafie, M. Diem and D. W. Vidrine. Fourier-transform infrared vibrational circular dichroism. *Journal of the American Chemical Society*, 101:496–498, 1979.

[71] A. Lakhani, P. Malon and T. A. Keiderling. Comparison of vibrational circular dichroism instruments: Development of a new dispersive VCD. *Journal of Applied Spectroscopy*, 63:775–785, 2009.

[72] P. Malon and T. A. Keiderling. A solution to the artefact problem in fourier transform vibrational circular dichroism. *Journal of Applied Spectroscopy*, 42:32–38, 1988.

[73] C. N. Su and T. A. Keiderling. Conformation of dimethyl tartrate in solution. vibrational circular dichroism results. *Journal of the American Chemical Society*, 102:511–515, 1980.

[74] M. Diem, G. M. Roberts, O. Lee and A. Barlow. Design and performance of an optimized dispersive infrared dichrograph. *Applied Spectroscopy*, 42:20–27, 1988.

[75] G. R. Bird and M. Parrish. The wire grid as a near-infrared polarizer. *Journal of the Optical Society of America*, 50:886–891, 1960.

[76] T. J. Bridges and J. W. Kluver. Dichroic calcite polarizers for infrared. *Applied Optics*, 4:1121–1125, 1965.

[77] D. J. Dummer, S. G. Kaplan, L. M. Hanssen, A. S. Pine and Y. Zong. High-quality brewster's angle polarizer for broadband infrared application. *Applied Optics*, 37:1194–1204, 1998.

[78] B. B. Wang. Useful aperture. Technical report, Hinds Instruments.

[79] A. Rogalski. HgCdTe infrared detector material: history, status and outlook. *Reports on Progress in Physics*, 68:2267–2336, 2005.

[80] E. Theocharous, J. Ishii and N. P. Fox. Absolute linearity measurements on HgCdTe detectors in the infared region. *Applied Optics*, 43:4182–4188, 2004.

[81] P. Hamm, R. A. Kaindl and J. Stenger. Noise suppression in femtosecond mid-infrared light sources. *Optics Letters*, 25:1798–1800, 2000.

[82] G. Cerullo, M. Nisoli, S. Stagira and S. De silveri. Sub-8-fs pulses from an ultra broad optical parametric amplifier in the visible. *Optics Letters*, 23:1283–1285, 1998.

[83] T. Wilhem, J. Piel and E. Riedle. Sub-20-fs pulses across the visible from a blue pumped single-pass noncollinear parametric converter. *Optics Letters*, 22:1494–1496, 1997.

[84] E. Riedle, M. Beutter, S. Lochbrunner, J. Piel, S. Spoerlein and W. Zinth. Generation of 10 to 50fs pulses tunable through all the visible and the NIR. *Applied Physics B*, 71:457–465, 2000.

[85] J. Bredenbeck and P. Hamm. Versatile small volume closed-cycle flow cell system for transient spectroscopy at high repetition rates. *Review of Scientific Instrumentation*, 74:3188–3189, 2003.

[86] E. D. Lipp, C. G. Zimba, L. A. Nafie and D. W. Vidrine. Polarization demodulation - A new approach to the reduction of polarization artefacts from vibrational circular dichroism spectra. *Applied Spectroscopy*, 5:496–498, 1982.

[87] K. Rahmelow. Electronic influences on an infrared detector signal: Non-linearity and amplification. *Applied Spectroscopy*, 36:2123–2132, 1997.

[88] M. S. Alam and J. Predina. Identification and estimation of nonlinearity in constant-voltage-biased infrared sensor detected signals. *Optical Engineering*, 39:3264–3271, 2000.

[89] O. Abe, K. Kawasaki and M. Wakaki. Improvement of nonlinearity and extension of wavelength region using tandem (PV+PC) type HgCdTe detector (dual-MCT) in FTIR spectrometer. *Journal of Electronic Materials*, 28:3264–3271, 1999.

[90] J. C. Cheng, L. A. Nafie and P. J. Stephens. Polarization scrambling using a photoelastic modulator: Application to circular dichroism measurement. *Journal of the Optical Society of America*, 65:1031, 1975.

[91] X. Cao, R. Dukor and L. Nafie. Reduction of linear birefringence in vibrational circular dichroism measurement: use of a rotating half-wave plate. *Theoretical Chemistry Accounts: Theory, Computation, and Modeling (Theoretica Chimica Acta)*, 119:69–79, 2008.

[92] J. Badoz, M. P. Silverman and J. C. Canit. Wave propagation through a medium with static and dynamic birefringence - theory of the photo elastic modulator. *Journal of the Optical Society of America A*, 4:672–682, 1990.

[93] J. Bredenbeck, J. Helbing, C. Renner, R. Behrendt, L. Moroder, J. Wachtveitl and P. Hamm. Transient 2D-IR spectroscopy: Snapshots of the nonequilibrium ensemble during the picosecond conformational transition of a small peptide. *Journal of Physical Chemistry*, 107:8654–8660, 2003.

[94] B. Jasiewiez, E. Sikorska, I. V. Khmelinskii, B. Warzajtis, U. Rychlewska, W. Boczon and M. Sikorski. Spectroscopy and structure of sparteine and 2-methylsparteine dichloride metal complexes. *Journal of Molecular Structure*, 707:89–96, 2004.

[95] H. Rhee, J. H. Ha, S. J. Jeon and M. Cho. Femtosecond spectral interferometry of optical activity: Theory. *Journal of Chemical Physics*, 129:094507, 2008.

[96] R. Schweitzer-Stenner, F. Eker, K. Griebenow, X. Cao and L. A. Nafie. The conformation of tetra-alanine in water determination by polarized raman, FT-IR and VCD spectroscopy. *Journal of American Chemical Society*, 126:2768–2776, 2004.

[97] W. Xiong and M. T. Zanni. Signal enhancement and background cancellation in collinear two-dimensional spectroscopies. *Optics Letters*, 33:1371–1373, 2008.

[98] E. F. Chen and C. Strauss. Nanosecond laser temperature-jump optical rotatory dispersion: Application to early events in protein folding/unfolding. *Review of Scientific Instruments*, 76, 2005.

[99] L. Lepetit, G. Chriaux and M. Joffre. Linear techniques of phase measurement by femtosecond spectral interferometry for applications in spectroscopy. *Journal of Optical Society of America B*, 12:2467–2474, 1995.

[100] R. W. Bormett, G. D. Smith, S. A. Asher, D. Barrick and D. M. kurtz Jr. Vibrational circular dichroism measurements of ligand vibrations in haem and non-haem metalloenzymes. *Faraday Discussions*, 99:327–339, 1994.

[101] H. Rhee, Y. June, Z. H. Kim, S. Jeon and M. Cho. Phase sensitive detection of vibrational optical activity free-induction-decay: vibrational CD and ORD. *Journal of the Optical Society of America B*, 26:1008–1017, 2009.

[102] C. Niezborala and F. Hache. Measuring the dynamics of circular dichroism in a pump-probe experiment with a babinet-soleil compensator. *Journal of the Optical Society of America B*, 23:2418–2424, 2006.

[103] H. S. Chung, Z. Ganim, K. C. Jones and A. Tokmakoff. Transient 2D-IR spectroscopy of ubiquitin unfolding dynamics. *Proceedings of the National Academy of Science of America*, 104:14237–14242, 2007.

[104] H. S. Chung, M. Khalil, A. W. Smith and A. Tokmakoff. Transient two-dimensional IR spectrometer for probing nanosecond temperature-jump kinetics. *Review of Scientific Instruments*, 78:063101, 2007.

[105] R. C. Jones. A new calculus for the treatment of optical systems. *Journal of Optical Society of America*, 31:488–493, 1941.

[106] G. G. Stokes. On the composition and resolution of streams of polarized light from different sources. *Transaction of the Cambridge Philosophical Society*, 9:399, 1819.

[107] E Wolf. Optics in terms of observable quantities. *Nuovo cimento*, 12:884–888, 1954.

[108] M. R. Dennis. Geometric interpretation of the three-dimensional coherence matrix for nonparaxial polarization. *Journal of Optics A: pure and applied optics*, 6:26–31, 2004.

[109] P. Roman. Generalized stokes parameters for waves with arbitrary form. *Nuovo cimento*, 13(5):974–982, 1959.

[110] D. Goldstein. *Polarized light*. Marcel Dekker, 2003.

[111] M. J. Walker. Matrix calculus and the stokes parameters of polarized radiation. *American Journal of Physics*, 22:170–174, 1954.

[112] H. P. Jensen, J. A. Schnellman and T. Troxell. Modulation techniques in polarization spectroscopy. *Applied Spectroscopy*, 32:192–200, 1978.

[113] J. Schnellman and H. P. Jensen. Optical spectroscopy of oriented molecules. *Chemical review*, 87:1359–1399, 1987.

[114] E. Collett. Description of polarization in classical physics. *American Journal of Physics*, 36:713–725, 1968.

[115] E. Hecht. Note on an operational definition of the stokes parameters. *American Journal of Physics*, 38:1156–1158, 1970.

[116] F. Perrin. Polarization of light scattered by isotropic opalescent media. *Journal of Chemical Physics*, 10:415–425, 1942.

[117] P. Soelillet. The parameters which characterize the partial polarization of light in the phenomena of fluorescence. *Annales de Physique*, 12:23–97, 1929.

[118] T. C. Troxell and H. A. Scheraga. Electric dichroism and polymer conformation. i. theory of optical properties of anisotropic media, and method of measurement. *Macromolecules*, 4:519–527, 1971.

[119] E. L. O'Neill. *Introduction to Statistical Optics.* Dover Publications, 1992.

[120] M. Born and E. Wolf. *Principles of Optics: Electromagnetic Theory of Propagation, Interference and Diffraction of Light.* Cambridge University Press, 1999.

[121] N. G. Parke. Optical algebra. *Journal of Mathematics and Physics*, 28:131–139, 1949.

[122] R. Schmieder. Stokes algebra formalism. *Journal of Optical Society of America*, 59:297–302, 1969.

[123] U. Fano. A stokes-parameter technique for the treatment of polarization in quantum mechanics. *Physical Review*, 93:121–123, 1954.

[124] S. Mukamel. *Principles of Nonlinear Optical Spectroscopy.* Oxford University Press, 1999.

Acknowledgements

First of all, I want to thank Dr. Jan Helbing, who supervised me during my Ph.D. work, I learnt a lot from him, both from technical and experimental side and he guided me through the jungle of chiral infrared spectroscopy. Further thanks go to Prof. Dr. Peter Hamm for giving me the opportunity to realize my thesis in his group. I am also grateful for all group members (present and former) with whom I had a wonderful time during the last four years. Hoping not to forget anyone: Jens Bredenbeck, Rolf Pfister, Virgiliu Botan, Valentina Cervetto, Mariusz Kozinski, Ellen Backus, Janne Ihalainen, Marco Schade (Marcoschado), Fivos Perakis (Au bon lait de brebis), Julien Réhault (Réhoult), Esben Andresen, Alexander Rodenberg, Mateusz Donten, Robbert Bloem, Samuele Giani (Jenny), Valéry Weber, Harry Bregy, Sean Garret-Roe, Jouko Korppi-Tommola, Paul M. Donaldson.

Furthermore, I want to thank Armin Kühne, Roland Zehnder and Horst Blasi for their precision mechanical pieces, Ueli Feusi and Jens Jacobs for their computer support, Hermann Schwarz for his electronic devices and also Maja Gossweiler for handling all the administrative stuff.

All this work could not have been possible without the constant support of my parents and my two sisters and also from my friends (from Switzerland and France) who were always there for me, many thanks to all of you.

Curriculum vitae

Surname: BONMARIN

First name: Mathias

Place and date of birth: Bern, Switzerland, 31.05.1979

Citizenship: Swiss (Val-de-Travers NE)

Education:

2006 - pres.	*Ph.D. Program, Graduate School of Chemical and Molecular Sciences* University of Zurich, Zurich (Switzerland)
2004 - 2005	*Master in Economics* Catholic University of Louvain, Louvain-la-neuve (Belgium)
2002 - 2003	*Master of Science in Optics, Opto-electronics and Microwaves* Grenoble Institute of Technology, Grenoble (France)
1997 - 2002	*Master of Science in Biomedical Engineering* School of Advanced Studies in Engineering, Marseilles (France) *Diploma Thesis Title*: Low Coherence Interferometry for High Resolution Imaging
1997	*French Scientific Baccalauréat* Provence High School, Marseilles (France)